

## ABSTRACT

BROWN, ELISABETH MARY MARGARET. A Nonlinear Conservation Law Modeling Carbon Sequestration. (Under the direction of Michael Shearer.)

A quasi-linear hyperbolic partial differential equation with a discontinuous flux models geologic carbon dioxide ( $\text{CO}_2$ ) migration and storage through residual trapping [17]. Dual flux curves emerge in this model, giving rise to flux discontinuities. One flux describes the invasion of the plume into pore space, and the other captures the flow as the plume drains and leaves  $\text{CO}_2$  bubbles behind, which are then trapped by brine in the pore space between rock grains. Flux functions with discontinuities in space have been previously studied; however, the flux in this model depends on how the plume height changes in time, a different kind of discontinuity that introduces new patterns. A striking feature of this simple model is that, because of its dual flux curves, solutions of the conservation law can include the prediction that the entire  $\text{CO}_2$  plume is deposited as bubbles in a finite time.

The model is explored in more detail, and some mathematical issues are resolved. We describe the construction of fundamental wave solutions of the equation, namely shock waves and rarefaction fans. To establish the admissibility of shock waves, we introduce the notion of cross-hatch characteristics to address the ambiguity of characteristic speeds in regions of the characteristic plane where the solution is constant. Detailed analytic solutions of wave interactions resulting from the dual flux model include some properties that do not occur in conventional scalar conservation laws. Some wave interactions yield novel phenomena due to the dual flux, such as shock-rarefaction interactions that would persist for all time with a single flux, here are completed in finite time.

The existence of an entropy solution of the Cauchy problem for any initial  $\text{CO}_2$  plume is established using wave-front tracking. To prove this theorem, we construct piecewise constant approximate solutions of the Cauchy problem using expansion shocks in place of rarefaction waves. In order to establish that a subsequence of approximate solutions converges to an entropy solution of the Cauchy problem, we have to account for the dual fluxes carefully.

© Copyright 2017 by Elisabeth Mary Margaret Brown

All Rights Reserved

A Nonlinear Conservation Law Modeling Carbon Sequestration

by  
Elisabeth Mary Margaret Brown

A dissertation submitted to the Graduate Faculty of  
North Carolina State University  
in partial fulfillment of the  
requirements for the Degree of  
Doctor of Philosophy

Applied Mathematics

Raleigh, North Carolina

2017

APPROVED BY:

---

Michael Shearer  
Chair of Advisory Committee

---

Mansoor Haider

---

Alina Chertock

---

Ralph Smith

## DEDICATION

This degree is dedicated to my parents, Dr. Judith Taylor & Edward Brown,  
and everyone who has ever smiled at me.

## BIOGRAPHY

Elisabeth was raised on ten acres outside of Williamston, Michigan where her parents instilled within her a love of traveling and volunteering. Such adventures led her to Bozeman, Montana for undergraduate studies at Montana State University. Before graduating in 2008 with Bachelor of Science degrees in both Civil Engineering and Mathematics, Elisabeth developed a deep fascination with water flow and hydraulics. During her graduate studies at North Carolina State University in Raleigh, North Carolina, Elisabeth unearthed a desire to delve into research problems that arise due to the connectedness between engineering and mathematics; in both fields, she explored research projects involving fluid flow. In August 2012, Elisabeth earned a Master of Science degree in Civil Engineering for her thesis work in the water resources field of coastal engineering. In December of that same year, she obtained another Master of Science degree after her current advisor and other professors welcomed her to the realm of applied mathematics. In the following semesters, Elisabeth pursued her love of partial differential equations that model fluid flow, and she immersed herself in teaching that topic to undergraduate and graduate students. Elisabeth's Ph.D. research was intertwined with the ever-present fluids theme of her academic career. This dissertation and a Doctorate in Applied Mathematics from North Carolina State University are the results.

## ACKNOWLEDGEMENTS

I would like to thank my advisor, Dr. Michael Shearer, for his immeasurable amount of expertise, guidance, and support throughout my years under his tutelage. He ultimately led me to a deeper appreciation and love of the mathematics of fluid flow that only someone so close to this area could imbue into another person.

I also wish to thank Dr. Mansoor Haider for first introducing me to partial differential equations and his continued encouragement throughout my time in graduate school. Thanks also to Dr. Alina Chertock for her generous insight and mentoring. I would like to express my sincere appreciation to Dr. Ralph Smith, a fellow Montana State University graduate, for constructive dialog throughout my time in North Carolina.

Thanks are also extended to my friends who are fanned out (like a rarefaction) from coast to coast, as well as those folks in Raleigh and SAS Hall, for frequent smiles and encouragement. I have so enjoyed solving cleverly-themed crossword puzzles, traveling, going to group fitness classes, riding my road bike on 100-mile adventures, crushing competitors in beach volleyball, and geocaching with you all. Also, how could I forget Cup A Joe where some of my most insightful thoughts occurred.

A special thank you to my parents. We did it!

Finally, special thanks to Slalom and Putter, whose collective weight equals the number of pages in the Existence Theorem... doubled.

# TABLE OF CONTENTS

List of Tables . . . . .	vii
List of Figures . . . . .	viii
Chapter 1 Introduction . . . . .	1
Chapter 2 The Dual Flux Model . . . . .	5
2.1 Model Assumptions . . . . .	5
2.2 Residual Trapping . . . . .	9
2.3 Dimensionless Partial Differential Equation [17] . . . . .	12
2.4 Summary of the Dual Flux Model . . . . .	14
Chapter 3 Characteristics and Shocks . . . . .	16
3.1 Cross-hatch Characteristics . . . . .	16
3.2 Shocks . . . . .	17
3.3 Expansion Shocks . . . . .	22
3.4 Rarefactions . . . . .	24
Chapter 4 Wave Interactions . . . . .	27
4.1 Catalog of Interactions . . . . .	27
4.2 Case A: Shock - Rarefaction: $\eta_L < \eta_M$ and $\eta_R < \eta_M$ . . . . .	30
4.2.1 Case A: Example . . . . .	31
4.2.2 Case A: Summary & Cross-hatch Characteristics . . . . .	33
4.2.3 Case $\mathcal{A}$ : Shock - Expansion Shock: $\eta_L < \eta_M$ and $\eta_R < \eta_M$ . . . . .	35
4.3 Case B: Shock - Shock: $\eta_L < \eta_M < \eta_R$ . . . . .	36
4.4 Case C: Rarefaction - Shock: $\eta_M < \eta_L$ and $\eta_M < \eta_R$ . . . . .	36
4.4.1 Case C: Example . . . . .	39
4.4.2 Case $\mathcal{C}$ : Expansion Shock - Shock: $\eta_M < \eta_L$ and $\eta_M < \eta_R$ . . . . .	41
4.5 Non-increasing Total Variation & Number of Waves . . . . .	42
Chapter 5 Existence Theorem . . . . .	44
5.1 Wave-front Tracking . . . . .	45
5.2 Proof: Existence of a Weak Solution of (5.0.1) . . . . .	46
5.2.1 Existence of a Limit Function . . . . .	46
5.2.2 Limit Function is a Weak Solution . . . . .	48
5.3 Proof: Limit Function is an Entropy Solution of (5.0.1) . . . . .	49
5.3.1 Classical Shocks Satisfy the Entropy Inequality . . . . .	50
5.3.2 Admissible Shock Entropy Inequality: Example . . . . .	51
5.3.3 Rarefaction Waves Satisfy the Entropy Inequality . . . . .	53
5.4 Existence of a Classical Entropy Solution . . . . .	57
Chapter 6 Comprehensive Example . . . . .	60
6.1 Rarefaction-Shock-Rarefaction Solution . . . . .	60

6.2	Graze Characteristic Leads to Cross-hatch Characteristics . . . . .	62
6.3	Expansion Shock Justification . . . . .	63
6.4	Solution After Constant $\eta_{\text{graze}}$ Region Emerges . . . . .	66
6.5	Results with Dimensional Parameters . . . . .	67
<b>Chapter 7</b>	<b>Exact Numerical Solutions . . . . .</b>	<b>69</b>
7.1	Wave-front Tracking Algorithm . . . . .	69
7.2	Trapping Comparison of Wave-front Tracking Solutions . . . . .	74
7.3	Sequence of Numerical Wave-front Tracking Solutions . . . . .	78
<b>Chapter 8</b>	<b>Concluding Remarks . . . . .</b>	<b>83</b>
<b>References</b>	<b>. . . . .</b>	<b>86</b>
<b>Appendices</b>	<b>. . . . .</b>	<b>91</b>
Appendix A	Preliminary Proofs . . . . .	92
A.1	Helly's Compactness Theorem . . . . .	92
A.2	Time-Dependent Helly's Theorem . . . . .	99
A.3	Arzela-Ascoli Theorem . . . . .	101
Appendix B	Numerical Codes . . . . .	104
B.1	MATLAB Implementation of Analytic Results . . . . .	104
B.2	Wave-front Tracking Numerical Code . . . . .	111



## LIST OF TABLES

Table 4.1	Possible initial conditions with three states. . . . .	29
Table 4.2	Shock position $\xi = \hat{\xi} + \alpha (1 - 2\hat{\eta}) \tau + \left[ (\xi_e - \hat{\xi}) \tau_e^{-\beta_1} - \alpha (1 - 2\hat{\eta}) \tau_e^{\beta_2} \right] \tau^{\beta_1}$ for a shock emanating from $(\xi_e, \tau_e)$ that is the result of a rarefaction emanating from $\hat{\xi}$ interacting with a constant state $\hat{\eta}$ , for $\mathcal{M} = 1$ and $\sigma = 1 - \varepsilon$ . The colored circles correspond to shock colors in Figures 4.2.1 and 4.4.3. . . . .	34
Table 4.3	Wave interaction summary. . . . .	43

## LIST OF FIGURES

Figure 1.0.1 Schematic of the carbon sequestration process. Captured CO <sub>2</sub> is injected below an impermeable layer of rock for storage. Taken from [43]. . . . .	2
Figure 1.0.2 As a CO <sub>2</sub> plume flows through permeable rock, some of the CO <sub>2</sub> becomes residually trapped in the pore spaces between rock grains. . . . .	3
Figure 2.1.1 A CO <sub>2</sub> plume in a porous layer with variables used in derivation of model. . .	6
Figure 2.1.2 Hydrostatic pressure geometry in the (a) CO <sub>2</sub> and (b) brine layers. . . . .	7
Figure 2.1.3 (a) Vertical distance between origin and any point $(x, z)$ . (b) Replicated from [17]: Flow rates for brine and CO <sub>2</sub> impact the time rate of change of volume for an arbitrary control volume. . . . .	8
Figure 2.2.1 Initial plume shape represented by dashed line. When plume is invading new pore space, $\frac{\partial h(x,t)}{\partial t} > 0$ , and when the plume is draining and leaving a residual surface, $\frac{\partial h(x,t)}{\partial t} < 0$ . . . . .	10
Figure 2.3.1 Shown in dimensionless variables, a residual area of immobile CO <sub>2</sub> remains as the plume migrates to the right. . . . .	13
Figure 2.4.1 Dual fluxes (2.4.3) for $\mathcal{M} = 10$ and $\varepsilon = 0.4$ . Both flux curves attain a maximum value at $\eta^* = 1/(1 + \sqrt{\mathcal{M}})$ . The characteristic speeds satisfy $0 < (1 - \varepsilon)f'(\eta) < f'(\eta)$ if $\eta < \eta^*$ , and $f'(\eta) < (1 - \varepsilon)f'(\eta) < 0$ if $\eta > \eta^*$ . . .	15
Figure 3.1.1 For $\eta < \eta^*$ , $0 < (1 - \varepsilon)f'(\eta) < f'(\eta)$ , and for $\eta > \eta^*$ , $f'(\eta) < (1 - \varepsilon)f'(\eta) < 0$ . . .	17
Figure 3.2.1 Faster characteristics on each side of admissible shock impinge on the shock. . .	18
Figure 3.2.2 A forward shock with $\Lambda > 0$ . (a) Characteristic plane with cross-hatch characteristics in constant regions. (b) Shock speed determined from the upper flux curve. . . . .	19
Figure 3.2.3 Backward shock, $\Lambda < 0$ , for which (a) $\eta_\tau > 0$ , so the shock speed is found from the lower flux curve, (b). . . . .	20
Figure 3.2.4 (a) All four characteristics enter admissible shock. (b) Slower characteristics on left leave admissible shock. . . . .	21
Figure 3.2.5 (a) An initial step up yields a shock wave. (b) Stationary vertical interface between brine and CO <sub>2</sub> plume, $\Lambda = 0$ . (c) Forward shock, $\Lambda > 0$ . (d) Backward shock, $\Lambda < 0$ . . . . .	22
Figure 3.3.1 Slower characteristics on each side of admissible shock leave the shock in forward time. . . . .	23
Figure 3.3.2 Backward expansion shock. (a) All characteristics leave the shock. (b) The faster characteristics on the left, with speed $(1 - \varepsilon)f'(\eta_L)$ , enter the shock. . .	23
Figure 3.4.1 (a) Three expansion shocks approximating a centered rarefaction wave. Since $\eta$ is necessarily decreasing from left to right in the rarefaction wave, we have that $\eta_\tau < 0$ left of the $\tau$ axis, so that $\sigma = 1$ , as indicated in (b). To the right, $\eta_\tau > 0$ , so that $\sigma = 1 - \varepsilon$ there. . . . .	24

Figure 3.4.2 (a) A step down yields a rarefaction fan. (b) With parameters $\mathcal{M} = 10$ , $\varepsilon = 0.4$ , the upper flux curve is traversed by $(\tilde{\eta}, \sigma f(\tilde{\eta}))$ as the rarefaction fans from $\eta_L$ down to $\eta^*$ , then jumps down to the lower flux curve as the solution decreases from $\eta^*$ to $\eta_R$ .	25
Figure 3.4.3 A rarefaction wave propagating left and right. The discontinuity in $\sigma$ corresponds to a discontinuity in the interface slope.	26
Figure 4.1.1 Initial condition with (P1) $\eta_L = \eta_R < \eta_M$ , (P2) $\eta_L < \eta_R < \eta_M$ , (P3) $\eta_R < \eta_L < \eta_M$ , (P4) $\eta_M < \eta_L = \eta_R$ , (P5) $\eta_M < \eta_R < \eta_L$ , (P6) $\eta_M < \eta_L < \eta_R$ , (P7) $\eta_L < \eta_M < \eta_R$ , and (P8) $\eta_R < \eta_M < \eta_L$ .	28
Figure 4.1.2 Summary of results for eight possible initial pairings.	30
Figure 4.2.1 For shock-rarefaction interaction with $\eta_L = 0.2$ , $\eta_M = 1$ , $\eta_R = 0.3$ , $\varepsilon = 0.4$ , (a) characteristic and shock speeds determined from discontinuous flux curves, and (b) solution in characteristic plane. Dashed red lines in (a) correspond to point ① in (b) where shock speed equals slower characteristic speed on left.	32
Figure 4.3.1 (a) Pair 8b has fanning rarefactions separated by a fixed distance for all time. (b) Case B example (Pair 7e) has two shocks colliding.	37
Figure 4.4.1 No interaction when speed of leading characteristic in rarefaction is less than shock speed represented on (a) discontinuous flux curves and (b) characteristic plane with $\eta_L = 0.51$ , $\eta_M = 0$ , $\eta_R = 0.9$ , $\sigma = 0.05$ , and $\tilde{\eta}_M \approx 0.95$ .	38
Figure 4.4.2 Shock speeds and characteristic speeds determined by discontinuous flux curves for $\eta_M = 0$ , $\eta_R = 0.9$ , $\varepsilon = 0.7$ , $\mathcal{M} = 1$ . Points (a)-(e) correspond to points on Figure 4.4.3.	40
Figure 4.4.3 Analytic solution for $\eta_M = 0$ , $\eta_R = 0.9$ , $\varepsilon = 0.7$ , $\mathcal{M} = 1$ with (f) $\eta_L = 0.51 < \tilde{\eta}$ , and (g) $\eta_L = 0.7 > \tilde{\eta}$ . Points (a)-(e) correspond to Figures 4.4.2(a)-(e).	41
Figure 5.2.1 Geometric demonstration of the $L^1$ norm.	47
Figure 5.3.1 For forward shocks with $\Lambda(\eta) > 0$ in (a) and backward shocks with $\Lambda(\eta) < 0$ in (b), the characteristics determined by upper (in blue) and lower (in green) flux curves are slower (more negative) than the shocks (in red). (c) Since $E(\eta_L) = E'(\eta_L) = 0$ and $E'(\eta) < 0$ for all $\eta > \eta_L$ , it follows that $E(\eta_R) < 0$ .	52
Figure 5.3.2 (a) Arbitrary volume $V$ through which front $\xi = y_m(\tau)$ propagates, and (b) details of volume $V_-$ and $\partial V_-$ .	54
Figure 5.3.3 For expansion shock $y_m$ , the black tangent lines to the discontinuous flux curves always have $\tilde{f}'(\eta_m^L) \leq \tilde{f}'(n) \leq \tilde{f}'(\eta_m^R)$ for $n \in [\eta_m^R, \eta_m^L]$ and $\tilde{f}$ given by (5.3.1).	56
Figure 5.3.4 As the size of the expansion shocks decreases (and therefore the number of expansion shocks increases from one (a) to three (b)), the rarefaction is obtained in the limit (c). Here, $\eta_L = \eta_R = 0.1$ , $\eta_M = 0.6$ , and $\varepsilon = 0.4$ .	58
Figure 6.1.1 Initial condition where (b) is a magnification of a portion of (a).	61

Figure 6.1.2	Exact solution for $\eta_L = 0.3$ , $\eta_0(-0.5) = 0.1$ , $\eta_M = 1$ , $\eta_R = 0.2$ , $\mathcal{M} = 1$ and $\varepsilon = 0.4$ . The non-centered rarefaction on the right interacts with $\eta_M$ until point (a), when the plume breaks away from the bottom of the aquifer. The two rarefactions begin to interact at point (a) to yield a shock that becomes stationary at (b). After point (c), the speeds of both rarefactions are reduced due to trapping. At point (d), the shock speed equals the speed of the entering characteristic corresponding to $\eta_{\text{graze}}$ in the non-centered rarefaction, resulting in a constant region with cross-hatch characteristics. The faster characteristics, in red, now enter the shock from the left. The shock persists until time $\tau_e$ , when the $\eta_{\text{graze}}$ characteristic within the rarefaction enters the shock from the right, point (e).	62
Figure 6.3.1	Expansion shock approximations of initial rarefactions.	63
Figure 6.3.2	Expansion shock representation of the continuous solution in Figure 6.1.2, with corresponding points (a)-(c).	64
Figure 6.3.3	Expansion shock justification of constant state $\eta_{\text{graze}}$ .	65
Figure 6.4.1	Analytic solution of initial condition that is completely trapped as residual bubbles after a finite time, $\tau_{\text{end}} = 168.45$ , and at a finite position, $\xi_{\text{final}} = 111.07$ , the blue star. Here, $\mathcal{M} = 1$ , $\varepsilon = 0.4$ , and the plume has $\eta_L = 0.3$ , $\eta_{\text{graze}} \approx 0.25$ , and $\eta_R = 0.2$ , with $\eta = 0$ in the rest of the aquifer.	67
Figure 7.1.1	(a) Initial condition $\eta_0 \in L^1(\mathbb{R}) \cap BV(\mathbb{R})$ , (b) seven middle $\eta$ values within initial plume, and (c) piecewise constant approximation.	70
Figure 7.1.2	Compression shocks have $\eta_L < \eta_R$ . (a) Speed of forward compression shock determined by upper flux curve. (b) Speed of backward compression shock determined by lower flux curve.	71
Figure 7.1.3	Expansion shocks have $\eta_L > \eta_R$ . (a) Speed of forward expansion shock determined by lower flux curve. (b) Speed of backward expansion shock found on upper flux curve.	71
Figure 7.1.4	Exact wave-front solutions of initial Riemann problems up to the first shock collision in (a) characteristic plane and (b) solution space, where shocks are shown as vertical interfaces. In (b) and (c), arrows indicate directions and magnitudes of propagating shocks. (c) At this interaction time, $\tau = 0.72$ , an orange backward expansion shock collides with a pink classical backward shock and eliminates the solution state $\eta = 0.93$ , the black star in (b).	72
Figure 7.1.5	(a) Initial plume approximated by piecewise constant states (top) such that the maximum jump up (compressive shock) and jump down (expansion shock) is $h_{\text{max}} = 0.47$ , and (bottom) the resulting exact wave-front tracking solution for $\varepsilon = 0.8$ in characteristic space. (b) Corresponding migrating plume and residual surface in solution space at interaction times.	73
Figure 7.2.1	Initial plume and resulting residual surface for trapping parameter $\varepsilon = 0.8$ and maximum shock size = 0.47.	74
Figure 7.2.2	Trapping parameter is decreased to $\varepsilon = 0.4$ . (a) Initial shock speeds and directions for piecewise constant plume approximation with maximum shock size = 0.47. (b) Wave-front propagation of plume migration after one interaction, when the constant state indicated by the black star in (a) is eliminated.	75

Figure 7.2.3 (a) (top) Initial plume approximated as in Section 7.1, and (bottom) the resulting exact wave-front tracking solution for $\varepsilon = 0.4$ in characteristic space. (b) Corresponding migrating plume and exact residual surface for $\varepsilon = 0.4$ in solution space. . . . .	76
Figure 7.2.4 Residual surfaces when $\varepsilon = 0.8$ (more trapping) and $\varepsilon = 0.4$ (less trapping). .	77
Figure 7.3.1 (a) Initial approximation with $h_{\max} = 0.37$ and resulting exact wave-front tracking solution. (b) The plume migrates until the final interaction time, $\tau_{\text{end}} = 13.08$ , after which point, a residual surface is all that remains. . . .	78
Figure 7.3.2 Results of numerical implementation of the wave-front tracking method for an approximation of the initial condition with $h_{\max} = 0.27$ . . . . .	79
Figure 7.3.3 Results of numerical implementation of the wave-front tracking method for an approximation of the initial condition with $h_{\max} = 0.17$ . . . . .	80
Figure 7.3.4 Initial plume is approximated with 37 constant states due to the restriction, $h_{\max} = 0.07$ , on maximum sizes of jumps up (classical shocks) and down (expansion shocks). (a) Wave-fronts corresponding to 37 initial constant states and shock speeds and directions. (b) Plume location after one interaction. (c) Exact locations of the wave-fronts are tracked throughout the characteristic plane until final interaction point of $\tau_{\text{end}} = 12.36$ and $\xi_{\text{final}} = 4.40$ . . . . .	81
Figure 7.3.5 An exact wave-front tracking solution, for maximum allowable initial shock sizes of $h_{\max} = 0.07$ , provides a visualization of plume migration at each interaction time. The mobile plume is blue, the residual surface of trapped bubbles is light blue, and the brine is white. . . . .	82
Figure B.1.1 Analytic Case A Example MATLAB code. . . . .	105
Figure B.2.1 Wave-front tracking MATLAB code. . . . .	112

Some 35.7 billion tonnes of carbon dioxide ( $\text{CO}_2$ ) were emitted into the atmosphere in 2014 [34], an increase from the previous year's global  $\text{CO}_2$  emissions of 32 gigatonnes [19]. In 2000, the Intergovernmental Panel on Climate Change projected a range of estimated emissions from fossil fuel combustion and industrial processes for the year 2020; current emissions are within that annual planning range of 29 to 44 billions tonnes of  $\text{CO}_2$  [20]. The capture of  $\text{CO}_2$  before its exodus into the atmosphere seems to be a promising technological solution to reduce the escalating global impact of  $\text{CO}_2$  emissions. In such a process, gaseous  $\text{CO}_2$  is collected at industrial sites and power plants, compressed, and injected into geological formations deep underground, as shown in Figure 1.0.1. Geotechnical evidence suggests that there is a potential subsurface storage capability of 2,000 billion tonnes of  $\text{CO}_2$  in porous reservoirs worldwide [20]. A goal of future and ongoing carbon dioxide capture and storage projects, such as the Sleipner project where nearly one million tonnes of  $\text{CO}_2$  are injected annually into a permeable sandstone layer beneath the North Sea [41, 44, 48], is to permanently trap  $\text{CO}_2$  kilometers underground and prevent the greenhouse gas from entering the atmosphere [14, 33]. While a wealth of seismic surveys of the Sleipner project have indicated no signs of leakage [6], the possibility of escape of the injected  $\text{CO}_2$  from brine-filled aquifers remains a concern.

During injection, the captured gaseous  $\text{CO}_2$  is compressed and becomes supercritical; hence, upon release into the porous rock, the sequestered  $\text{CO}_2$  behaves like a liquid. The supercritical  $\text{CO}_2$  is less dense than the ambient brine, so the injected plume rises within the aquifer [16, 17, 18]. Appropriate sites for carbon capture and storage projects have an impermeable cap rock in the geological formation that acts as a barrier to hinder the upward migration of the

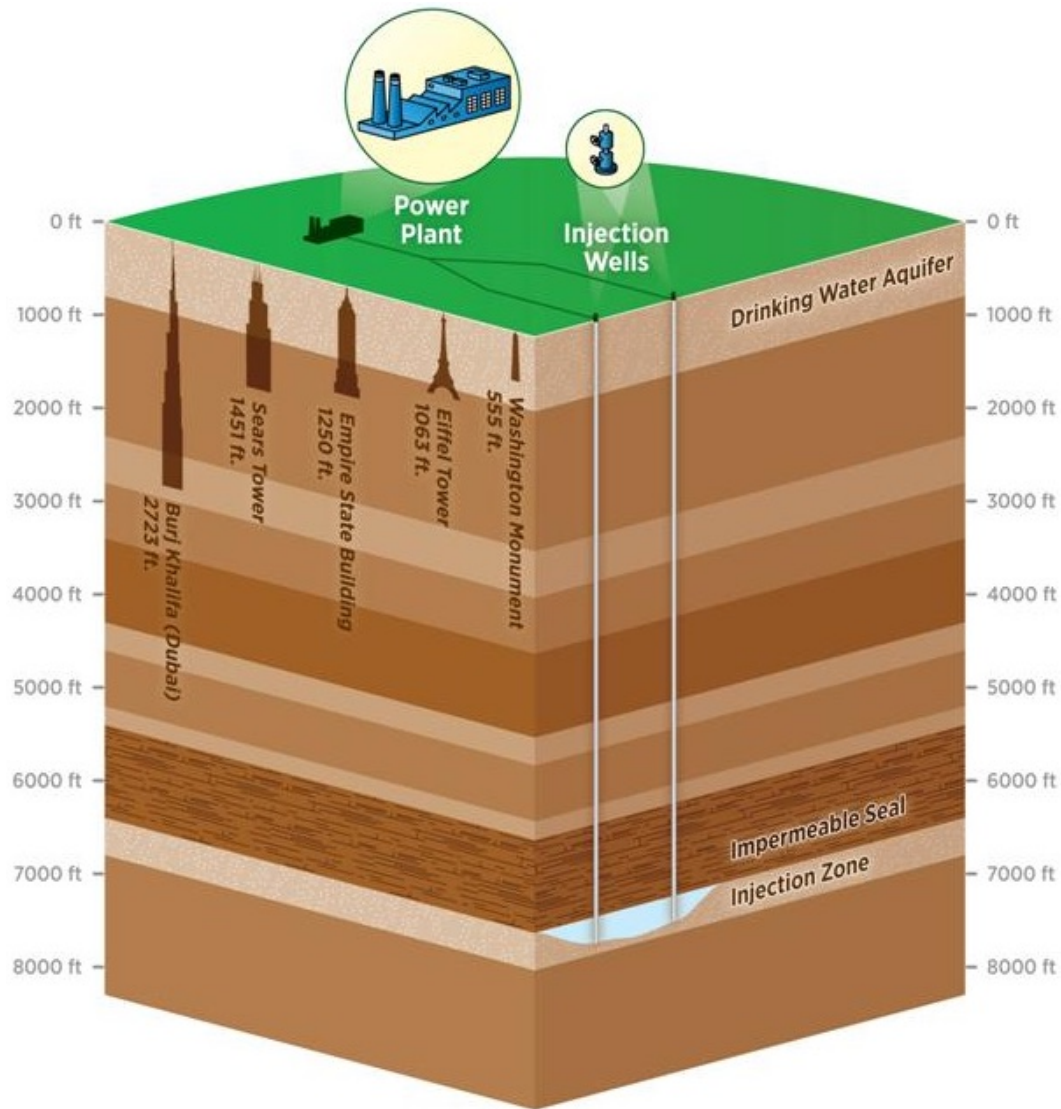


Figure 1.0.1: Schematic of the carbon sequestration process. Captured  $\text{CO}_2$  is injected below an impermeable layer of rock for storage. Taken from [43].

buoyant plume and keep the  $\text{CO}_2$  beneath the Earth's surface [2]. Once the plume rises to the impermeable upper boundary, the  $\text{CO}_2$  travels along inclines in the cap's lower surface and spreads through the porous rock as a gravity current. As the plume migrates, it deposits bubbles of  $\text{CO}_2$  that remain in place. The sequestration is successful if all of the  $\text{CO}_2$  in the plume is deposited before the plume reaches fractures within the cap rock that would allow leakage of the plume from the aquifer [14, 19, 40, 44].

This mechanism to permanently immobilize  $\text{CO}_2$  within a porous medium is known as residual trapping. Capillary forces between the two fluids (brine and supercritical  $\text{CO}_2$ ) stably trap bubbles of  $\text{CO}_2$  within pore spaces. As the plume of  $\text{CO}_2$  migrates through a previously brine-filled aquifer, surface tension within the pore geometry around the rock grains inhibits the brine from refilling all pore space in the wake of the plume. As shown in Figure 1.0.2, some of the  $\text{CO}_2$  becomes residually trapped in nooks and crannies within the pore space as isolated ganglia that become disconnected from the bulk of the plume as brine permeates into the remaining pore space [14, 17, 19, 21, 36]. Without residual trapping, the  $\text{CO}_2$  plume could migrate indefinitely. Residual trapping reduces the volume of mobile  $\text{CO}_2$  within the plume and enables aquifers with a fractured cap rock to be used effectively for  $\text{CO}_2$  storage.

Hesse, Orr, and Tchelepi [17] formulated a nonlinear hyperbolic partial differential equation with a discontinuous flux to model geologic carbon dioxide migration and storage through residual trapping. As shown in the model derivation in Section 2, the switch between the two concave dual flux functions is prescribed to occur at points  $(x, t)$  where the height  $h(x, t)$  of the plume at position  $x$  at time  $t$  changes from increasing to decreasing in time, i.e.,  $\frac{\partial h(x, t)}{\partial t}$  changes sign. A striking feature of this simple model is that, because of its dual flux curves, solutions of the equation can include the prediction that the entire  $\text{CO}_2$  plume is deposited as bubbles in a finite time.

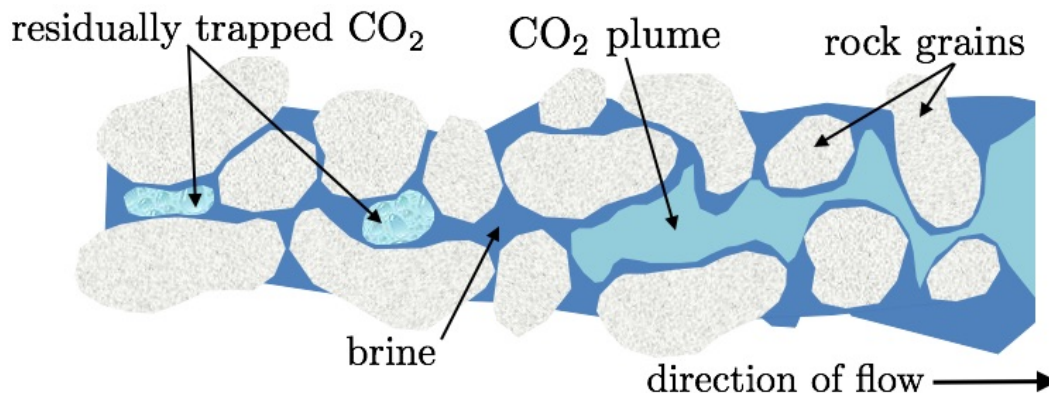


Figure 1.0.2: As a  $\text{CO}_2$  plume flows through permeable rock, some of the  $\text{CO}_2$  becomes residually trapped in the pore spaces between rock grains.



In this dissertation, we explore the model in more detail, resolving some mathematical issues and establishing the existence of entropy solutions of the Cauchy problem using wave-front tracking. In Chapter 2, we derive the modeling equation of [17], including the switch between the two flux functions, depending on whether the plume is propagating into a region of brine or depositing  $\text{CO}_2$  droplets. In Chapter 3, we describe the construction of fundamental wave solutions of the equation, namely shock waves and rarefaction waves. To establish the admissibility of shock waves, we introduce the notion of cross-hatch characteristics to address the ambiguity of characteristic speeds. Chapter 4 includes a detailed description of wave interactions, including some properties that do not occur in conventional scalar conservation laws. In Chapter 5, we construct piecewise constant approximate solutions of the Cauchy problem using expansion shocks in place of rarefaction waves. In order to establish that a subsequence of approximate solutions converges to an entropy solution of the Cauchy problem, we have to account for the dual fluxes carefully. The analytic solution of the example included in Chapter 6 relies on the inclusion of cross-hatch characteristics from both flux functions, and exact numerical wave-front tracking solutions are presented in Chapter 7. We conclude the dissertation in Chapter 8 with some remarks.

---

## The Dual Flux Model

---

In this chapter, we outline several simplifying assumptions about the aquifer and the nature of the flow, then derive the model, a first order conservation law with a switch in flux depending on whether, at a given location, the CO<sub>2</sub> plume is advancing or depositing bubbles in its wake. Further details regarding the model can be found in Hesse, Orr, and Tchelepi [17].

### 2.1 Model Assumptions

Subsurface geology often has complicated spatial variability, and three-dimensional models of carbon sequestration involve unresolved and difficult issues. To simplify matters, we consider a porous aquifer that is locally uniform in the transverse direction and analyze the two-dimensional propagation of a cross-section of the flow through a porous aquifer of constant thickness  $H$  beneath an impermeable cap rock sloped at constant angle  $\theta$ . A buoyant plume of supercritical carbon dioxide, CO<sub>2</sub>, with height  $h(x, t)$  at position  $x$  and time  $t$  is introduced to the brine-filled aquifer for storage, as shown in Figure 2.1.1. Each incompressible fluid occupies a distinct portion of the aquifer, so, with this sharp interface assumption, the dissolution of CO<sub>2</sub> into the brine is neglected [17, 19].

The viscosity contrast between the two fluids propels the CO<sub>2</sub> plume to invade available pore space as it migrates laterally as a gravity current [14, 22, 35]. The advection-dominated migration is mainly horizontal, and the displacement of the brine by the CO<sub>2</sub> plume is assumed to be slow enough so that the gravity-capillary equilibrium is maintained in any vertical cross-section

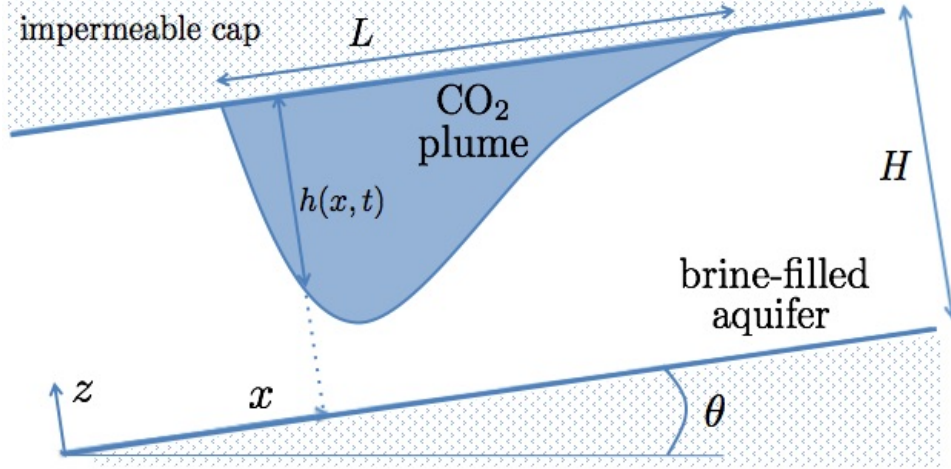


Figure 2.1.1: A CO<sub>2</sub> plume in a porous layer with variables used in derivation of model.

[17]. Assume  $P_c$  is the constant capillary pressure “necessary to squeeze a hydrocarbon droplet through a pore throat” [45], and let  $p_I(x, t)$  be the pressure at the interface between brine and supercritical CO<sub>2</sub> at position  $x$  at time  $t$ . Suppose  $h_b(x, t) = H - h(x, t)$  is the depth of the brine at position  $x$  at time  $t$ , and let  $z$  be the orthogonal distance from the bottom of the aquifer. When  $z = h_b(x, t)$ , the pressure,  $p(x, t)$ , equals the interface pressure,  $p_I(x, t)$ .

Under the assumption that pressure within the current is hydrostatic, the pressure within the CO<sub>2</sub> plume can be determined. Recall that hydrostatic pressure at a point depends on the density of the fluid, gravitational constant  $g$ , and depth at which the pressure is measured. When  $z > h_b(x, t)$ , the point  $(x, z)$  is located within the CO<sub>2</sub> plume, as shown in Figure 2.1.2(a). The hydrostatic pressure induced by the CO<sub>2</sub> layer increases as  $z$  decreases from  $H$  to  $h_b(x, t)$ ; hence, the pressure within the plume is given by

$$p(x, t) = P_c + p_I(x, t) - \rho g [z - h_b(x, t)] \cos(\theta)$$

where  $\rho$  is the density of the supercritical CO<sub>2</sub>. As shown in Figure 2.1.2(b), a point  $(x, z)$  is in the brine layer when  $z < h_b(x)$ . Since the brine is beneath the interface, hydrostatic pressure will add to the interface pressure, and it follows that the pressure in the brine layer is

$$p(x, t) = p_I(x, t) + (\rho + \Delta\rho) g [h_b(x, t) - z] \cos(\theta)$$

where  $\rho + \Delta\rho$  is the density of the brine; with this notation, it is clear that brine is more dense

than  $\text{CO}_2$ . It follows that the pressure at a point  $(x, z)$  at time  $t$  within the aquifer is given by

$$p(x, t) = \begin{cases} P_c + p_I(x, t) - \rho g [z - h_b(x, t)] \cos(\theta) & \text{when } z > h_b(x, t), \\ p_I(x, t) + (\rho + \Delta\rho) g [h_b(x, t) - z] \cos(\theta) & \text{when } z \leq h_b(x, t). \end{cases} \quad (2.1.1)$$

Within the aquifer, volume is conserved, and the conservation of momentum equation for this fluid flow through a porous medium is given in the form of Darcy's law [16, 19, 21, 44]. Consider phase  $j$ , where  $j = b$  indicates brine, and  $\text{CO}_2$  is designated by  $j = c$ . For phase  $j$ , define  $q_j$  as volume flux per unit width,  $k_{rj}$  as relative permeability,  $\mu_j$  as viscosity, and  $\lambda_j = \frac{k_{rj}}{\mu_j}$  as the constant mobility; the effect of the residual  $\text{CO}_2$  on the mobility of the brine is assumed to be negligible. Let  $k$  be the permeability of the porous medium. The multiphase extension of Darcy's law is given by  $q_j = -k \lambda_j \frac{\partial \phi_j}{\partial x}$ , where  $\phi_j = p(x, t) + \rho_j g [x \sin(\theta) + z \cos(\theta)]$  is the potential of phase  $j$  and is consistent with literature pertaining to petroleum engineering's black oil model [1, 42, 46]. The potential adjusts the pressure given by (2.1.1) and scales by the vertical distance between any point  $(x, z)$  within the aquifer and the origin  $(x, z) = (0, 0)$ , see Figure 2.1.3(a). For the  $\text{CO}_2$  plume, it follows that

$$\begin{aligned} \frac{\partial \phi_c}{\partial x} &= \frac{\partial}{\partial x} \left[ P_c + p_I(x, t) - \rho g [z - h_b(x, t)] \cos(\theta) + \rho g [x \sin(\theta) + z \cos(\theta)] \right] \\ &= \frac{\partial p_I(x, t)}{\partial x} + \rho g \cos(\theta) \frac{\partial}{\partial x} [H - h(x, t)] + \rho g \sin(\theta) \\ &= \frac{\partial p_I(x, t)}{\partial x} + \rho g \left[ -\frac{\partial h(x, t)}{\partial x} \cos(\theta) + \sin(\theta) \right]. \end{aligned} \quad (2.1.2)$$

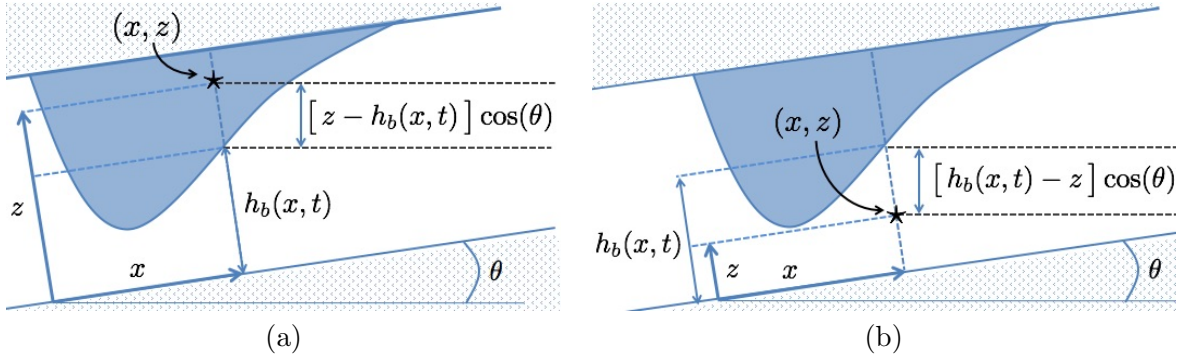


Figure 2.1.2: Hydrostatic pressure geometry in the (a)  $\text{CO}_2$  and (b) brine layers.

Similarly for the brine layer,

$$\begin{aligned}\frac{\partial \phi_b}{\partial x} &= \frac{\partial}{\partial x} \left[ p_I(x, t) + (\rho + \Delta \rho) g [h_b(x, t) - z] \cos(\theta) + (\rho + \Delta \rho) g [x \sin(\theta) + z \cos(\theta)] \right] \\ &= \frac{\partial p_I(x, t)}{\partial x} + (\rho + \Delta \rho) g \left[ -\frac{\partial h(x, t)}{\partial x} \cos(\theta) + \sin(\theta) \right].\end{aligned}\quad (2.1.3)$$

The flow rate per unit width of the CO<sub>2</sub> phase is  $Q_c(x, t) = h(x, t) q_c$ , and the flow rate per unit width of the brine phase is  $Q_b(x, t) = h_b(x, t) q_c$ . From Figure 2.1.3(b), if  $\Delta x$  diminishes to zero, then  $Q_c + Q_b = 0$ . Combining this conservation of volume equation with the extended Darcy's law yields  $h(x, t) \left[ -k \lambda_c \frac{\partial \phi_c}{\partial x} \right] = -(H - h(x, t)) \left[ -k \lambda_b \frac{\partial \phi_b}{\partial x} \right]$ , and by (2.1.2) and (2.1.3), it follows that

$$\frac{\partial p_I(x, t)}{\partial x} = \frac{-g \left[ -\frac{\partial h(x, t)}{\partial x} \cos(\theta) + \sin(\theta) \right] \left[ (H - h(x, t)) \lambda_b (\rho + \Delta \rho) + h(x, t) \lambda_c \rho \right]}{h(x, t) \lambda_c + (H - h(x, t)) \lambda_b}.$$

Hence, the flow rate of the plume becomes

$$Q_c(x, t) = k g \Delta \rho \frac{h(x, t) \lambda_c (H - h(x, t)) \lambda_b}{h(x, t) \lambda_c + (H - h(x, t)) \lambda_b} \left[ -\frac{\partial h(x, t)}{\partial x} \cos(\theta) + \sin(\theta) \right]. \quad (2.1.4)$$

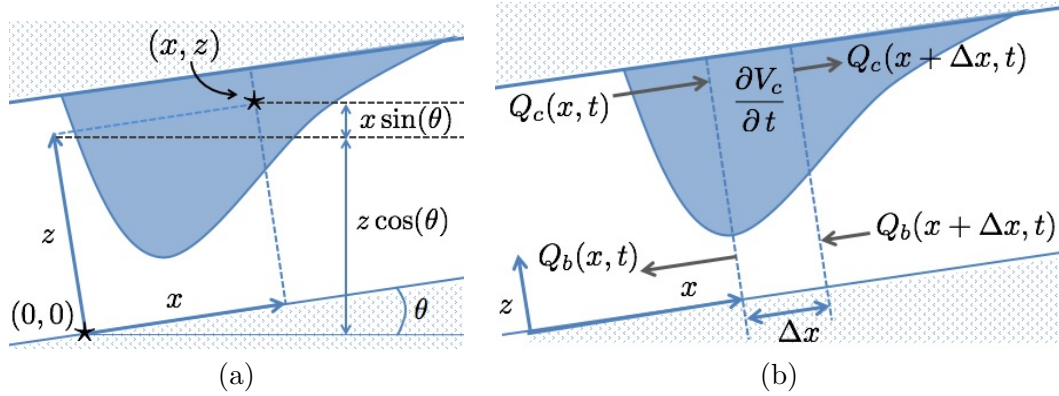


Figure 2.1.3: (a) Vertical distance between origin and any point  $(x, z)$ . (b) Replicated from [17]: Flow rates for brine and CO<sub>2</sub> impact the time rate of change of volume for an arbitrary control volume.

Conservation of volume over an arbitrary control length,  $\Delta x$ , is shown in Figure 2.1.3(b), and it follows that the time rate of change of the plume volume,  $V_c$ , depends on the flow of  $\text{CO}_2$  into and out of the control volume and  $\text{CO}_2$  sources or sinks,  $R'_c$ , within the control volume as

$$\frac{\partial V_c}{\partial t} = Q_c(x, t) - Q_c(x + \Delta x, t) + R'_c, \quad (2.1.5)$$

the differential form of (2.3) in [17].

## 2.2 Residual Trapping

Under the assumption that the formation of residual  $\text{CO}_2$  drives trapping within aquifers, the sink term in (2.1.5) will depend on how residual trapping changes the plume volume in time. Let  $S_{jr}$  be the constant residual saturation of phase  $j$  left behind the  $\text{CO}_2$  plume front [17, 24] and suppose that the possibility of residually trapping bubbles of  $\text{CO}_2$  within the pore space is proportional to the porosity of the porous medium,  $\phi$ .

Consider a plume with initial location shown as in Figure 2.2.1 that then migrates to the right. On the advancing face of the plume, the thickness of the plume is increasing, and  $\frac{\partial h(x, t)}{\partial t} > 0$ . When  $\frac{\partial h(x, t)}{\partial t} > 0$ , migrating  $\text{CO}_2$  is invading new pore space while remaining hydraulically connected to the plume; hence, no volume is lost when the plume is advancing. Correspondingly,  $\frac{\partial h(x, t)}{\partial t} < 0$  in the wake of the plume. When the plume is draining from a region of the aquifer and  $\frac{\partial h(x, t)}{\partial t} < 0$ , brine invades, and bubbles of  $\text{CO}_2$  are isolated within the available pore space; thus, a volume of  $\text{CO}_2$  is lost as residual saturation,  $S_{cr}$ , in the wake of the plume. Hence, for a small time step, the volume of  $\text{CO}_2$  that is lost from a control volume of width  $\Delta x$  within the plume is given by

$$R'_c = \begin{cases} 0 & \text{when } \frac{\partial h(x, t)}{\partial t} > 0, \\ \phi S_{cr} \Delta x \frac{\partial h(x, t)}{\partial t} & \text{when } \frac{\partial h(x, t)}{\partial t} < 0, \end{cases}$$

and (2.1.5) becomes

$$\frac{\partial V_c}{\partial t} = \begin{cases} Q_c(x, t) - Q_c(x + \Delta x, t) & \text{when } \frac{\partial h(x, t)}{\partial t} > 0, \\ Q_c(x, t) - Q_c(x + \Delta x, t) + \phi S_{cr} \Delta x \frac{\partial h(x, t)}{\partial t} & \text{when } \frac{\partial h(x, t)}{\partial t} < 0. \end{cases} \quad (2.2.1)$$

Notice that  $R'_c$  acts as a sink for  $\text{CO}_2$  in (2.2.1) because  $\frac{\partial h(x, t)}{\partial t}$  is negative in the region where residual trapping occurs. Hence, a residual surface of trapped bubbles of  $\text{CO}_2$  remains in the wake of the plume.

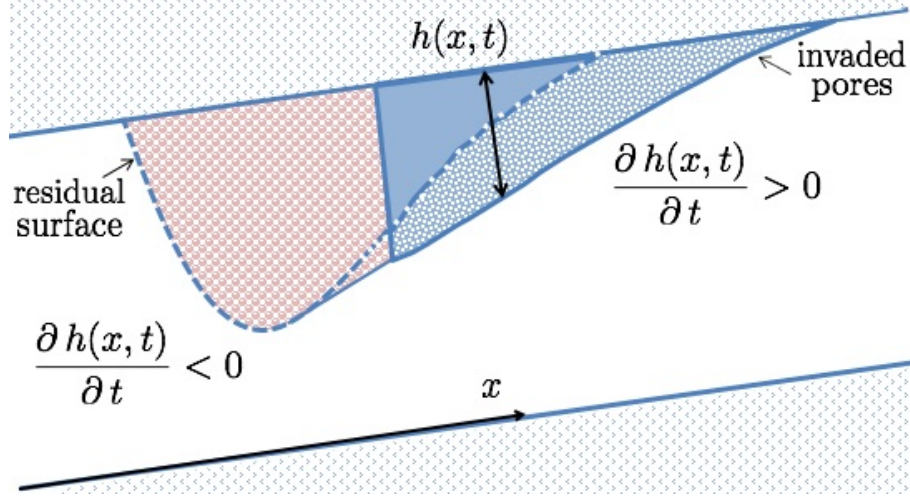


Figure 2.2.1: Initial plume shape represented by dashed line. When plume is invading new pore space,  $\frac{\partial h(x, t)}{\partial t} > 0$ , and when the plume is draining and leaving a residual surface,  $\frac{\partial h(x, t)}{\partial t} < 0$ .

Because capillary entry pressure prevents the drainage of the brine from the smallest pores, some residual brine remains as the  $\text{CO}_2$  plume advances into a region of the aquifer. The volume of  $\text{CO}_2$  within a fixed control width is proportional to the depth of the plume and the amount of available pore space not occupied by residual brine. Hence,

$$\frac{\partial V_c}{\partial t} = \phi (1 - S_{br}) \Delta x \frac{\partial h(x, t)}{\partial t},$$

which, when combined with (2.2.1) yields

$$\phi (1 - S_{br}) \Delta x \frac{\partial h(x, t)}{\partial t} = \begin{cases} Q_c(x, t) - Q_c(x + \Delta x, t), & \frac{\partial h(x, t)}{\partial t} > 0, \\ Q_c(x, t) - Q_c(x + \Delta x, t) + \phi S_{cr} \Delta x \frac{\partial h(x, t)}{\partial t}, & \frac{\partial h(x, t)}{\partial t} < 0. \end{cases}$$

Dividing this by  $\Delta x$  and taking a limit of the resulting expression as  $\Delta x \rightarrow 0$  implies

$$\phi (1 - S_{br}) \frac{\partial h(x, t)}{\partial t} = \begin{cases} -\frac{\partial Q_c(x, t)}{\partial x}, & \frac{\partial h(x, t)}{\partial t} > 0, \\ -\frac{\partial Q_c(x, t)}{\partial x} + \phi S_{cr} \frac{\partial h(x, t)}{\partial t}, & \frac{\partial h(x, t)}{\partial t} < 0. \end{cases} \quad (2.2.2)$$

The mobility ratio,  $\mathcal{M} = \frac{\lambda_c}{\lambda_b}$ , between the supercritical carbon dioxide and the brine depends

on permeability and viscosity of each phase; for carbon sequestration, the invading  $\text{CO}_2$  is more mobile than the ambient brine, so that  $\mathcal{M} \geq 1$  [17, 33]. From (2.1.4), it follows that

$$\begin{aligned}\frac{\partial Q_c(x, t)}{\partial x} &= \frac{\partial}{\partial x} \left( -k g \Delta \rho \frac{h(x, t) \lambda_c (H - h(x, t)) \lambda_b}{h(x, t) (\lambda_c - \lambda_b) + H \lambda_b} \left[ -\sin(\theta) + \frac{\partial h(x, t)}{\partial x} \cos(\theta) \right] \right) \\ &= -k g \Delta \rho \lambda_c \frac{\partial}{\partial x} \left( \frac{h(x, t) (H - h(x, t))}{h(x, t) (\mathcal{M} - 1) + H} \left[ -\sin(\theta) + \frac{\partial h(x, t)}{\partial x} \cos(\theta) \right] \right).\end{aligned}$$

Combination of the above expression with (2.2.2) yields

$$\frac{\partial h(x, t)}{\partial t} = \begin{cases} \frac{k g \Delta \rho \lambda_c}{\phi (1 - S_{br})} \frac{\partial}{\partial x} \left( \frac{h(x, t) (H - h(x, t))}{h(x, t) (\mathcal{M} - 1) + H} \left[ -\sin(\theta) + \frac{\partial h(x, t)}{\partial x} \cos(\theta) \right] \right) & \text{when } \frac{\partial h(x, t)}{\partial t} > 0, \\ \frac{k g \Delta \rho \lambda_c}{\phi (1 - S_{br} - S_{cr})} \frac{\partial}{\partial x} \left( \frac{h(x, t) (H - h(x, t))}{h(x, t) (\mathcal{M} - 1) + H} \left[ -\sin(\theta) + \frac{\partial h(x, t)}{\partial x} \cos(\theta) \right] \right) & \text{when } \frac{\partial h(x, t)}{\partial t} < 0. \end{cases}$$

This can be written in terms of a discontinuous conductivity,  $\kappa$ , to obtain

$$\frac{\partial h(x, t)}{\partial t} = \kappa \frac{\partial}{\partial x} \left( \frac{h(x, t) (H - h(x, t))}{h(x, t) (\mathcal{M} - 1) + H} \left[ -\sin(\theta) + \frac{\partial h(x, t)}{\partial x} \cos(\theta) \right] \right) \quad (2.2.3)$$

where

$$\kappa = \begin{cases} \kappa_0 = \frac{k g \Delta \rho \lambda_c}{\phi (1 - S_{br})}, & \frac{\partial h(x, t)}{\partial t} > 0, \\ \kappa_1 = \frac{k g \Delta \rho \lambda_c}{\phi (1 - S_{br} - S_{cr})}, & \frac{\partial h(x, t)}{\partial t} < 0. \end{cases} \quad (2.2.4)$$



## 2.3 Dimensionless Partial Differential Equation [17]

Advection-dominated migration is assumed, resulting in the following dimensionless scalings:

$$\xi = \frac{x}{L}, \quad \tau = \frac{t \kappa_1 \sin(\theta)}{L}, \quad \eta(\xi, \tau) = \frac{h(x, t)}{H}, \quad \sigma = \frac{\kappa}{\kappa_1}, \quad (2.3.1)$$

where  $L$  is a characteristic length along the impermeable cap, for example the initial extent of a typical plume as shown in Figure 2.1.1. Hence,  $\xi$  is the dimensionless spatial variable,  $\tau$  the non-dimensional advective characteristic time scale, and  $\eta \in [0, 1]$  is the fraction of the aquifer occupied by a  $\text{CO}_2$  plume, which is referred to as the dimensionless plume height. The residual surface of immobile  $\text{CO}_2$  remaining in the wake of the migrating plume is controlled by a dimensionless residual trapping parameter,  $\varepsilon = \frac{S_{cr}}{1-S_{br}} \in [0, 1]$ : when  $\varepsilon = 0$ , there is no pore space available to residually trap  $\text{CO}_2$ , whereas,  $\varepsilon = 1$  indicates an aquifer with all pore space available for sequestration of  $\text{CO}_2$ . Both  $\varepsilon$  and  $\mathcal{M}$  are constant material properties of a given, porous, isotropic aquifer filled with known fluids [14, 17, 21]. From (2.2.4) and (2.3.1), the switch parameter  $\sigma \in (0, 1]$  is given by

$$\sigma = \begin{cases} 1 - \varepsilon \leq 1, & \frac{\partial \eta(\xi, \tau)}{\partial \tau} > 0, \\ 1, & \frac{\partial \eta(\xi, \tau)}{\partial \tau} < 0. \end{cases} \quad (2.3.2)$$

As shown in Figure 2.3.1, when  $\eta_\tau > 0$ , the migrating  $\text{CO}_2$  is invading new pore spaces, and the switch parameter depends on the trapping parameter. Conversely, when the plume is draining and  $\eta_\tau < 0$ , no new trapping locations are sought, and the brine invades, isolating bubbles of  $\text{CO}_2$  in a residual surface. We define a quadratic function  $f$  as

$$f(\eta(\xi, \tau)) = \frac{\eta(\xi, \tau) (1 - \eta(\xi, \tau))}{\eta(\xi, \tau) (\mathcal{M} - 1) + 1}. \quad (2.3.3)$$

Combination of (2.3.3) and the fact that  $h(x, t) = H \eta(\xi, \tau)$  implies that equation (2.2.3) can be rewritten as

$$\frac{\partial h(x, t)}{\partial t} = \kappa \frac{\partial}{\partial x} \left( H f(\eta(\xi, \tau)) \left[ -\sin(\theta) + \frac{\partial h(x, t)}{\partial x} \cos(\theta) \right] \right).$$

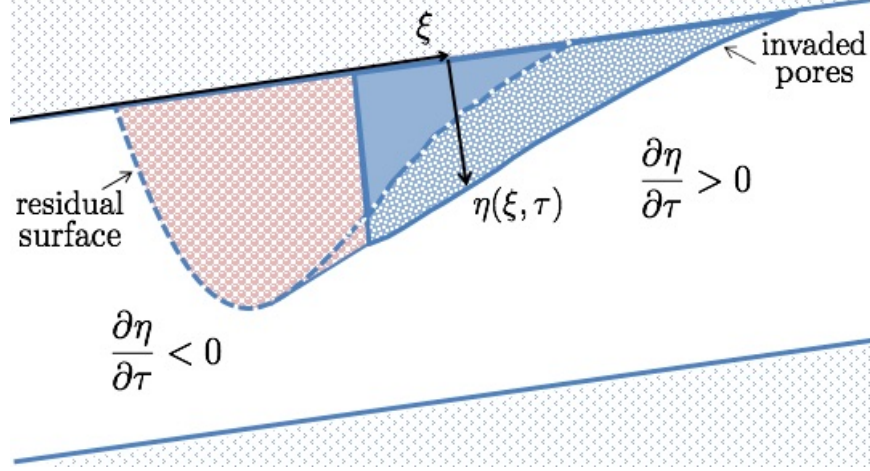


Figure 2.3.1: Shown in dimensionless variables, a residual area of immobile  $\text{CO}_2$  remains as the plume migrates to the right.

Substitution of the dimensionless variables from (2.3.1) into the previous expression yields

$$\begin{aligned} \frac{\kappa_1 \sin(\theta)}{L} \frac{\partial \eta(\xi, \tau)}{\partial \tau} &= -\frac{\kappa}{L} \frac{\partial}{\partial \xi} \left( f(\eta(\xi, \tau)) \sin(\theta) \right) + \frac{\kappa}{L} \frac{\partial}{\partial \xi} \left( \frac{\partial \eta(\xi, \tau)}{\partial \xi} \frac{H f(\eta(\xi, \tau)) \cos(\theta)}{L} \right) \\ \implies \frac{1}{\sigma} \frac{\partial \eta(\xi, \tau)}{\partial \tau} &= -\frac{\partial f(\eta(\xi, \tau))}{\partial \xi} + \frac{\partial}{\partial \xi} \left( \frac{\partial \eta(\xi, \tau)}{\partial \xi} \frac{H f(\eta(\xi, \tau))}{L \tan(\theta)} \right). \end{aligned}$$

The Péclet number,  $Pe = \frac{L \tan(\theta)}{H} > 0$ , and it follows that

$$\frac{1}{\sigma} \frac{\partial \eta(\xi, \tau)}{\partial \tau} + \frac{\partial f(\eta(\xi, \tau))}{\partial \xi} = \frac{1}{Pe} \frac{\partial}{\partial \xi} \left( f(\eta(\xi, \tau)) \frac{\partial \eta(\xi, \tau)}{\partial \xi} \right).$$

In a sloping aquifer, advection dominates diffusion, so  $Pe$  is large because the Péclet number represents the ratio of the rate of advection of a physical quantity by the flow to the rate of diffusion of the same quantity. As  $Pe \rightarrow \infty$  in the aforementioned equation, we obtain a first order partial differential equation given by [17]:

$$\frac{\partial \eta(\xi, \tau)}{\partial \tau} + \frac{\partial}{\partial \xi} \left( \sigma f(\eta(\xi, \tau)) \right) = 0, \quad (2.3.4)$$

where  $\sigma$  is a function of  $\frac{\partial \eta(\xi, \tau)}{\partial \tau}$ . The conservation law given in (2.3.4) is a scalar equation that is non-dimensional, quasi-linear, and hyperbolic.

## 2.4 Summary of the Dual Flux Model

In this section, we compile the relevant components of the governing equation that are frequently referenced as we move forth through this dissertation. It is convenient to introduce subscript notation rather than partial notation, so it follows from (2.3.2) that the switch parameter  $\sigma \in (0, 1]$  is given by

$$\sigma = \begin{cases} 1 - \varepsilon, & \eta_\tau > 0, \\ 1, & \eta_\tau < 0, \end{cases} \quad (2.4.1)$$

for trapping parameter  $\varepsilon \in [0, 1)$ . From [17] and (2.3.4), the evolution of a gravity current with residual trapping can be modeled as a nonlinear conservation law given by

$$\eta_\tau + (\sigma f(\eta))_\xi = 0, \quad (2.4.2)$$

in which the flux,  $\sigma f$ , is a fractional flow rate obtained by eliminating pressure from a version of Darcy's law. From (2.3.3), the flux function is

$$\sigma f(\eta) = \sigma \frac{\eta(1 - \eta)}{\eta(\mathcal{M} - 1) + 1}, \quad (2.4.3)$$

from which it follows that

$$\sigma f'(\eta) = \sigma \frac{\eta^2(1 - \mathcal{M}) - 2\eta + 1}{[\eta(\mathcal{M} - 1) + 1]^2}. \quad (2.4.4)$$

The switch between migration and deposition represented by the parameter  $\sigma = \sigma(\eta_\tau)$  gives rise to discontinuities in the flux, (2.4.3). Dual flux curves emerge in this model and are shown in Figure 2.4.1. The lower flux curve describes the invasion of the plume into pore space, and the upper flux captures the flow as the plume leaves CO<sub>2</sub> bubbles behind, which are then trapped by brine in the pore space. The value  $\eta = \eta^*$  with  $f'(\eta^*) = 0$  plays a significant role in the construction of admissible shock solutions of (2.4.2). For the flux function (2.4.3), we have

$$\eta^* = \frac{1}{1 + \sqrt{\mathcal{M}}}.$$

Flux functions with discontinuities in space have been previously studied, [8, 29, 39]; however, the flux in this model depends on the sign of  $\eta_\tau$ , a different kind of discontinuity that introduces new phenomena. For  $\varepsilon = 0$ , there is a single flux function; the aquifer has no available pore space to trap CO<sub>2</sub>, and the plume migrates according to the classical case in which the plume

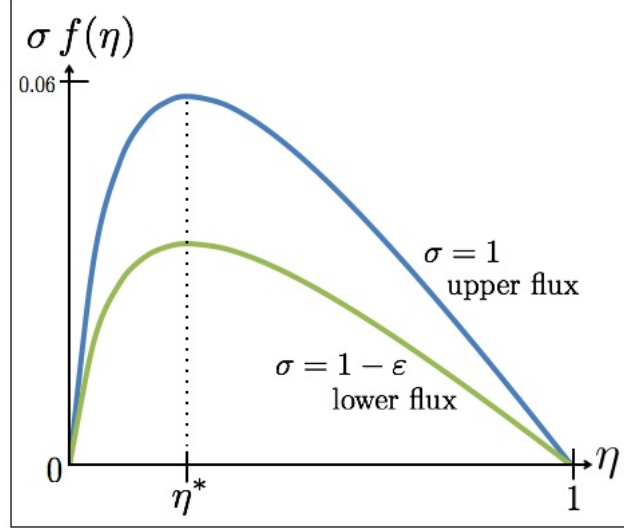


Figure 2.4.1: Dual fluxes (2.4.3) for  $\mathcal{M} = 10$  and  $\varepsilon = 0.4$ . Both flux curves attain a maximum value at  $\eta^* = 1 / (1 + \sqrt{\mathcal{M}})$ . The characteristic speeds satisfy  $0 < (1 - \varepsilon) f'(\eta) < f'(\eta)$  if  $\eta < \eta^*$ , and  $f'(\eta) < (1 - \varepsilon) f'(\eta) < 0$  if  $\eta > \eta^*$ .

volume remains fixed and would migrate indefinitely with no deposition. Typically  $\varepsilon \in (0, 1)$  in geologic storage [17, 21, 33, 36], and the entire compactly supported plume may be trapped within available pore space after a finite time and within a finite aquifer volume.

---

Characteristics and Shocks

---

In this chapter, we explain the role of the discontinuous switch parameter, see (2.4.1), in the construction of shocks and rarefactions. We also resolve an ambiguity, related to the constant regions of  $\eta$  in the characteristic plane, by introducing cross-hatch characteristics.

### 3.1 Cross-hatch Characteristics

Since the switch parameter,  $\sigma$ , is not defined when  $\eta_\tau = 0$ , the characteristic speed is not well-defined in regions of the characteristic plane where the solution is constant. To resolve this, we include characteristics determined by both flux curves at each point where  $\eta_\tau = 0$ ; we refer to the characteristics as *cross-hatch characteristics* since they form a cross-hatch pattern in regions where  $\eta$  is constant. This new pattern of characteristics is illustrated in Figure 3.2.2(a). The two possible characteristic speeds are  $\sigma f'(\eta)$  with  $\sigma = 1$  or  $\sigma = 1 - \varepsilon$  in equation (2.4.4). We refer to the larger or greater characteristic speed as the *faster* speed, and the other characteristic speed as the *slower* speed. In constant regions of the characteristic plane with cross-hatch characteristics, *faster characteristics* travel with the faster characteristic speed, and *slower characteristics* travel with the slower characteristic speed. The faster and slower characteristics as in Definition 3.1.1 are shown on the dual flux curves in Figure 3.1.1.

**Definition 3.1.1.** (a) If  $\eta < \eta^*$ , the faster speed is  $f'(\eta)$ , and the slower speed is  $(1 - \varepsilon) f'(\eta)$ .  
(b) If  $\eta > \eta^*$ , the faster characteristic speed is  $(1 - \varepsilon) f'(\eta)$ , and the slower speed is  $f'(\eta)$ .

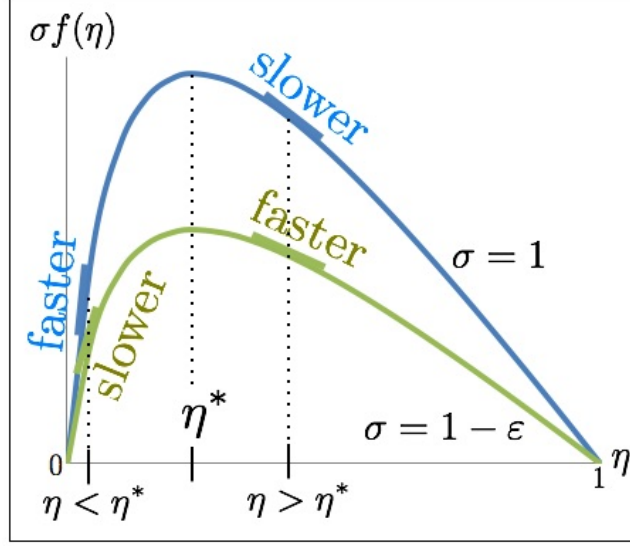


Figure 3.1.1: For  $\eta < \eta^*$ ,  $0 < (1 - \epsilon)f'(\eta) < f'(\eta)$ , and for  $\eta > \eta^*$ ,  $f'(\eta) < (1 - \epsilon)f'(\eta) < 0$ .

The reason for introducing cross-hatch characteristics becomes apparent when considering initial value problems similar to one considered in Hesse, Orr, and Tchelepi. In [17], the characteristic portrait in Figure 7 has a gap with no characteristics in a region with constant solution. We resolve this non-physical gap by including cross-hatch characteristics, ensuring that the solution value at any point in the characteristic plane can be obtained by tracing characteristics back to the initial condition. The particular example of Figure 4.2.1 exhibits a shock curve on which the shock speed becomes one of the characteristic speeds at a time  $\tau_{\text{graze}}$ , thus risking loss of admissibility. Continuation of the solution for  $\tau > \tau_{\text{graze}}$  then depends on cross-hatch characteristics, as explained in Section 4.2. Another example with a solution that relies on cross-hatch characteristics is given in Chapter 6.

## 3.2 Shocks

The Riemann problem composed of equation (2.4.2) and initial condition

$$\eta(\xi, 0) = \begin{cases} \eta_L, & \xi < 0, \\ \eta_R, & \xi > 0, \end{cases}$$

has discontinuous weak solutions known as shock waves. Consider the piecewise constant function

$$\eta(\xi, \tau) = \begin{cases} \eta_L, & \xi < \Lambda \tau, \\ \eta_R, & \xi > \Lambda \tau \end{cases} \quad (3.2.1)$$

propagating with speed  $\Lambda$ . Since  $\sigma$  in (2.4.1) is selected by the sign of  $\eta_\tau$ , we set  $\sigma = 1$  if  $\eta$  jumps down, in the sense of distributions, across the shock as time increases; otherwise, if the jump is up, we set  $\sigma = 1 - \varepsilon$ . This fixes the value of  $\sigma$ , and we can write the Rankine-Hugoniot jump condition for the specific flux (2.4.3),

$$\Lambda = \frac{\sigma [f(\eta_R) - f(\eta_L)]}{\eta_R - \eta_L} = \frac{\sigma [1 - (\mathcal{M} - 1)\eta_R\eta_L - \eta_R - \eta_L]}{[\eta_R(\mathcal{M} - 1) + 1][\eta_L(\mathcal{M} - 1) + 1]}. \quad (3.2.2)$$

Hesse et al. [17] justified the choice of  $\sigma$  in a slightly different way by including dissipative terms that smooth the shock.

For a scalar conservation law with a single flux function, admissible shocks satisfy the Lax entropy condition, requiring characteristics to enter the shock on both sides [25]. Here, with two fluxes, we specify shock admissibility as follows:

**Definition 3.2.1.** *The shock wave (3.2.1) is admissible if and only if the faster characteristics enter the shock from both sides. See Figure 3.2.1.*

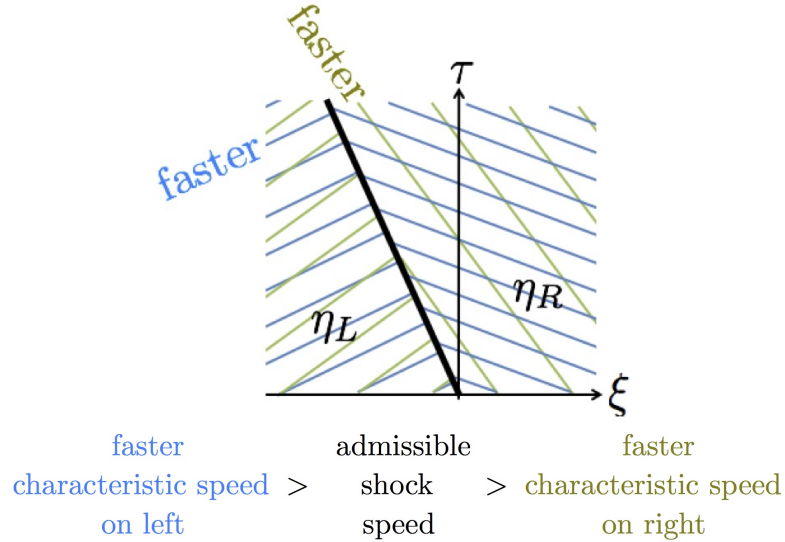


Figure 3.2.1: Faster characteristics on each side of admissible shock impinge on the shock.

Thus, for (3.2.1), we require  $f'(\eta_L) > f'(\eta_R)$ . Since the flux is concave,  $\eta_L < \eta_R$  is necessary for an admissible shock, just as it would be for a single flux equation. Such a step up is shown in Figure 3.2.5(a). As shown in Figure 3.2.2(a),  $\eta_\tau < 0$  across a forward shock (i.e., with  $\Lambda > 0$ ), so that  $\sigma = 1$ . Consequently, not only is  $\Lambda$  determined from the upper flux curve, but also the faster characteristics enter the shock, see Figure 3.2.2(b). For an admissible backward shock, with  $\Lambda < 0$ , we have  $\sigma = 1 - \varepsilon$ , and the shock is admissible if and only if the characteristics found on the lower flux curve impinge on the shock on the right, because they are the less negative characteristics, and enter the shock on the left because either they are the faster characteristics (if  $\eta_L > \eta^*$ ), or both families have positive speed (if  $\eta_L < \eta^*$ ), as shown in Figure 3.2.3.

The following Lemma states that all characteristics enter an admissible shock unless the slower family leaves on the left, as shown in Figure 3.2.4.

**Lemma 3.2.2.** *The only characteristics that can leave an admissible shock belong to the slower family, and are on the left of the shock.*

**Proof:** Consider an admissible shock (3.2.1). If  $\eta_R < \eta^*$ , the faster characteristic speed is on the upper flux, so  $f'(\eta_R) < \Lambda$  is required. Thus,  $(1 - \varepsilon) f'(\eta_R) < \Lambda$  also. Hence, both characteristics on the right impinge on the shock. If  $\eta_R > \eta^*$ , the faster characteristic speed is on the lower flux curve, so admissibility requires  $(1 - \varepsilon) f'(\eta_R) < \Lambda$ . Since  $\eta_R > \eta^*$ ,  $f'(\eta_R) < (1 - \varepsilon) f'(\eta_R)$ , and the slower characteristic on the right also enters the shock. Hence, both characteristics on the right always impinge on an admissible shock.

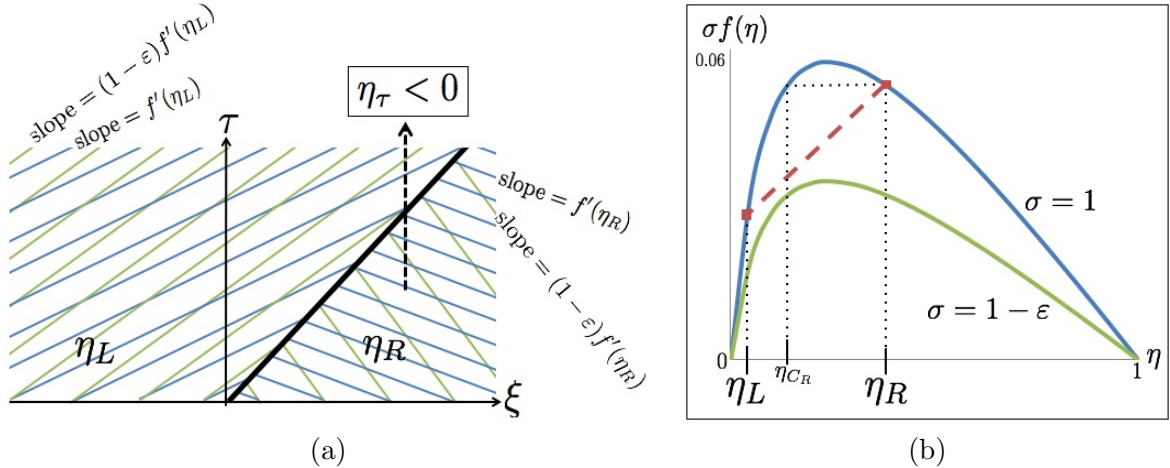


Figure 3.2.2: A forward shock with  $\Lambda > 0$ . (a) Characteristic plane with cross-hatch characteristics in constant regions. (b) Shock speed determined from the upper flux curve.



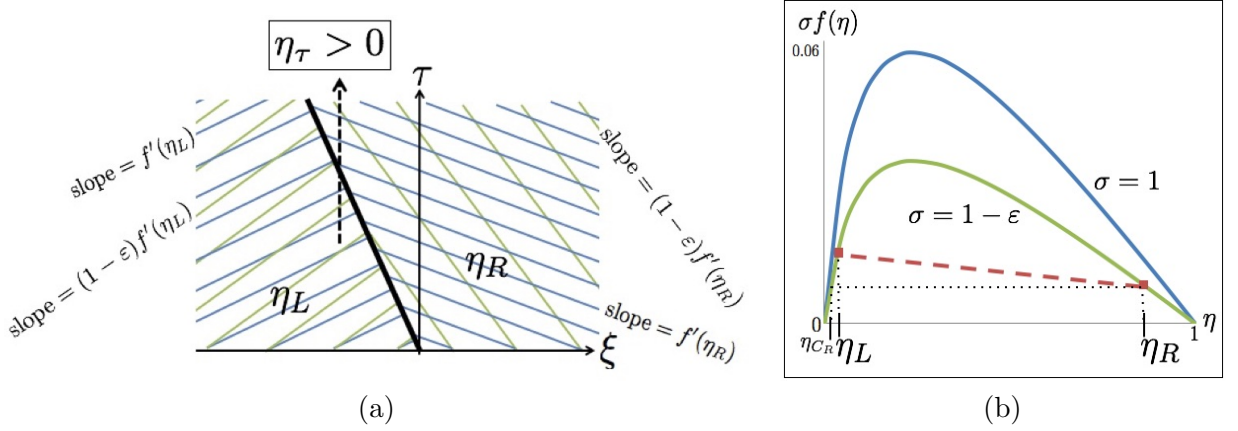


Figure 3.2.3: Backward shock,  $\Lambda < 0$ , for which (a)  $\eta_\tau > 0$ , so the shock speed is found from the lower flux curve, (b).

If  $\eta_L < \eta^* < \eta_R$  yields a backward shock, both characteristics on the left have positive speed whilst the shock speed is negative, so both characteristics on the left must enter the shock.

When  $\eta_L < \eta^*$  results in a forward shock to  $\eta_R$ , the faster characteristic entering the shock from the left has speed  $f'(\eta_L) > \Lambda$ , since  $\sigma = 1$ . If  $\Lambda < (1 - \epsilon) f'(\eta_L)$ , the slower characteristics will also impinge on the forward shock; however, it is possible that  $(1 - \epsilon) f'(\eta_L) < \Lambda$ , in which case the slower characteristics on the left emanate from the shock. Similarly, if  $\eta^* < \eta_L$ , an admissible shock requires  $0 > \sigma f'(\eta_L) > \Lambda$  for  $\sigma = 1 - \epsilon$ . The more negative characteristic speed  $f'(\eta_L)$  may or may not satisfy  $f'(\eta_L) > \Lambda$ , so the slower characteristics on the left can leave the shock.

In summary, since the faster characteristics must impinge on the shock from both sides, the slower characteristics on the right also enter the shock, but the slower characteristics on the left can leave the shock, as in Figure 3.2.4(b).  $\square$

For a constant  $\eta = \eta_J \neq \eta^*$ , there exists  $\eta_{C_J} \neq \eta_J$  such that  $f(\eta_{C_J}) = f(\eta_J)$ . For the flux (2.4.3),  $\eta_{C_J}$  is given by

$$\eta_{C_J} = \frac{1 - \eta_J}{(\mathcal{M} - 1)\eta_J + 1}. \quad (3.2.3)$$

For example, in Figure 3.2.2(b), we show  $\eta_R > \eta^*$  and the corresponding  $\eta_{C_R}$ . If  $\eta_L = \eta_{C_R}$ , then the shock (3.2.1) is stationary,  $\Lambda = 0$ , which can be calculated from either flux curve.

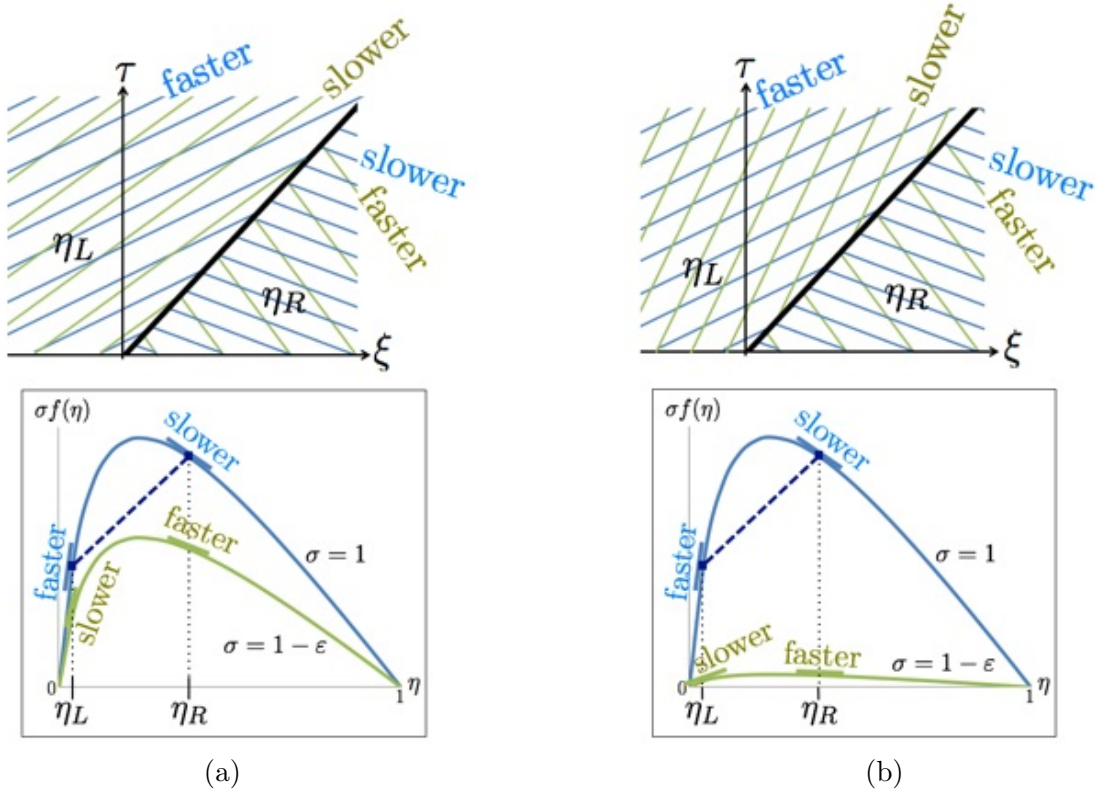


Figure 3.2.4: (a) All four characteristics enter admissible shock. (b) Slower characteristics on left leave admissible shock.

In Figure 3.2.5 we show the three types of shock waves (3.2.1) as sharp jumps in the plume interface height. Any centered solution (3.2.1) can be shifted away from the origin since (2.4.2) is translationally invariant. A shock wave emanating from a position  $\xi = \tilde{\xi}$  is a mathematical representation of the physically relevant sharp vertical interface between the  $\text{CO}_2$  plume and brine within the aquifer given by the initial condition where plume to the right of  $\tilde{\xi}$  has a larger height than the plume on the left, as shown in Figure 3.2.5(b). When  $\eta_L < \eta_R$ , (3.2.1) yields a shock wave solution where the interface between plume and underlying brine maintains its initial shape and travels with speed  $\Lambda$ . When  $\Lambda = 0$ , the stationary shock shown in Figure 3.2.5(b) persists at the location of the initial discontinuity,  $\tilde{\xi}$ , shown in Figure 3.2.5(a). For a forward shock to the right, the interface leaves a residual surface in the plume's wake, containing a region of trapped residual bubbles, as shown in Figure 3.2.5(c). Hence, the use of the upper flux curve with switch parameter  $\sigma = 1$  during the construction of forward shocks is justified. For backward shocks, shown in Figure 3.2.5(d), new pore spaces are available for  $\text{CO}_2$  to fill as the plume advances to the left, so the switch parameter depends on trapping, and  $\sigma = 1 - \varepsilon$ .

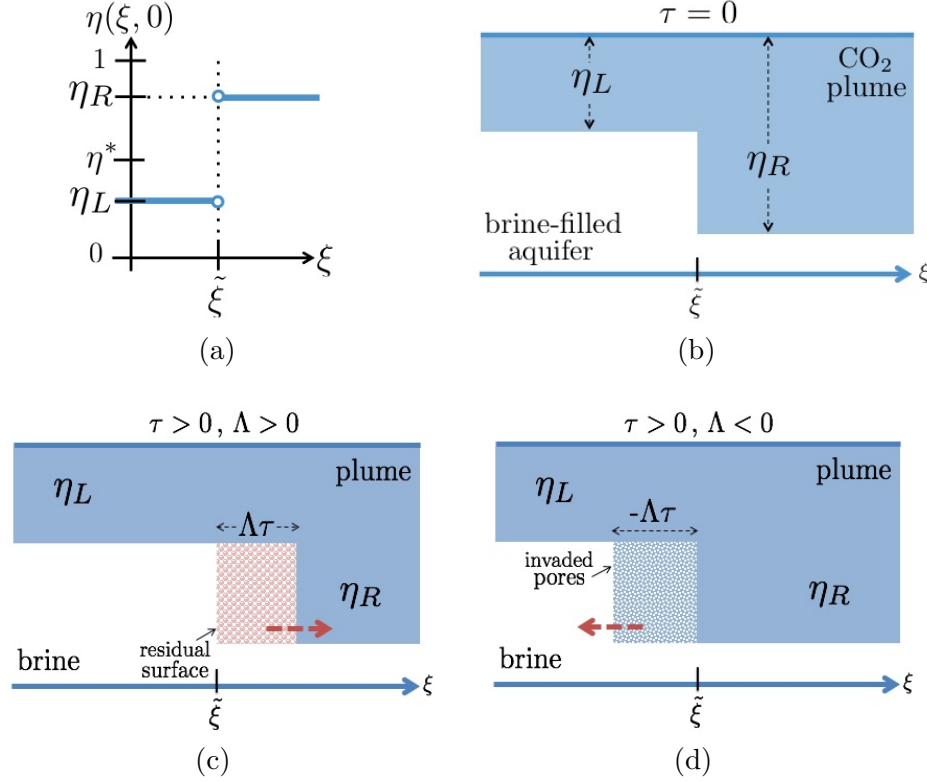


Figure 3.2.5: (a) An initial step up yields a shock wave. (b) Stationary vertical interface between brine and CO<sub>2</sub> plume,  $\Lambda = 0$ . (c) Forward shock,  $\Lambda > 0$ . (d) Backward shock,  $\Lambda < 0$ .

### 3.3 Expansion Shocks

We consider expansion shocks because we will need them in Chapter 4 as approximations to rarefactions in wave-front tracking. For scalar conservation laws, expansion shocks have characteristics leaving the shock in forward time on both sides of the shock, as shown in Figure 3.3.1. In our case, we can have two characteristic speeds on either side of a shock. Analogous to Definition 4.2.1, it turns out to be appropriate to define a shock to be an expansion shock if the slower characteristics on each side emanate from the shock, Figure 3.3.1. Following a similar argument as in the proof of Lemma 4.2.2, the faster characteristics on the right also leave the shock, but the faster characteristics on the left may or may not enter the shock, as shown in Figure 3.3.2. Consider a shock wave solution (3.2.1). We have shown that if  $\eta_R > \eta_L$ , then the shock is admissible, and the faster characteristics enter the shock from both sides. If  $\eta_R < \eta_L$ , we argue that the shock is necessarily an expansion shock. For forward expansion shocks,  $\Lambda > 0$  is determined in (3.2.2) with  $\sigma = 1 - \varepsilon$  since  $\eta_\tau > 0$  in the sense of distributions.

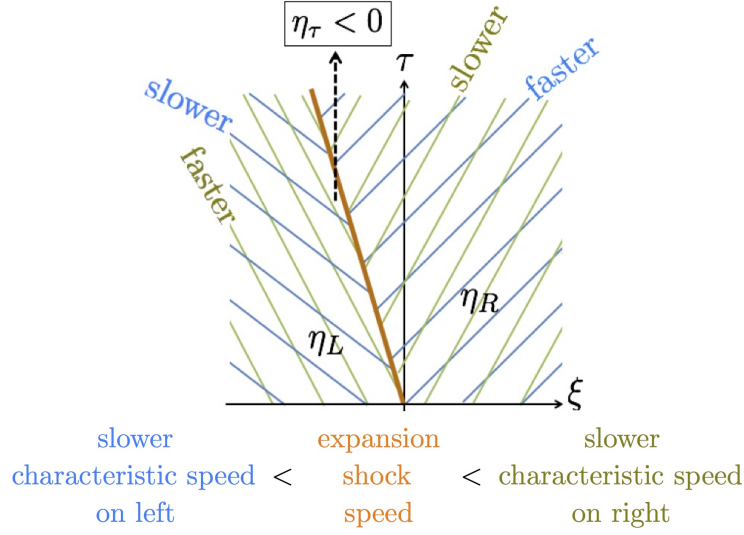


Figure 3.3.1: Slower characteristics on each side of admissible shock leave the shock in forward time.

The corresponding characteristics, with speed  $(1 - \varepsilon) f'(\eta)$ , leave the shock on both sides. It follows that the shock is an expansion shock. Similarly, for  $\Lambda < 0$ , we have  $\sigma = 1$  in (3.2.2), and the characteristics with speed  $f'(\eta)$  leave the backward shock, which is necessarily an expansion shock.

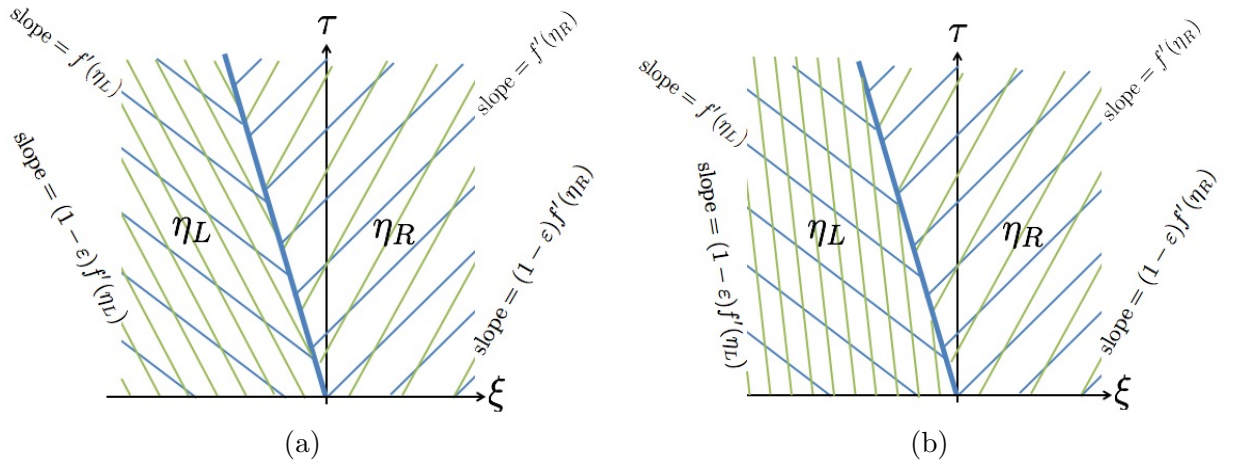


Figure 3.3.2: Backward expansion shock. (a) All characteristics leave the shock. (b) The faster characteristics on the left, with speed  $(1 - \varepsilon) f'(\eta_L)$ , enter the shock.

### 3.4 Rarefactions

Centered rarefaction fans are continuous weak solutions of (2.4.2) and have the form

$$\eta(\xi, \tau) = \begin{cases} \eta_L, & \frac{\xi}{\tau} < \sigma f'(\eta_L), \\ \tilde{\eta}\left(\frac{\xi}{\tau}\right), & \sigma f'(\eta_L) < \frac{\xi}{\tau} < \sigma f'(\eta_R), \\ \eta_R, & \sigma f'(\eta_R) < \frac{\xi}{\tau}, \end{cases} \quad (3.4.1)$$

where  $\tilde{\eta}$  is a function of the similarity variable  $\xi/\tau$ . The method of characteristics reduces the construction of a solution to the conservation law given by (2.4.2) to solving ordinary differential equations throughout the solution space; hence, the speed of the characteristics is  $d\xi/d\tau = \sigma f'(\eta)$ , and, for the flux (2.4.3), the function  $\tilde{\eta}$  in (3.4.1) is given by

$$\tilde{\eta}\left(\frac{\xi}{\tau}\right) = \begin{cases} \frac{\xi(1 - \mathcal{M}) - \sigma\tau + \sqrt{\mathcal{M}\sigma\tau[\xi(\mathcal{M} - 1) + \sigma\tau]}}{(\mathcal{M} - 1)[\xi(\mathcal{M} - 1) + \sigma\tau]}, & \mathcal{M} \neq 1, \\ \frac{1}{2} \left[ 1 - \frac{\xi}{\sigma\tau} \right], & \mathcal{M} = 1. \end{cases} \quad (3.4.2)$$

In Figure 3.4.1(a) we show a rarefaction wave approximated by three expansion shocks; from left to right, the expansion shocks have increasing speeds. *Expansion shocks approximating a rarefaction do not approach.* The rarefaction with  $\eta_R < \eta^* < \eta_L$  in Figure 3.4.1(b) has both forward and backward characteristics with speeds that depend on the value of  $\sigma$ , as explained in the figure caption.

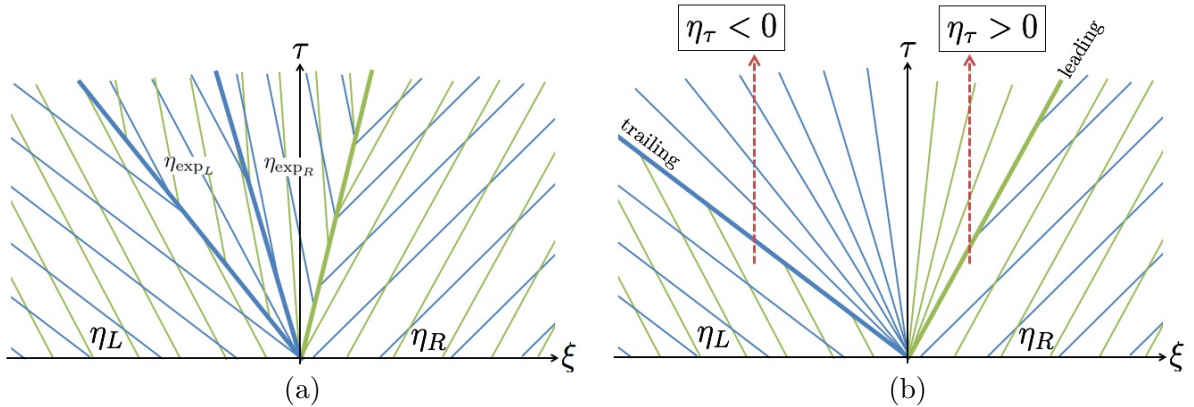


Figure 3.4.1: (a) Three expansion shocks approximating a centered rarefaction wave. Since  $\eta$  is necessarily decreasing from left to right in the rarefaction wave, we have that  $\eta_{\tau} < 0$  left of the  $\tau$  axis, so that  $\sigma = 1$ , as indicated in (b). To the right,  $\eta_{\tau} > 0$ , so that  $\sigma = 1 - \varepsilon$  there.

In the limit, an admissible rarefaction fan is indeed approximated by an increasing number of expansion shocks. Since we require  $\sigma f'(\eta_L) < \sigma f'(\eta_R)$  to yield a rarefaction, it follows that  $\eta_R < \eta_L$ . In Figure 3.4.2, we show the construction of a rarefaction wave, resolving a step down in  $\eta$ , using both flux functions.

The rarefaction solution, given by (3.4.1) and (3.4.2), varies continuously from  $\eta_L$  to  $\eta_R$  in Figure 3.4.1(b). Note  $\tilde{\eta}$  is continuous across  $\xi = 0$  even though  $\sigma$  in (3.4.2) has a discontinuity at this position [17]. However, there is a discontinuity in the slope of the plume interface due to the jump in  $\sigma$ . The discontinuity in the flux function captures the slope discontinuity between the CO<sub>2</sub> plume and underlying brine in the physical system at the position where the plume invades new portions of the aquifer. From (3.4.2), we calculate the derivative

$$\tilde{\eta}_\xi = \begin{cases} \frac{-\sqrt{\mathcal{M}\sigma\tau}}{2[\xi(\mathcal{M}-1) + \sigma\tau]^{3/2}}, & \mathcal{M} \neq 1, \\ -\frac{1}{2\sigma\tau}, & \mathcal{M} = 1. \end{cases} \quad (3.4.3)$$

From (3.4.3), we calculate the jump in the derivative  $\eta_\xi(\xi/\tau)$  at  $\xi = 0$ , where  $f'(\eta) = 0$ , and  $\sigma$

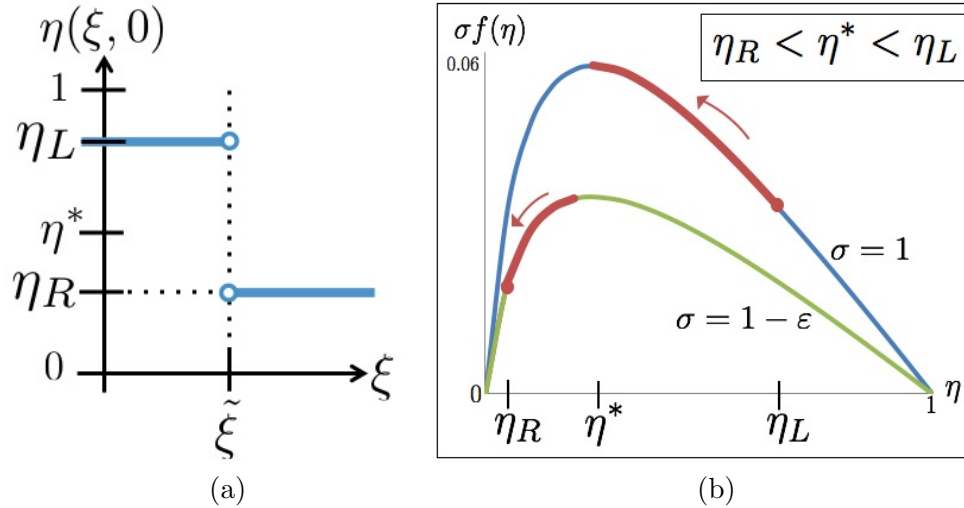


Figure 3.4.2: (a) A step down yields a rarefaction fan. (b) With parameters  $\mathcal{M} = 10$ ,  $\varepsilon = 0.4$ , the upper flux curve is traversed by  $(\tilde{\eta}, \sigma f(\tilde{\eta}))$  as the rarefaction fans from  $\eta_L$  down to  $\eta^*$ , then jumps down to the lower flux curve as the solution decreases from  $\eta^*$  to  $\eta_R$ .

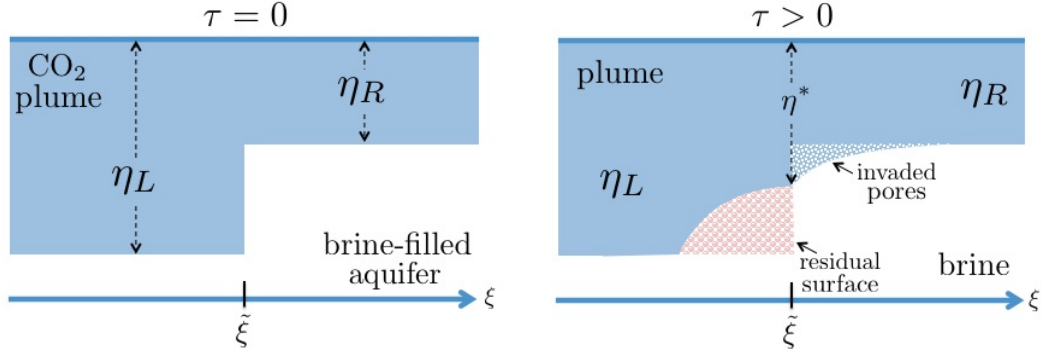


Figure 3.4.3: A rarefaction wave propagating left and right. The discontinuity in  $\sigma$  corresponds to a discontinuity in the interface slope.

switches from  $\sigma = 1$  to  $\sigma = 1 - \varepsilon$  :

$$[\eta_\xi] = \frac{\sqrt{\mathcal{M}}}{2\tau} \frac{\varepsilon}{1 - \varepsilon}. \quad (3.4.4)$$

The discontinuous slope  $\eta_\xi$  at  $\xi = \tilde{\xi}$  is shown in Figure 3.4.3 for the case where  $\eta_R < \eta^* < \eta_L$ . The plume is migrating to the right, leaving a region of trapped residual bubbles with  $\xi < \tilde{\xi}$  and invading new pores where  $\xi > \tilde{\xi}$ .



It follows from Chapter 3 that the solution of the Riemann problem

$$\begin{cases} \eta_\tau + (\sigma f(\eta))_\xi = 0, & \xi \in \mathbb{R}, \tau > 0, \\ \eta(\xi, 0) = \begin{cases} \eta_L, & \xi < 0, \\ \eta_R, & \xi > 0 \end{cases} \end{cases}$$

is a classical compressive shock if  $\eta_L < \eta_R$  and a rarefaction fan if  $\eta_L > \eta_R$ . While the structure of these individual waves depends on the details of two flux functions and the switch between them, the outcome is, broadly speaking, the same as for a convex scalar conservation law with a single flux.

In this chapter, we consider pairs of Riemann problems, demonstrating differences from properties of scalar equations with a single flux. Each Riemann problem generates a single wave; we are interested in whether or not the waves interact, and the result of the interaction.

## 4.1 Catalog of Interactions

A detailed classification of all combinations of left-hand waves from  $\eta_L$  to  $\eta_M$  paired with right-hand waves from  $\eta_M$  to  $\eta_R$  yielded a complete catalog of interactions. For  $\eta_L$  and  $\eta_R$  different from  $\eta_M$ , consider initial data of the form:



$$\eta(\xi, 0) = \begin{cases} \eta_L, & \xi < \xi_1, \\ \eta_M, & \xi_1 < \xi < \xi_2, \\ \eta_R, & \xi_2 < \xi. \end{cases} \quad (4.1.1)$$

There are eight possible pairs of a left-hand and a right-hand wave, as shown in Figure 4.1.1. Due to the shape of the discontinuous flux function, the eight possible initial conditions with three constant states can be further divided, and these specific pairings are listed in Table 4.1.

We focus on the main features of solutions of initial value problems with initial data of the form (4.1.1) that were obtained during the complicated classification. We noted similarities between the solutions of different pairs, see Figure 4.1.2, and restructured the original pairs into four broad cases. Similar to the classical case with a single concave flux function, if  $\eta(\xi, 0)$  is decreasing,  $\eta_L > \eta_M > \eta_R$  as in Pair 8, then the solution consists of two rarefaction waves that do not approach, see Figure 4.3.1(a). Consequently, since the speed of an approximating expansion shock is between the speeds of the corresponding rarefaction's trailing and leading characteristics, two expansion shocks will not approach.

We treat the three remaining continuous cases in turn, and, if the data has an initial rarefaction, we examine the interactions involving expansion shock approximations. Case A has a shock wave on the left and a rarefaction on the right and encompasses Pairs 1-3. Case B has  $\eta(\xi, 0)$

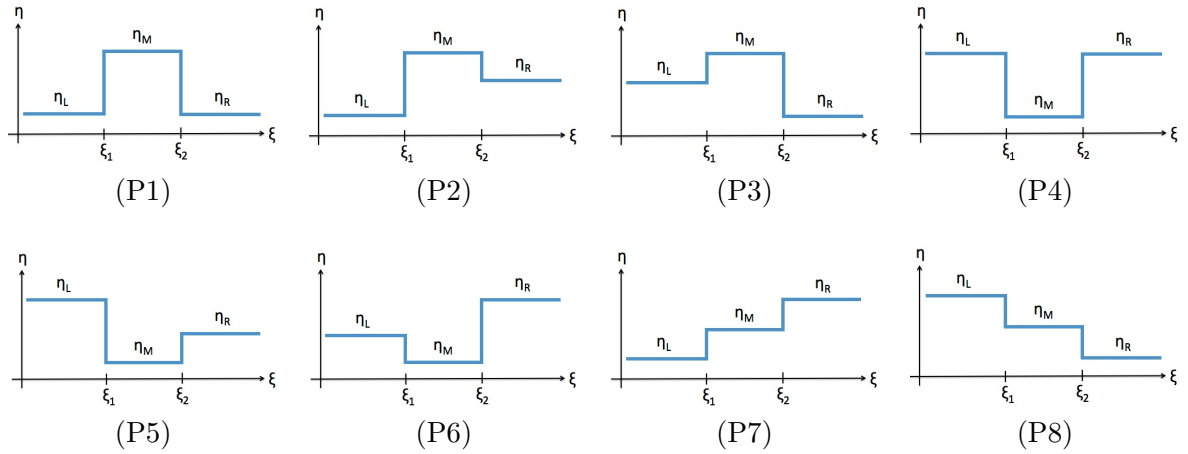


Figure 4.1.1: Initial condition with (P1)  $\eta_L = \eta_R < \eta_M$ , (P2)  $\eta_L < \eta_R < \eta_M$ , (P3)  $\eta_R < \eta_L < \eta_M$ , (P4)  $\eta_M < \eta_L = \eta_R$ , (P5)  $\eta_M < \eta_R < \eta_L$ , (P6)  $\eta_M < \eta_L < \eta_R$ , (P7)  $\eta_L < \eta_M < \eta_R$ , and (P8)  $\eta_R < \eta_M < \eta_L$ .

Table 4.1: Possible initial conditions with three states.

<b>Pair 1</b> $\eta_L = \eta_R < \eta_M$		<b>Pair 5</b> $\eta_M < \eta_R < \eta_L$	
a	$\eta_L = \eta_R < \eta_M < \eta^*$	a	$\eta_M < \eta_R < \eta_L < \eta^*$
b	$\eta_L = \eta_R < \eta_{C_M} < \eta^* \leq \eta_M$	b	$\eta_M < \eta_R < \eta^* < \eta_L$
c	$\eta_L = \eta_R = \eta_{C_M} < \eta^* < \eta_M$	c	$\eta_M < \eta_{C_R} < \eta^* < \eta_R < \eta_L$
d	$\eta_{C_M} < \eta_L = \eta_R < \eta^* < \eta_M$	d	$\eta_M = \eta_{C_R} < \eta^* < \eta_R < \eta_L$
e	$\eta^* \leq \eta_L = \eta_R < \eta_M$	e	$\eta_{C_R} < \eta_M < \eta^* < \eta_R < \eta_L$
<b>Pair 2</b> $\eta_L < \eta_R < \eta_M$		<b>Pair 6</b> $\eta_M < \eta_L < \eta_R$	
a	$\eta_L < \eta_R < \eta_M < \eta^*$	a	$\eta_M < \eta_L < \eta_R < \eta^*$
b	$\eta_L < \eta_R < \eta^* < \eta_M$ with $\eta_L < \eta_{C_M}$	b	$\eta_M < \eta_L < \eta^* < \eta_R$ with $\eta_M < \eta_{C_R}$
c	$\eta_L = \eta_{C_M} < \eta_R < \eta^* < \eta_M$	c	$\eta_M = \eta_{C_R} < \eta_L < \eta^* < \eta_R$
d	$\eta_{C_M} < \eta_L < \eta_R < \eta^* < \eta_M$	d	$\eta_{C_R} < \eta_M < \eta_L < \eta^* < \eta_R$
e	$\eta_L < \eta_{C_M} < \eta^* < \eta_R < \eta_M$	e	$\eta_M < \eta_{C_R} < \eta^* < \eta_L < \eta_R$
f	$\eta_L = \eta_{C_M} < \eta^* < \eta_R < \eta_M$	f	$\eta_M = \eta_{C_R} < \eta^* < \eta_L < \eta_R$
g	$\eta_{C_M} < \eta_L < \eta^* < \eta_R < \eta_M$	g	$\eta_{C_R} < \eta_M < \eta^* < \eta_L < \eta_R$
h	$\eta^* < \eta_L < \eta_R < \eta_M$	h	$\eta^* < \eta_M < \eta_L < \eta_R$
<b>Pair 3</b> $\eta_R < \eta_L < \eta_M$		<b>Pair 7</b> $\eta_L < \eta_M < \eta_R$	
a	$\eta_R < \eta_L < \eta_M < \eta^*$	a	$\eta_L < \eta_M < \eta_R < \eta^*$
b	$\eta_R < \eta_L < \eta_{C_M} < \eta^* < \eta_M$	b	$\eta_L < \eta_M < \eta_{C_R} < \eta^* < \eta_R$
c	$\eta_R < \eta_L = \eta_{C_M} < \eta^* < \eta_M$	c	$\eta_L < \eta_M = \eta_{C_R} < \eta^* < \eta_R$
d	$\eta_R < \eta_L < \eta^* < \eta_M$ with $\eta_{C_M} < \eta_L$	d	$\eta_L < \eta_M < \eta^* < \eta_R$ with $\eta_{C_R} < \eta_M$
e	$\eta_R < \eta^* < \eta_L < \eta_M$	e	$\eta_L < \eta_{C_M} < \eta^* < \eta_M < \eta_R$
f	$\eta^* < \eta_R < \eta_L < \eta_M$	f	$\eta_L = \eta_{C_M} < \eta^* < \eta_M < \eta_R$
<b>Pair 4</b> $\eta_M < \eta_L = \eta_R$		g	$\eta_{C_M} < \eta_L < \eta^* < \eta_M < \eta_R$
a	$\eta_M < \eta_L = \eta_R < \eta^*$	h	$\eta^* < \eta_L < \eta_M < \eta_R$
b	$\eta_M < \eta_{C_R} < \eta^* < \eta_L = \eta_R$	<b>Pair 8</b> $\eta_R < \eta_M < \eta_L$	
c	$\eta_M = \eta_{C_R} < \eta^* < \eta_L = \eta_R$	a	$\eta_R < \eta_M < \eta_L < \eta^*$
d	$\eta_{C_R} < \eta_M < \eta^* < \eta_L = \eta_R$	b	$\eta_R < \eta_M < \eta^* < \eta_L$
e	$\eta^* < \eta_M < \eta_L = \eta_R$	c	$\eta_R < \eta^* < \eta_M < \eta_L$
		d	$\eta^* < \eta_R < \eta_M < \eta_L$

increasing yielding two successive shock waves, as in Pair 7. Case C has a rarefaction-shock initial condition with a jump down then a jump up, as in Pairs 4-6.

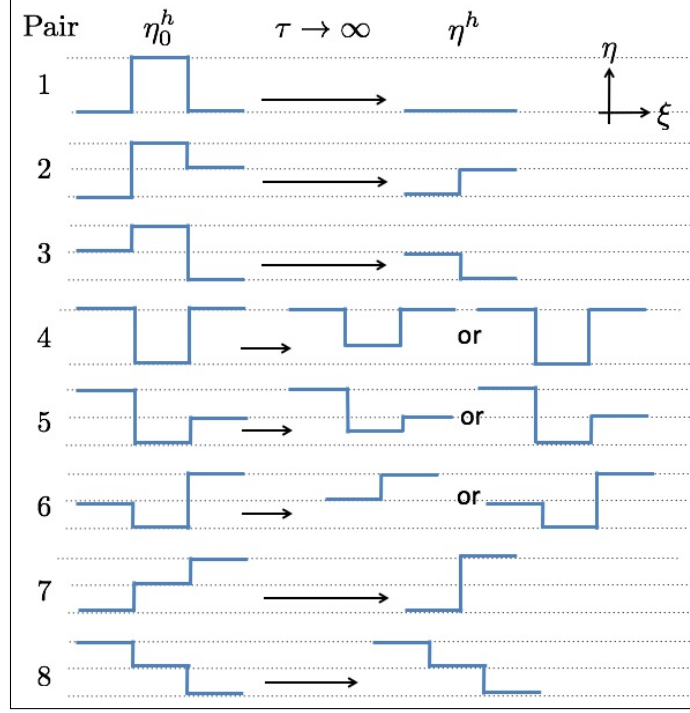


Figure 4.1.2: Summary of results for eight possible initial pairings.

## 4.2 Case A: Shock - Rarefaction: $\eta_L < \eta_M$ and $\eta_R < \eta_M$

In this case, we have a shock with speed  $\Lambda$  emanating from  $\xi_1$  and a rarefaction centered at  $\xi_2 > \xi_1$ . To see that the two waves approach, we check that the shock speed is greater than the speed of the trailing characteristic in the rarefaction. There are two cases to consider, (i)  $\Lambda > 0$  and (ii)  $\Lambda < 0$ . In case (i), the shock admissibility condition requires  $f'(\eta_M) < \Lambda$ , so that the speed  $\sigma f'(\eta_M)$  of the trailing edge of the rarefaction is less than the shock speed, whether  $\eta_M < \eta^*$ , for which  $\sigma = 1 - \varepsilon$ , or  $\eta_M > \eta^*$ , for which  $\sigma = 1$ . In case (ii), we have  $\Lambda < 0$  and  $\eta_\tau > 0$ . Thus,  $\eta_M > \eta^*$  but now shock admissibility requires  $(1 - \varepsilon) f'(\eta_M) < \Lambda$ , and the rarefaction, with trailing edge traveling at speed  $f'(\eta_M) < (1 - \varepsilon) f'(\eta_M) < \Lambda < 0$ , approaches the shock. Therefore, the trailing characteristic from the rarefaction on the right will always be slower than the shock on the left, so the discontinuities always approach in Case A.

### 4.2.1 Case A: Example

In this example, we derive the analytic solution and illustrate basic shock construction in the characteristic plane for a specific Case A interaction. The exact solution is plotted in the characteristic plane, Figure 4.2.1(b), and the code that generated the plot is included in Appendix B.1. For demonstrative purposes, we consider a specific Pair 2d initial condition with  $\mathcal{M} = 1$ . Since  $\eta_{C_M} < \eta_L$ , we begin with a backward shock from  $\eta_L$  up to  $\eta_M$  that emanates from  $\xi = \xi_1$ , and a rarefaction from  $\eta_M$  down to  $\eta_R$  centered at  $\xi = \xi_2$ . The negative shock speed is determined by the dark blue chord on the lower flux curve in Figure 4.2.1(a) and is  $\Lambda = \sigma(1 - \eta_M - \eta_L)$ , where  $\sigma = 1 - \varepsilon$ ; the backward shock in the characteristic plane is given by  $\xi = \Lambda\tau + \xi_1$  and is shown in dark blue in Figure 4.2.1(b). The trailing characteristic in the rarefaction has speed  $s_t = f'(\eta_M) < \Lambda$  and is a bold light blue line in Figure 4.2.1(b). The trailing characteristic begins to interact with the backward shock at transition time  $\tau_T = \frac{\xi_2 - \xi_1}{\Lambda - s_t}$  and transition position  $\xi_T = s_t \tau_T + \xi_2$ , shown as the cyan star in Figure 4.2.1(b). Since  $\xi_T < \xi_2$ , the characteristic speeds within the rarefaction from  $\eta_M$  down to  $\eta^*$  are determined with  $\sigma = 1$ , and for  $(\xi, \tau)$ , the rarefaction solution is

$$\eta_{\text{rare}} = \frac{1}{2} \left[ 1 - \frac{\xi - \xi_2}{\tau} \right]. \quad (4.2.1)$$

In this region, a resulting backward shock from  $\eta_L$  up to  $\eta_{\text{rare}}$  emanating from  $(\xi_T, \tau_T)$  is given by

$$\frac{d\xi}{d\tau} = \sigma(1 - \eta_{\text{rare}} - \eta_L),$$

for  $\sigma = 1 - \varepsilon$ , which, when combined with (4.2.1) and solved, yields the shock position

$$\xi = \xi_2 + \left( \frac{\sigma}{2 - \sigma} \right) (1 - 2\eta_L) \tau + \left[ (\xi_T - \xi_2) \tau_T^{-\frac{\sigma}{2}} - \left( \frac{\sigma}{2 - \sigma} \right) (1 - 2\eta_L) \tau_T^{\frac{2 - \sigma}{2}} \right] \tau^{\frac{\sigma}{2}} \quad (4.2.2)$$

while  $\eta_{\text{rare}} > \eta_{C_L}$ , as shown as the black line in Figure 4.2.1(b). When  $\eta_{\text{rare}} = \eta_{C_L}$  for  $J = L$  in (3.2.3), the chord between  $\eta_L$  and  $\eta_{\text{rare}}$  is horizontal and can be found on either flux curve in Figure 4.2.1(a). The green star in Figure 4.2.1(b) is the stationary shock point  $(\xi_S, \tau_S)$  found by solving for  $\tau$  in (4.2.1) and substituting into (4.2.2) to find  $\xi = \xi_S$ .

As the rarefaction continues to erode away on the right side of the shock, the result is a forward shock, given by

$$\frac{d\xi}{d\tau} = 1 - \eta_{\text{rare}} - \eta_L, \quad (4.2.3)$$

between  $\eta_L$  and the solutions within the rarefaction,  $\eta_{C_L} > \eta_{\text{rare}} > \eta^*$  given by (4.2.1). The

forward shock emanates from  $(\xi_S, \tau_S)$ , and the position is given by

$$\xi = \xi_2 + (1 - 2\eta_L)\tau + \left[ (\xi_S - \xi_2)\tau_S^{-\frac{1}{2}} - (1 - 2\eta_L)\tau_S^{\frac{1}{2}} \right] \tau^{\frac{1}{2}},$$

which is the red line in Figure 4.2.1. When  $\eta_{\text{rare}} = \eta^*$ , the characteristic speed can be found from the horizontal tangent on either flux curve in Figure 4.2.1(a). Here,  $\xi = \xi^* = \xi_2$  and  $\tau = \tau^* = \tau_S \left( \frac{\eta_{CL} - \eta_L}{\eta^* - \eta_L} \right)^2$ , indicated by the black star in Figure 4.2.1(b). As a forward shock from  $\eta_L$  to  $\eta_{\text{rare}}$  progresses,  $\sigma = 1 - \varepsilon$  through the rarefaction. Hence, at a given  $(\xi, \tau)$  within the portion the rarefaction from  $\eta^*$  to  $\eta_R$ , the solution is

$$\eta_{\text{rare}} = \frac{1}{2} \left[ 1 - \frac{\xi - \xi_2}{\sigma \tau} \right], \quad (4.2.4)$$

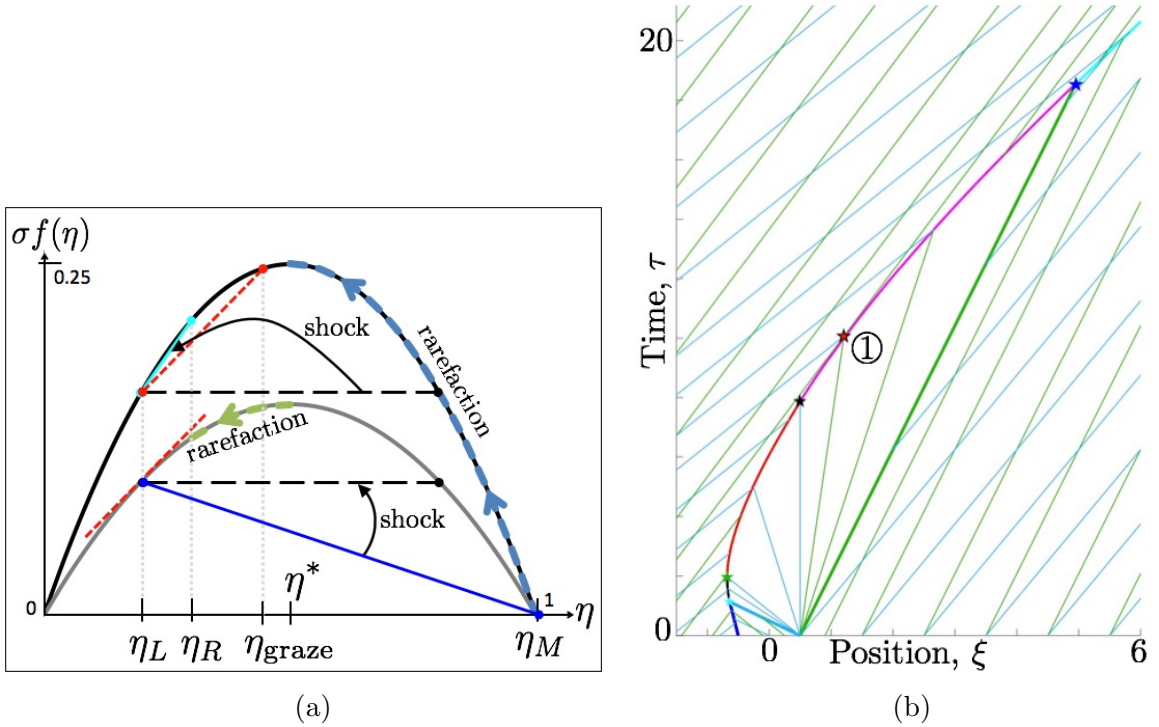


Figure 4.2.1: For shock-rarefaction interaction with  $\eta_L = 0.2$ ,  $\eta_M = 1$ ,  $\eta_R = 0.3$ ,  $\varepsilon = 0.4$ , (a) characteristic and shock speeds determined from discontinuous flux curves, and (b) solution in characteristic plane. Dashed red lines in (a) correspond to point ① in (b) where shock speed equals slower characteristic speed on left.

which, when combined with (4.2.3) yields the shock position in this region,

$$\xi = \xi_2 + \left( \frac{\sigma}{2\sigma - 1} \right) (1 - 2\eta_L) \tau + \left[ \left( \xi^* - \xi_2 \right) \tau^{*- \frac{1}{2\sigma}} - \left( \frac{\sigma}{2\sigma - 1} \right) (1 - 2\eta_L) \tau^{* \frac{2\sigma - 1}{2\sigma}} \right] \tau^{\frac{1}{2\sigma}}, \quad (4.2.5)$$

shown in pink in Figure 4.2.1(b). Table 4.2 summarizes the three possible analytic solutions for exact shock position derived above and an additional possible backward shock obtained when  $\eta_{\text{rare}}$  in (4.2.4) when mobility  $\mathcal{M} = 1$ . For this example, a forward shock persists until it reaches the leading edge of the rarefaction, given by a bold green line in Figure 4.2.1(b). Since  $\eta_R < \eta^*$ , the leading characteristic is given by  $\xi = \xi_2 + \sigma (1 - 2\eta_R) \tau$ , which can be combined with (4.2.5) to yield the finite interaction position,  $\xi_F$ , and time,  $\tau_F$ , the dark blue star in Figure 4.2.1(b).

After the final point  $(\xi_F, \tau_F)$ , there are only two outgoing constant states separated by a shock with strength  $\eta_R - \eta_L$ , shown as a cyan line in Figure 4.2.1. We have shown that if  $\eta_L < \eta_R$ , the result of the interaction is a single shock with strength  $\eta_R - \eta_L$ ; the total number of waves decreases from two to one, and the total variation decreases from  $2\eta_M - \eta_L - \eta_R$  to  $\eta_R - \eta_L$ . If  $\eta_L = \eta_R$ , the result of the interaction is a plume of constant height  $\eta_L = \eta_R$ ; the total variation decreases from  $2(\eta_M - \eta_L)$  to 0, and the number of waves decreases from two to zero. If  $\eta_L > \eta_R$ , then the long-time behavior is a rarefaction wave from  $\eta_L$  down to  $\eta_R$ , the remnants of the short-time wave joining  $\eta_M$  to  $\eta_R$ , after the interaction with the shock wave has completed.

The catalog of interactions shows that for Case A, which initially contained a shock and rarefaction, the total variation always decreases and the middle state  $\eta_M$  is always eliminated from the solution in finite time.

#### 4.2.2 Case A: Summary & Cross-hatch Characteristics

In Figure 4.2.1, we illustrate the solution as the interaction between shock and rarefaction proceeds for the specific flux (2.4.3) with  $\mathcal{M} = 1$  and other constant values shown in the figure. On the left, we show the track of the rarefaction through the flux curves as the characteristics fan from negative to positive speed. The rarefaction fan provides the values of  $\eta$  on the right of the shock as the evolution proceeds. The shock speed is represented by the slope of the chords in Figure 4.2.1(a). As the speed switches from negative to positive, the chord moves from the lower flux graph to the upper, as  $\eta_\tau$  changes sign. The crossover is represented by the horizontal dashed line. In this Case A example, the construction proceeds until the rarefaction wave has been completely absorbed by the shock.

Table 4.2: Shock position  $\xi = \hat{\xi} + \alpha (1 - 2\hat{\eta}) \tau + \left[ (\xi_e - \hat{\xi}) \tau_e^{-\beta_1} - \alpha (1 - 2\hat{\eta}) \tau_e^{\beta_2} \right] \tau^{\beta_1}$  for a shock emanating from  $(\xi_e, \tau_e)$  that is the result of a rarefaction emanating from  $\hat{\xi}$  interacting with a constant state  $\hat{\eta}$ , for  $\mathcal{M} = 1$  and  $\sigma = 1 - \varepsilon$ . The colored circles correspond to shock colors in Figures 4.2.1 and 4.4.3.

$\eta_{\text{rare}} \backslash d\xi/d\tau$	$1 - \eta_{\text{rare}} - \hat{\eta}$	$\sigma (1 - \eta_{\text{rare}} - \hat{\eta})$
$\frac{1}{2} \left[ 1 - \frac{\xi - \hat{\xi}}{\tau} \right]$	$\alpha = 1$ $\beta_1 = \frac{1}{2}$ $\beta_2 = \frac{1}{2}$ ●	$\alpha = \frac{\sigma}{2-\sigma}$ $\beta_1 = \frac{\sigma}{2}$ $\beta_2 = \frac{2-\sigma}{2}$ ●
$\frac{1}{2} \left[ 1 - \frac{\xi - \hat{\xi}}{\sigma \tau} \right]$	$\alpha = \frac{\sigma}{2\sigma-1}$ $\beta_1 = \frac{1}{2\sigma}$ $\beta_2 = \frac{2\sigma-1}{2\sigma}$ ●	$\alpha = \sigma$ $\beta_1 = \frac{1}{2}$ $\beta_2 = \frac{1}{2}$ ●

This interaction of a shock with a rarefaction looks similar to such interactions for a scalar conservation law with convex flux [29, 37]. However, there is a small but significant difference. While the shock has negative speed, it is calculated from the flux  $(1 - \varepsilon) f(\eta)$ . The shock is admissible because the characteristics on the left have positive speed, and the faster characteristics on the right have speed  $(1 - \varepsilon) f'(\eta)$ , which is slower than the shock speed, as shown in Figure 4.2.1(b). In fact, for the smaller flux (in the lower graph), the shock satisfies the Lax entropy condition. However, as the shock turns and gains positive speed, we switch to the upper flux curve. The characteristics on the right both have negative speed to start with, and hence impinge on the shock. On the left, both characteristics travel faster than the shock. In fact, as the shock turns, it has zero speed, and the characteristics for both fluxes have positive speed, so this property persists for some further time.

However, as the shock continues to accelerate, there is a time, ① in Figure 4.2.1(b), when the shock moves with the characteristic speed of  $(1 - \varepsilon) f'(\eta_L)$  of the smaller flux, see red dashed lines in Figure 4.2.1(a) corresponding to  $\eta = \eta_{\text{graze}}$ . Consequently, if we continue to look only at the single family of characteristics that were significant for the shock when it had negative speed, then the shock fails to satisfy the Lax entropy condition after this time. Since the rarefaction to the right of this shock can only increase the shock speed, the slower characteristics on the left will no longer enter the resulting shock; hence, cross-hatch characteristics are a necessary and interesting construction because we have to include the characteristics of the larger flux

(which had already been invoked to calculate the shock speed) in order to make sense of the subsequent progress of the shock wave. In Figure 4.2.1(b), you can see quite clearly that a characteristic grazes the shock at point ①, but it is the slower (green) characteristic - the faster (blue) characteristics on the left continue to impinge on the shock. This example and other similar instances are the reason for including both families of characteristics (*cross-hatch characteristics*) in open regions of the  $(\xi, \tau)$  plane where  $\eta$  is constant.

Figure 4.2.1(b) also demonstrates the result of Lemma 4.2.2. Consider the resulting shock emanating from  $\tau_F$ . The characteristics determined by both the upper and lower flux curves for  $\eta_R$  enter the shock, as do the faster characteristics on the left, shown in blue. The slower characteristics on the left are determined by the lower flux curve since  $\eta_L < \eta^*$ ; these characteristics from the slower family exit the shock.

### 4.2.3 Case $\mathcal{A}$ : Shock - Expansion Shock: $\eta_L < \eta_M$ and $\eta_R < \eta_M$

For the wave-front tracking method, rarefactions are approximated by one or more expansion shocks. In Case A, a shock on the left will always interact with a rarefaction on the right; however, when the rarefaction is replaced by a piecewise constant approximation, the shock from  $\eta_L$  up to  $\eta_M$  and slowest (left-most) expansion shock between  $\eta_M$  and  $\eta_{\text{exp}_M} \in [\eta_R, \eta_M)$  do not always interact. Let  $\Lambda_{LM} = \frac{f(\eta_M) - f(\eta_L)}{\eta_M - \eta_L}$ :

(i) If  $\Lambda_{LM} > 0$ , a forward shock with speed  $\Lambda_{LM}$  connects  $\eta_L$  and  $\eta_M$ . If  $\eta_M \leq \eta^*$ , the expansion shock between  $\eta_M$  and  $\eta_{\text{exp}_M}$  also has positive speed; however, if  $\eta_M > \eta^*$ , the expansion shock could have positive, zero, or negative speed. The shock and expansion shock will only interact if the shock moves faster than the expansion shock. Let  $\tilde{\eta}_M < \eta_M$  be such that

$$\begin{cases} \tilde{\eta}_M = 0, & \text{if } (1 - \varepsilon) \frac{f(\eta_M) - f(0)}{\eta_M} < \Lambda_{LM}, \\ (1 - \varepsilon) \frac{f(\eta_M) - f(\tilde{\eta}_M)}{\eta_M - \tilde{\eta}_M} = \Lambda_{LM}, & \text{otherwise.} \end{cases}$$

Hence, the shock and approximating expansion shock(s) do not approach if  $\eta_L < \eta_M$  with  $\Lambda_{LM} > 0$  and  $\eta_{\text{exp}_M}$  satisfies

$$\eta_R \leq \eta_{\text{exp}_M} \leq \tilde{\eta}_M < \eta_M. \quad (4.2.6)$$



(ii) For the case when  $\Lambda_{LM} \leq 0$ , the shock speed,  $(1 - \varepsilon) \Lambda_{LM}$ , is reduced due to residual trapping. Define  $\bar{\eta}_M < \eta_M$  to be such that

$$(1 - \varepsilon) \Lambda_{LM} = \frac{f(\eta_M) - f(\bar{\eta}_M)}{\eta_M - \bar{\eta}_M}.$$

The shock wave and expansion shock wave do not interact if  $\eta_L < \eta_M$  has  $\Lambda_{LM} \leq 0$  and  $\eta_{\text{exp}_M}$  is such that

$$\eta_R \leq \eta_{\text{exp}_M} \leq \bar{\eta}_M < \eta_M \quad (4.2.7)$$

because the speed of the expansion shock approximating the rarefaction from  $\eta_M$  to  $\eta_R$  exceeds or equals the speed of the shock from  $\eta_L$  to  $\eta_M$ . Hence, if we have an expansion shock from  $\eta_M$  down to  $\eta_{\text{exp}_M}$ , where  $\eta_{\text{exp}_M}$  does not satisfy (4.2.6) or (4.2.7), then the shock and approximating expansion shock interact to yield interactions analogous to continuous shock-rarefaction interactions in Case A.

### 4.3 Case B: Shock - Shock: $\eta_L < \eta_M < \eta_R$

The second case involves a shock from a left state up to a middle state followed by a shock from the middle state up to a right state. Since the flux function is concave, the shock from  $\eta_L$  to  $\eta_M$  will have a greater shock speed than the shock from  $\eta_M$  to  $\eta_R$ , so the shocks will approach each other and interact at a finite time to yield a simple shock from  $\eta_L$  up to  $\eta_R$  with strength  $\eta_R - \eta_L$ . If the speeds of the approaching shocks have the same sign, the resulting shock has the same direction; if not, the resulting shock is forward if  $f(\eta_L) < f(\eta_R)$  as in Figure 4.3.1(b), stationary if  $f(\eta_L) = f(\eta_R)$ , or backward if  $f(\eta_L) > f(\eta_R)$ . The total variation is unchanged before and after the discontinuities interact, and the middle state is eliminated in finite time for Case B.

### 4.4 Case C: Rarefaction - Shock: $\eta_M < \eta_L$ and $\eta_M < \eta_R$

This case mirrors Case A, in that the short-time solution is a rarefaction wave to the left of a shock wave. However, whereas in Case A the two waves approach, in Case C their approach depends on further restrictions on the data. The reason for this is that the slower characteristics on the left can leave the shock (Lemma 3.2.2); they are necessarily parallel to the leading edge of the rarefaction. We distinguish two subcases in which the waves do not approach:

(i) If  $\eta_M \leq \eta^*$ , define  $\tilde{\eta}_M$  by

$$\frac{f(\tilde{\eta}_M) - f(\eta_M)}{\tilde{\eta}_M - \eta_M} = (1 - \varepsilon) f'(\eta_M),$$

and let  $\lambda_M$  denote this speed, shown in Figure 4.4.1. Then  $\lambda_M > 0$  is the speed of the leading edge of the rarefaction, and if  $\eta_R = \tilde{\eta}_M$ , then it is also the speed of the shock, since the shock has a jump up and positive speed. Then for  $\eta_M \leq \eta^*$  and

$$\eta_M < \eta_R \leq \tilde{\eta}_M, \quad \eta_M < \eta_L, \quad (4.4.1)$$

the shock from  $\eta_M$  to  $\eta_R$  has positive and larger speed:

$$\frac{f(\eta_R) - f(\eta_M)}{\eta_R - \eta_M} \geq \lambda_M.$$

Thus, (4.4.1) is sufficient to guarantee that the shock and rarefaction do not approach.

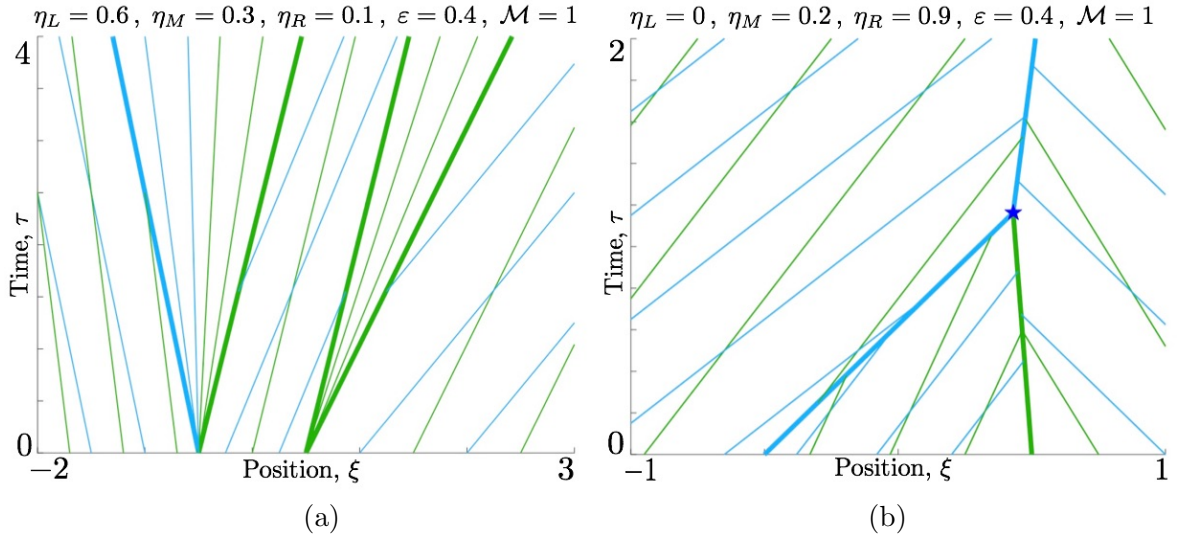


Figure 4.3.1: (a) Pair 8b has fanning rarefactions separated by a fixed distance for all time. (b) Case B example (Pair 7e) has two shocks colliding.

(ii) Similarly, if  $\eta_M > \eta^*$ , then the shock speed and speed of the leading edge of the rarefaction wave are both negative. In this case, the rarefaction is backward and uses the larger flux  $f(\eta)$  whereas the shock uses the lower flux  $(1 - \varepsilon)f(\eta)$ . Consequently, the interaction condition becomes

$$(1 - \varepsilon) \frac{f(\eta_R) - f(\eta_M)}{\eta_R - \eta_M} > f'(\eta_M).$$

Define  $\bar{\eta}_M > \eta_M$  by

$$\begin{cases} \bar{\eta}_M = 1, & \text{if } (1 - \varepsilon) \frac{f(1) - f(\eta_M)}{1 - \eta_M} > f'(\eta_M), \\ (1 - \varepsilon) \frac{f(\bar{\eta}_M) - f(\eta_M)}{\bar{\eta}_M - \eta_M} = f'(\eta_M), & \text{otherwise.} \end{cases}$$

Then the two waves do not approach if  $\eta^* < \eta_M$  and

$$\eta_M < \eta_R \leq \bar{\eta}_M, \quad \eta_M < \eta_L. \quad (4.4.2)$$

In summary, if neither (4.4.1) nor (4.4.2) are satisfied by  $\eta_R$ , then the rarefaction wave and shock wave interact much as in Case A. Otherwise, the shock travels faster than the rarefaction, and there is no interaction.

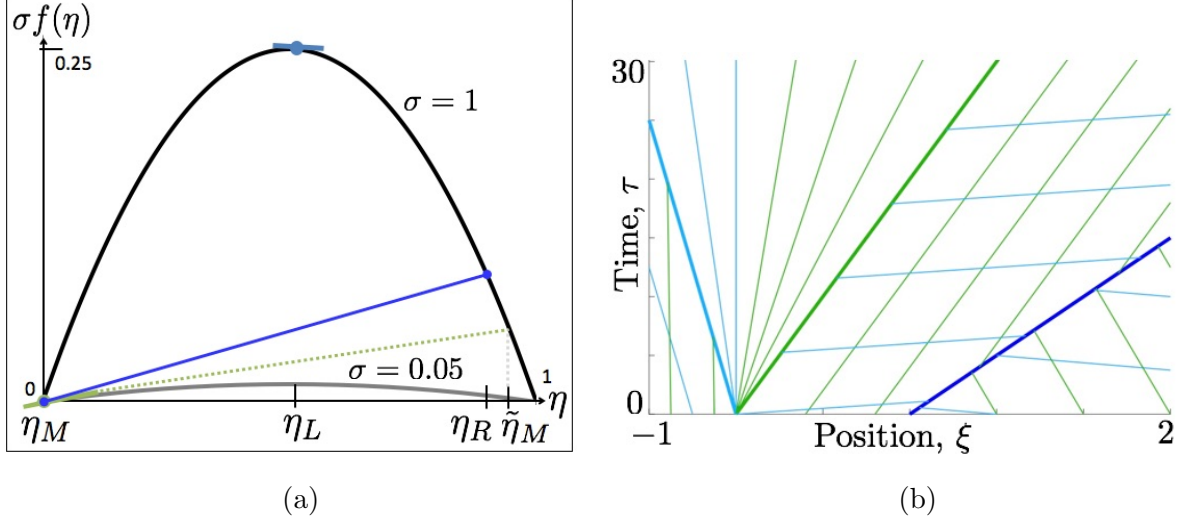


Figure 4.4.1: No interaction when speed of leading characteristic in rarefaction is less than shock speed represented on (a) discontinuous flux curves and (b) characteristic plane with  $\eta_L = 0.51$ ,  $\eta_M = 0$ ,  $\eta_R = 0.9$ ,  $\sigma = 0.05$ , and  $\tilde{\eta}_M \approx 0.95$ .

#### 4.4.1 Case C: Example

We derive a representative Case C (Pair 6e) analytic solution when  $\mathcal{M} = 1$  which has a rarefaction from  $\eta_L$  down to  $\eta_M$  emanating from  $\xi = \xi_1$  and a forward shock from  $\eta_M$  up to  $\eta_R$  centered at  $\xi_2 > \xi_1$ . The initial total variation for this case is  $\eta_L + \eta_R - 2\eta_M$ . The leading characteristic of the rarefaction interacts with the forward shock at  $(\xi_T, \tau_T)$ , point (a) in Figures 4.4.2 and 4.4.3. Subsequently, the rarefaction solution is given by (4.2.4) and the forward shock by (4.2.3); hence, the resulting shock position, shown in pink in Figure 4.4.3, is given by Table 4.2 with  $\xi_e = \xi_T$ ,  $\tau_e = \tau_T$ ,  $\hat{\xi} = \xi_1$ , and  $\hat{\eta} = \eta_R$ , until the shock becomes stationary at  $(\xi_S, \tau_S)$ , point (b) in Figures 4.4.2 and 4.4.3. Then the speeds of the shock and the characteristics in the rarefaction are reduced by  $\sigma = 1 - \varepsilon$ , and a backward shock position is obtained from the orange entry in Table 4.2 with  $\xi_e = \xi_S$ ,  $\tau_e = \tau_S$ ,  $\hat{\xi} = \xi_1$ , and  $\hat{\eta} = \eta_R$  and is drawn in orange in Figure 4.4.3. This shock path continues until  $\eta_{\text{rare}} = \eta^*$  at  $(\xi^*, \tau^*)$ , point (c) in Figures 4.4.2 and 4.4.3, at which point  $\eta_{\text{rare}}$  is given by (4.2.1), and the backward shock position, shown in black in Figure 4.4.3, is determined by Table 4.2 until  $\eta_{\text{rare}} = \eta_L$ , if possible.

Unlike Cases A and B, not all initial conditions in Case C lead to an eliminated initial middle state in finite time. Some solutions in Case C exhibit unusual behavior due to the flux discontinuity that does not arise in scalar equations with a single flux: shock speeds determined by one flux curve can equal corresponding characteristic speeds found on the other flux curve. In Figure 4.4.2(e), the plume asymptotically approaches a height of  $\tilde{\eta} \in (\max(\eta^*, \eta_M), \min(\eta_L, \eta_R))$  such that

$$f'(\tilde{\eta}) = (1 - \varepsilon) \frac{f(\eta_R) - f(\tilde{\eta})}{\eta_R - \tilde{\eta}}.$$

Hence, if  $\eta_L \geq \tilde{\eta}$ , the backward shock does not reach the rarefaction's trailing characteristic; the shock speed approaches the characteristic speed corresponding to  $\tilde{\eta}$  shown in purple in Figure 4.4.3(g). The result approaches a rarefaction from  $\eta_L$  down to  $\tilde{\eta}$  and a shock from  $\tilde{\eta}$  up to  $\eta_R$ ; since  $\eta_M < \tilde{\eta}$ , the total variation of the solution decreases to  $\eta_L + \eta_R - 2\tilde{\eta}$ . However, if  $\eta_L < \tilde{\eta}$  as in Figure 4.4.3(f), the middle state is eliminated in finite time, resulting in a decrease of total variation to  $\eta_R - \eta_L$ .

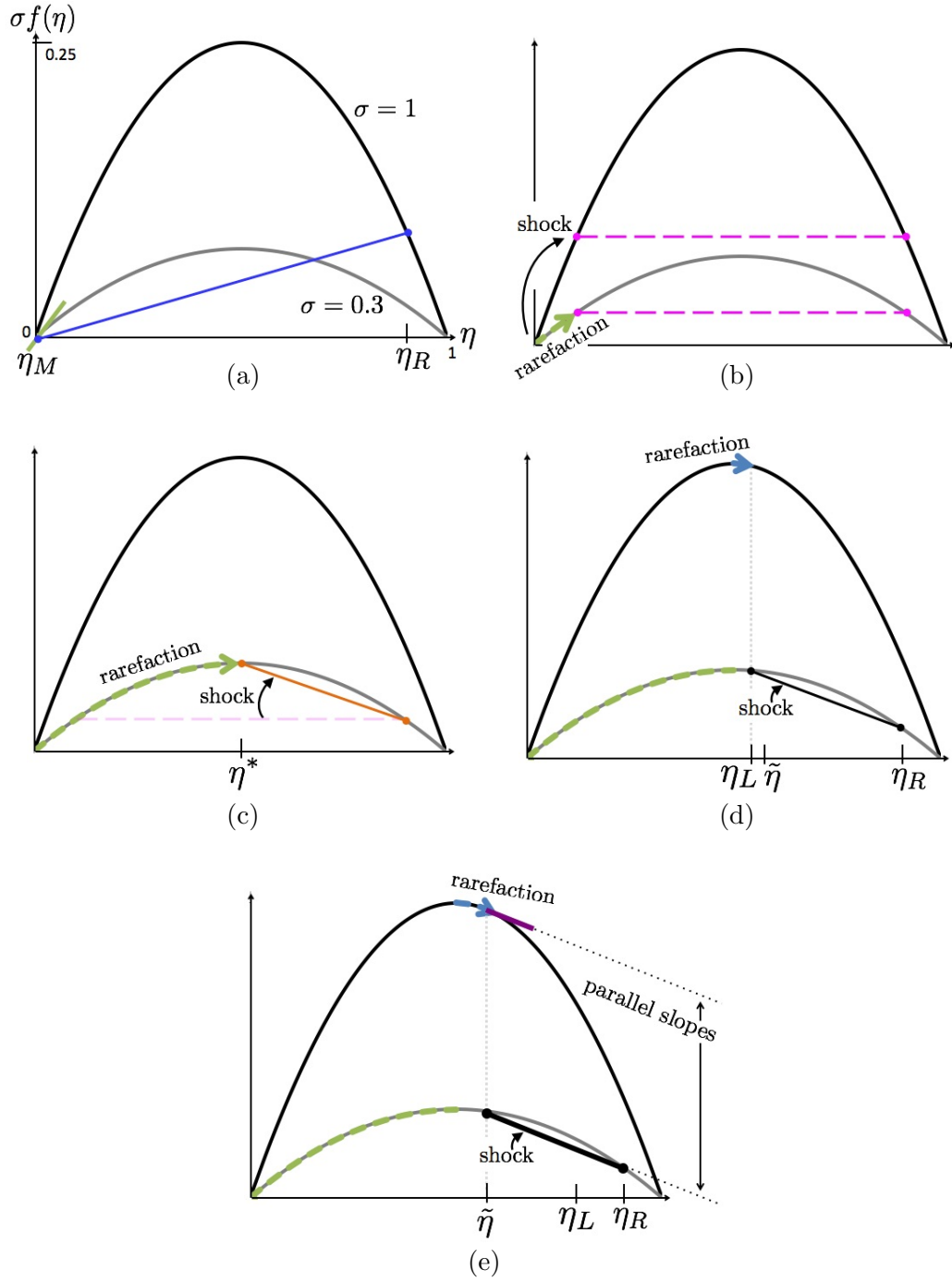


Figure 4.4.2: Shock speeds and characteristic speeds determined by discontinuous flux curves for  $\eta_M = 0$ ,  $\eta_R = 0.9$ ,  $\varepsilon = 0.7$ ,  $\mathcal{M} = 1$ . Points (a)-(e) correspond to points on Figure 4.4.3.

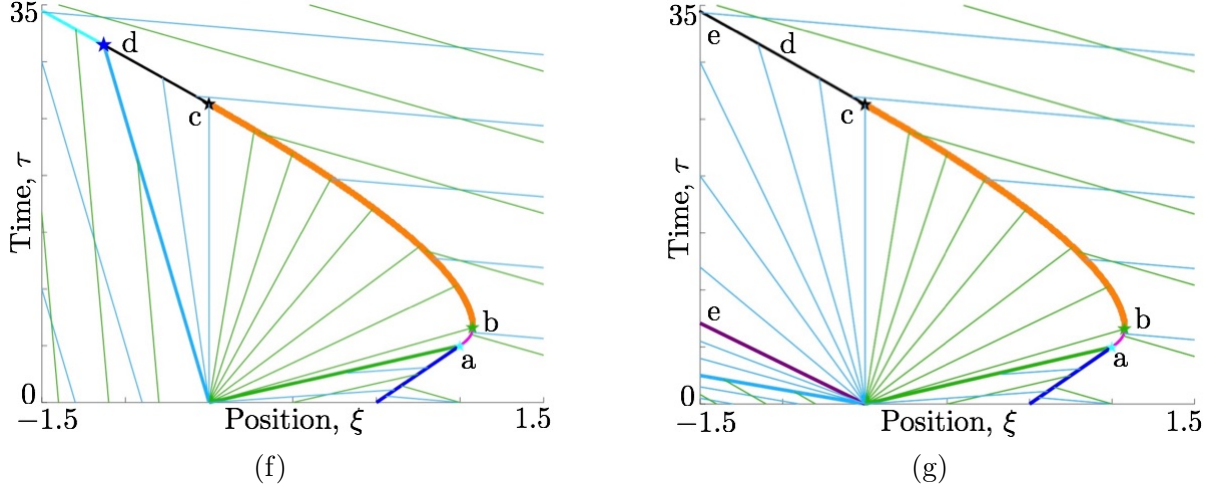


Figure 4.4.3: Analytic solution for  $\eta_M = 0$ ,  $\eta_R = 0.9$ ,  $\varepsilon = 0.7$ ,  $\mathcal{M} = 1$  with (f)  $\eta_L = 0.51 < \tilde{\eta}$ , and (g)  $\eta_L = 0.7 > \tilde{\eta}$ . Points (a)-(e) correspond to Figures 4.4.2(a)-(e).

It is also possible for a middle state to asymptote to a value  $\bar{\eta} \in (\eta_M, \min(\eta^*, \eta_L, \eta_R))$  such that

$$(1 - \varepsilon) f'(\bar{\eta}) = \frac{f(\eta_R) - f(\bar{\eta})}{\eta_R - \bar{\eta}}$$

since the speed of a forward shock is determined by the upper flux curve, and the characteristic speed to the right of the center of a rarefaction is found on the lower flux curve. Again, the total variation of the solution decreases. Hence, for Case C, if there is an interaction, the total variation always decreases, and the number of outgoing waves is non-increasing.

#### 4.4.2 Case $\mathcal{C}$ : Expansion Shock - Shock: $\eta_M < \eta_L$ and $\eta_M < \eta_R$

When the rarefaction in Case C is approximated with one (or more) expansion shock(s), the fastest (right-most) expansion shock connects  $\eta_{\text{exp}_M} \in (\eta_M, \eta_L]$  down to  $\eta_M$  with speed

$$\Lambda_{eM} = \frac{f(\eta_{\text{exp}_M}) - f(\eta_M)}{\eta_{\text{exp}_M} - \eta_M}.$$

In Case C, we necessitated restrictions on the incoming waves to obtain an interaction. Likewise, we have two conditions where the expansion shock and shock diverge:

(i) If  $\Lambda_{eM} \geq 0$ , the expansion shock speed is found on the lower flux curve. Define  $\tilde{\eta}_M > \eta_M$  by

$$(1 - \varepsilon) \Lambda_{eM} = \frac{f(\tilde{\eta}_M) - f(\eta_M)}{\tilde{\eta}_M - \eta_M}.$$

The expansion shock from  $\eta_{\text{exp}_M}$  to  $\eta_M$  and the shock from  $\eta_M$  to  $\eta_R$  do not approach if  $\eta_M < \eta_{\text{exp}_M} \leq \eta_L$  with  $\Lambda_{eM} \geq 0$ , and  $\eta_R$  satisfies

$$\eta_M < \eta_R \leq \tilde{\eta}_M. \quad (4.4.3)$$

(ii) If  $\Lambda_{eM} < 0$ , let  $\bar{\eta}_M > \eta_M$  be such that

$$\begin{cases} \bar{\eta}_M = 1, & \text{if } (1 - \varepsilon) \frac{f(1) - f(\eta_M)}{1 - \eta_M} > \Lambda_{eM}, \\ (1 - \varepsilon) \frac{f(\bar{\eta}_M) - f(\eta_M)}{\bar{\eta}_M - \eta_M} = \Lambda_{eM}, & \text{otherwise.} \end{cases}$$

The approximating expansion shock on the left and the shock to the right do not approach if  $\eta_M < \eta_{\text{exp}_M} \leq \eta_L$  with  $\Lambda_{eM} < 0$  with a given  $\eta_R$  such that

$$\eta_M < \eta_R \leq \bar{\eta}_M. \quad (4.4.4)$$

Hence, an expansion shock wave and shock wave will move apart if the shock speed is greater than the expansion shock speed. Contrastingly, if  $\eta_R$  does not satisfy (4.4.3) or (4.4.4), then the expansion shock wave and shock wave approach and interact as in previous cases.

## 4.5 Non-increasing Total Variation & Number of Waves

If (4.2.6)-(4.4.4) are not satisfied, then the two incoming waves interact. Given an initial rarefaction, if the result of an interaction is a rarefaction, the resulting rarefaction is smaller than the initial rarefaction. When the initial rarefaction is approximated by one or more expansion shocks, as in Case  $\mathcal{A}$  and Case  $\mathcal{C}$ , we ensure that the size of each expansion shock is below a threshold value; since the interaction can only decrease the size of a rarefaction, the corresponding number of approximating expansion shocks will not increase. All possible results for two approaching waves between three incoming constant states are summarized in Table 4.3: total variation and number of waves cannot increase due to an interaction.

Table 4.3: Wave interaction summary.

Case	Initial Waves	Total Variation	Number of Waves
A	$\eta_L < \eta_M, \eta_R < \eta_M$	decreases	decreases
$\mathcal{A}$	$\eta_L < \eta_M, \eta_{\text{exp}_M} < \eta_M$	decreases	decreases
B	$\eta_L < \eta_M < \eta_R$	constant	decreases
C	$\eta_M < \eta_L, \eta_M < \eta_R$	decreases	decreases (if $\eta_L < \bar{\eta} < \tilde{\eta}$ ) constant (otherwise)
$\mathcal{C}$	$\eta_M < \eta_{\text{exp}_M}, \eta_M < \eta_R$	decreases	decreases



---

Existence Theorem

---

Plume migration within a porous aquifer depends on the geometry of the carbon dioxide plume at the end of injection [19, 21]. An analytic solution for a specific idealized CO<sub>2</sub> plume is constructed by Hesse, Orr, and Tchelepi [17]. We consider the scalar conservation law (2.4.2) and an arbitrary initial plume of supercritical carbon dioxide,

$$\begin{cases} \eta_\tau + (\sigma f(\eta))_\xi = 0, & \xi \in \mathbb{R}, \tau > 0, \\ \eta(\xi, 0) = \eta_0(\xi), & \xi \in \mathbb{R}, \end{cases} \quad (5.0.1)$$

in which  $\eta_0 \in L^1(\mathbb{R}) \cap BV(\mathbb{R})$  with  $0 \leq \eta_0 \leq 1$ . In this chapter, we describe the wave-front tracking method, following the approach of LeFloch [26], and then prove the following result:

**Theorem 5.0.1.** *For  $\eta_0 \in L^1(\mathbb{R}) \cap BV(\mathbb{R})$  with  $0 \leq \eta_0 \leq 1$ , the Cauchy problem (5.0.1) has a classical entropy solution  $\eta(\xi, \tau) \in L^1_{loc}$ , satisfying*

- (a)  $\inf(\eta_0) \leq \eta(\xi, \tau) \leq \sup(\eta_0), \quad \xi \in \mathbb{R}, \tau > 0,$
- (b)  $TV(\eta(\xi, \tau)) \leq TV(\eta_0), \quad \xi \in \mathbb{R}, \tau \geq 0,$
- (c)  $\left\| \eta(\xi, \tau_2) - \eta(\xi, \tau_1) \right\|_{L^1(\mathbb{R})} \leq TV(\eta_0) \sup |f'| |\tau_2 - \tau_1|, \quad \xi \in \mathbb{R}, \tau_1, \tau_2 \geq 0,$

*including convergence to the initial condition:  $\left\| \eta(\xi, \tau) - \eta_0 \right\|_{L^1(\mathbb{R})} \leq TV(\eta_0) \sup |f'| \tau$  for all  $\tau \geq 0$ .*

## 5.1 Wave-front Tracking

Dafermos [10] introduced wave-front tracking as a method to construct approximate solutions for scalar, nonlinear, hyperbolic partial differential equations. The method has since been greatly generalized to systems of hyperbolic conservation laws [3, 4]. Much can be learned about the structure of the solution of a Cauchy problem from this superposition of solutions to Riemann problems [9, 11, 13, 27].

Since a sharp interface between the invading CO<sub>2</sub> and ambient brine was assumed, the shape of the invading plume is well-defined and acts as an initial guide for construction of wave interactions. At any position  $\xi$  in the aquifer,  $\eta_0 = 0$  indicates all brine, and  $\eta_0 = 1$  corresponds to all CO<sub>2</sub>; therefore,  $0 \leq \inf(\eta_0) \leq \sup(\eta_0) \leq 1$ . In the wave-front tracking algorithm, we first approximate the initial plume shape,  $\eta_0(\xi)$ , with a sequence of piecewise constant functions,  $\eta_0^h(\xi)$ , with  $h > 0$ , such that

$$\begin{aligned} \inf(\eta_0) &\leq \eta_0^h \leq \sup(\eta_0) \\ TV(\eta_0^h) &\leq TV(\eta_0) \\ \eta_0^h &\rightarrow \eta_0 \text{ in the } L^1 \text{ norm as } h \rightarrow 0^+. \end{aligned} \tag{5.1.1}$$

Each approximation  $\eta_0^h$  is constructed to have a finite number of discontinuities of magnitude at most  $h$ . The construction of a piecewise constant solution for short time involves solving the Riemann problems associated with each discontinuity in  $\eta_0^h$ ; the solutions to the resulting Riemann problems are known from Chapter 3. Rarefaction waves are replaced by expansion shocks of the same magnitude. The classical and expansion shock waves constructed from the initial discontinuities yield a piecewise constant approximation of the solution that persists until two wave-fronts approach. When waves meet, we refer to the collision as an interaction, and the solution is obtained as in Chapter 4. If the resulting solution is an admissible shock, the resulting jump up between constant states may exceed the initial threshold  $h$ ; large admissible shocks do not pose any complications as we move forward in the proof, so the shock is propagated forward without change. If the resulting solution is a rarefaction wave, then (as observed in the previous chapter) *the magnitude is necessarily smaller than  $h$* ; the rarefaction wave is approximated by an expansion shock with magnitude less than  $h$ , traveling with the shock speed of that discontinuity. The resulting discontinuities travel with constant shock speeds until the next interaction time, where the solution process repeats as in Chapter 4. Continuing in this way, we generate a piecewise constant solution of the conservation law for each approximation of the given plume. We have thus constructed  $\eta^h(\xi, \tau)$ , a sequence of wave-front tracking approximate solutions generated by the sequence of initial data  $\eta_0^h(\xi)$ .

## 5.2 Proof: Existence of a Weak Solution of (5.0.1)

In this section, we show that the Cauchy problem (5.0.1) admits a weak solution that satisfies conditions of Theorem 5.0.1. The proof is similar to the general proof outlined in Lefloch [26]; however, the discontinuous flux is carefully considered for this problem. We prove the existence of a limit function of the wave-front tracking approximations and show that the limit function is a weak solution of (5.0.1).

### 5.2.1 Existence of a Limit Function

In Chapter 4, we showed that the number of waves and total variation decreased or remained constant at any interaction time and remained constant between interaction times. Consequently, the number of wave interactions and resulting wave-fronts in each  $\eta^h$  remains finite for all  $\tau > 0$ , so the approximations are globally well-defined and prolong for all time [4]. Though LeFloch [26] considers the possibility of an accumulation of interaction points, the issue is easily resolved for (5.0.1): the initial number of discontinuities is finite, and the number of waves cannot increase as a result of any interaction, so there are finitely many interactions and, hence, no accumulation points.

Each approximation  $\eta^h$  is bounded by the corresponding  $\eta_0^h$ , as summarized by Figure 4.1.2 in the catalog of interactions. It follows from (5.1.1) that  $\inf(\eta_0) \leq \eta^h(\xi, \tau) \leq \sup(\eta_0)$  at any position and time; hence,  $\|\eta^h(\xi, \tau)\|_{L^\infty} \leq 1$ . As summarized in Table 4.3, total variation is non-increasing; therefore,  $TV(\eta^h(\xi, \tau)) \leq TV(\eta_0(\xi))$  for all  $\xi \in \mathbb{R}$  and  $\tau \geq 0$ .

Since the initial approximations were constructed with a finite number of waves, there will be finitely many, call that number  $\mathcal{K}$ , classical and expansion shocks in  $\eta^h$  within  $[\tau_1, \tau_2]$ , any time interval containing no interaction time. For  $m = 1, \dots, \mathcal{K}$ , let  $y_m'$  be the speed of propagating shock front  $\xi = y_m(\tau)$  in  $\eta^h$  for  $\tau \in [\tau_1, \tau_2]$ ; by (2.4.3),  $|y_m'| \leq \sup |f'| < \infty$ . The approximate solution to the left/right of wave-front  $y_m$  is  $\eta^h(y_m(\tau)^\mp, \tau)$ . In the  $(\xi, \eta)$  plane, the  $L^1$  norm is the area between the solutions at times  $\tau_1$  and  $\tau_2$ , as established in Figure 5.2.1. If, at a time  $\tau$ , a propagating front has a solution value to the left of it,  $\eta^h(y_m(\tau)^-, \tau)$ , which is larger than the  $\eta$  value to the right of the shock,  $\eta^h(y_m(\tau)^+, \tau)$ , then this is a positive addition to the  $L^1$  norm, as shown for all propagating fronts in Figure 5.2.1 except  $y_4$ . For  $y_4$ , the resulting area is subtracted from the other areas. The  $L^1$  norm is the absolute value of the result, as shown at the bottom of Figure 5.2.1. It follows that the approximate solutions  $\eta^h$  satisfy the uniform estimate given by

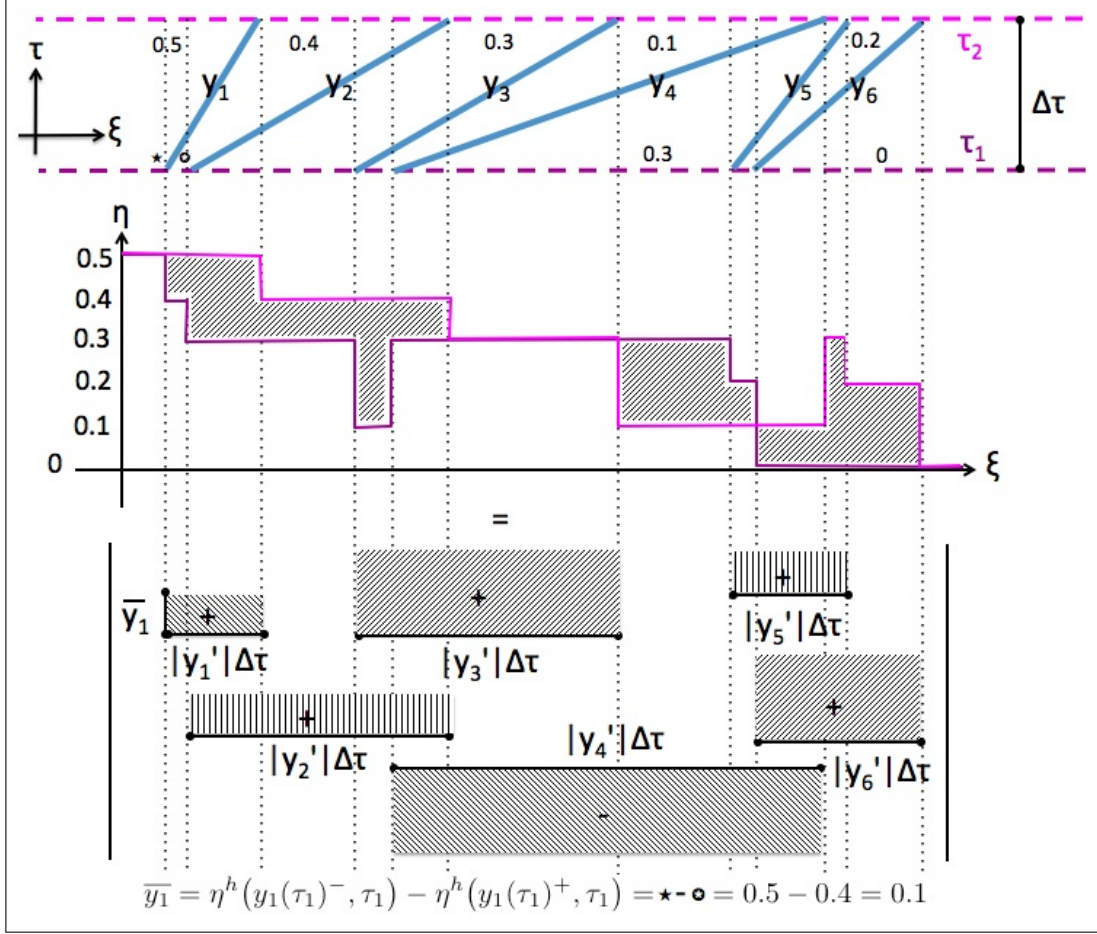


Figure 5.2.1: Geometric demonstration of the  $L^1$  norm.

$$\begin{aligned}
\left\| \eta^h(\xi, \tau_2) - \eta^h(\xi, \tau_1) \right\|_{L^1} &\leq \sum_{m=1}^{\mathcal{K}} \left| \eta^h(y_m(\tau_1)^-, \tau_1) - \eta^h(y_m(\tau_1)^+, \tau_1) \right| |y_m'| |\tau_2 - \tau_1| \\
&\leq TV(\eta_0) \sup |f'| |\tau_2 - \tau_1|,
\end{aligned} \tag{5.2.1}$$

since the sum of the vertical distances traveled along the  $\eta$ -axis is  $TV(\eta^h(\xi, \tau)) \leq TV(\eta_0)$  at time  $\tau \in [\tau_1, \tau_2]$ . Hence, we have shown that the sequence of functions  $\eta^h$  satisfies the conditions of both Helly's Compactness Theorem (Theorem A.1.1) and the Time-Dependent Helly's Theorem (Theorem A.2.1). Ergo, there exists a subsequence of  $\eta^h$ , call it  $\eta^{h,h}$ , and there

exists a function with bounded variation,  $\eta : \mathbb{R} \times \mathbb{R}^+ \rightarrow [0, 1]$ , such that

$$\begin{aligned} \eta^{h,h}(\xi, \tau) &\rightarrow \eta(\xi, \tau) \quad \text{in } L^1_{\text{loc}}, \\ \|\eta(\xi, \tau)\|_{L^\infty} + TV(\eta(\xi, \tau)) &\leq \kappa, \text{ and} \\ \|\eta(\xi, \tau_2) - \eta(\xi, \tau_1)\|_{L^1} &\leq \kappa |\tau_2 - \tau_1| \end{aligned} \tag{5.2.2}$$

for all  $\xi \in \mathbb{R}$ ,  $\tau, \tau_1, \tau_2 \in \mathbb{R}^+$ , and some  $\kappa > 0$ . We also have  $TV(\eta(\xi, \tau)) \leq \liminf_{h \rightarrow 0^+} TV(\eta^{h,h}(\xi, \tau))$  by Theorem A.1.1. Since  $\eta^{h,h}$  is a subsequence of  $\eta^h$ ,  $TV(\eta^{h,h}(\xi, \tau)) \leq TV(\eta_0(\xi))$ . Combination with the aforementioned lower semi-continuity property yields

$$TV(\eta(\xi, \tau)) \leq TV(\eta_0(\xi)) \quad \text{for all } \xi \in \mathbb{R} \text{ and } \tau \geq 0,$$

which is analogous to (b) in Theorem 5.0.1. Similarly, it follows that another property of the limit function is

$$\inf(\eta_0) \leq \eta(\xi, \tau) \leq \sup(\eta_0) \quad \text{for all } \xi \in \mathbb{R} \text{ and } \tau > 0,$$

paralleling (a) in Theorem 5.0.1. By (5.2.2),  $[\eta^{h,h}(\xi, \tau_2) - \eta^{h,h}(\xi, \tau_1)] \rightarrow [\eta(\xi, \tau_2) - \eta(\xi, \tau_1)]$  in  $L^1_{\text{loc}}$ ; hence  $\|\eta(\xi, \tau_2) - \eta(\xi, \tau_1)\|_{L^1} \leq \liminf_{h \rightarrow 0^+} \|\eta^{h,h}(\xi, \tau_2) - \eta^{h,h}(\xi, \tau_1)\|_{L^1}$  by the lower semi-continuity property of norms. Since  $\eta^{h,h}$  is a subsequence of  $\eta^h$ , combination of the previous inequality and the aforementioned uniform estimate yields a property akin to inequality (c) in Theorem 5.0.1:

$$\|\eta(\xi, \tau_2) - \eta(\xi, \tau_1)\|_{L^1} \leq TV(\eta_0) \sup |f'| |\tau_2 - \tau_1| \quad \text{for all } \xi \in \mathbb{R} \text{ and } \tau_1, \tau_2 \geq 0.$$

### 5.2.2 Limit Function is a Weak Solution

The wave-front tracking approximations  $\eta^h$  are exact solutions of  $\eta_\tau^h + (\sigma f(\eta^h))_\xi = 0$  because, by construction, the Rankine-Hugoniot jump condition (3.2.2) is satisfied across all admissible and expansion shocks. For  $0 \leq \eta \leq 1$ , it follows from (2.4.3) that  $|\sigma f'(\eta)| \leq |f'(0)| = 1$  since  $\mathcal{M} \geq 1$  for carbon sequestration. By (5.2.2), we have that  $\eta^{h,h} \rightarrow \eta$  in  $L^1_{\text{loc}}$ , which implies that  $\lim_{h \rightarrow 0^+} \iint \eta^{h,h} \varphi \, d\xi \, d\tau = \iint \eta \varphi \, d\xi \, d\tau$  for any test function  $\varphi \in C_0^1(\mathbb{R} \times \mathbb{R}^+)$  [47]. Hence,

$$\begin{aligned}
\left| \lim_{h \rightarrow 0^+} \int_{\mathbb{R}^+} \int_{\mathbb{R}} \varphi_\xi \left[ (\sigma f(\eta^{h,h})) - (\sigma f(\eta)) \right] d\xi d\tau \right| &\leq \lim_{h \rightarrow 0^+} \int_{\mathbb{R}^+} \int_{\mathbb{R}} |\varphi_\xi| \sup_{0 \leq \eta \leq 1} |\sigma f'| \left| \eta^{h,h} - \eta \right| d\xi d\tau \\
&\leq \lim_{h \rightarrow 0^+} \int_{\mathbb{R}^+} \int_{\mathbb{R}} |\varphi_\xi| \left| \eta^{h,h} - \eta \right| d\xi d\tau \\
&= 0.
\end{aligned}$$

Because  $\eta^{h,h}$  is a subsequence of  $\eta^h$ , it follows that  $\eta_\tau^{h,h} + (\sigma f(\eta^{h,h}))_\xi = 0$ , and

$$\begin{aligned}
0 &= - \lim_{h \rightarrow 0^+} \int_{\mathbb{R}^+} \int_{\mathbb{R}} \varphi \left[ \eta_\tau^{h,h} + (\sigma f(\eta^{h,h}))_\xi \right] d\xi d\tau \\
&= \lim_{h \rightarrow 0^+} \int_{\mathbb{R}^+} \int_{\mathbb{R}} \left[ \varphi_\tau \eta^{h,h} + \varphi_\xi (\sigma f(\eta^{h,h})) \right] d\xi d\tau + \lim_{h \rightarrow 0^+} \int_{\mathbb{R}} \varphi(\xi, 0) \eta^{h,h}(\xi, 0) d\xi \\
&= \int_{\mathbb{R}^+} \int_{\mathbb{R}} \left[ \varphi_\tau \eta + \varphi_\xi (\sigma f(\eta)) \right] d\xi d\tau + \int_{\mathbb{R}} \varphi(\xi, 0) \eta(\xi, 0) d\xi.
\end{aligned}$$

Therefore, the limit function  $\eta(\xi, \tau)$  from (5.2.2) is a weak solution of the conservation law (5.0.1) for all  $\xi \in \mathbb{R}$  and  $\tau > 0$ .

The inequality  $\|\eta(\xi, \tau) - \eta(\xi, 0)\|_{L^1} \leq \liminf_{h \rightarrow 0^+} \|\eta^{h,h}(\xi, \tau) - \eta^{h,h}(\xi, 0)\|_{L^1}$  follows from the lower semi-continuity property of the  $L^1$  norm [4, 26]. The uniform estimate derived in (5.2.1) yields  $\|\eta^{h,h}(\xi, \tau) - \eta^{h,h}(\xi, 0)\|_{L^1} \leq TV(\eta_0) \sup |f'| \tau$  for all  $\tau > 0$ . Combination yields  $\|\eta(\xi, \tau) - \eta(\xi, 0)\|_{L^1} \leq TV(\eta_0) \sup |f'| \tau$  for all  $\tau > 0$ ; thus,  $\|\eta(\xi, \tau) - \eta(\xi, 0)\|_{L^1}$  converges to zero as  $\tau \rightarrow 0^+$ . Since the initial condition given in (5.0.1) is  $\eta(\xi, 0) = \eta_0(\xi)$  for all  $\xi \in \mathbb{R}$ , it follows that  $\eta(\xi, \tau) \rightarrow \eta_0(\xi)$  as  $\tau \rightarrow 0^+$ , and the limit function  $\eta(\xi, \tau)$  exactly satisfies the given initial condition in (5.0.1). Hence, for all time, we have convergence to the initial condition similar to Theorem 5.0.1:

$$\left\| \eta(\xi, \tau) - \eta_0(\xi) \right\|_{L^1(\mathbb{R})} \leq TV(\eta_0) \sup |f'| \tau \quad \text{for all } \tau \geq 0.$$

### 5.3 Proof: Limit Function is an Entropy Solution of (5.0.1)

In this section, a proof of the existence of classical entropy solutions to the Cauchy problem (5.0.1) is presented. We prove that the limit function found in the previous section satisfies an entropy inequality throughout the characteristic plane.

Let  $U(\eta^{h,h})$  be an arbitrary  $C^2$  strictly convex entropy function, and  $F(\eta^{h,h})$  be a corresponding entropy flux with  $F'(\eta^{h,h}) = \sigma f'(\eta^{h,h}) U'(\eta^{h,h})$  for  $\sigma$  given by (2.4.1). Hence, the discontinuous definition of the entropy flux is  $F'(\eta^{h,h}) = \tilde{f}'(\eta^{h,h}) U'(\eta^{h,h})$  where

$$\tilde{f}'(\eta^{h,h}) = \begin{cases} f'(\eta^{h,h}), & \frac{\partial \eta^{h,h}}{\partial \tau} < 0, \\ (1 - \varepsilon) f'(\eta^{h,h}), & \frac{\partial \eta^{h,h}}{\partial \tau} > 0. \end{cases} \quad (5.3.1)$$

In cross-hatch regions of the characteristic plane where the solution  $\eta^{h,h}$  is constant between propagating wave-fronts, it follows that

$$\left[ U(\eta^{h,h}) \right]_{\tau} + \left[ F(\eta^{h,h}) \right]_{\xi} = U'(\eta^{h,h}) \eta_{\tau}^{h,h} + F'(\eta^{h,h}) \eta_{\xi}^{h,h} = 0. \quad (5.3.2)$$

In this section, we prove that wave-fronts in  $\eta^{h,h}$  that are propagating as admissible shocks or rarefactions in the rest of the characteristic plane also satisfy the entropy inequality

$$\left[ U(\eta^{h,h}) \right]_{\tau} + \left[ F(\eta^{h,h}) \right]_{\xi} \leq 0. \quad (5.3.3)$$

### 5.3.1 Classical Shocks Satisfy the Entropy Inequality

Solutions to the Riemann problem with  $\eta_L < \eta_R$  are classical shock waves satisfying the Lax entropy condition because the faster characteristics enter the shock from both sides, see Section 3.2. Such wave-fronts have a piecewise constant solution given by

$$\eta^{h,h}(\xi, \tau) = \begin{cases} \eta_L, & \xi < \Lambda \tau, \\ \eta_R, & \xi > \Lambda \tau, \end{cases} \quad (5.3.4)$$

with speed  $\Lambda$  given in (3.2.2) for a  $C^2$  strictly concave flux (2.4.3).

**Lemma 5.3.1.** *Shock wave-fronts (5.3.4) that satisfy the Lax entropy condition satisfy the entropy inequality (5.3.3).*

**Proof:** As described in Section 3.2, shock waves that are admissible in the sense of Lax have  $\eta_L < \eta_R$  due to the concavity of the dual flux curves. For  $\eta > \eta_L$ , let

$$\Lambda(\eta) = \frac{\sigma [f(\eta) - f(\eta_L)]}{\eta - \eta_L} \implies \Lambda'(\eta) = \frac{\sigma f'(\eta) - \Lambda(\eta)}{\eta - \eta_L}, \quad (5.3.5)$$

as in [4, 38]. For any shock connecting  $\eta_L$  up to  $\eta$ , it is apparent from Figures 5.3.1(a)-(b) that  $\sigma f'(\eta) < \Lambda(\eta)$  for both  $\sigma = 1$  and  $\sigma = 1 - \varepsilon$ ; therefore,

$$\Lambda'(\eta) < 0. \quad (5.3.6)$$

Since the entropy function  $U$  is  $C^2$  and strictly convex, it follows that  $U'' > 0$ , and for  $\eta > \eta_L$ ,

$$U'(\eta) > \frac{U(\eta) - U(\eta_L)}{\eta - \eta_L}. \quad (5.3.7)$$

For  $\eta > \eta_L$ , we define  $E(\eta) = -\Lambda(\eta) [U(\eta) - U(\eta_L)] + F(\eta) - F(\eta_L)$  for convex entropy pairs  $(U, F)$ . Differentiation yields

$$\begin{aligned} E'(\eta) &= -\Lambda(\eta) U'(\eta) - \Lambda'(\eta) [U(\eta) - U(\eta_L)] + F'(\eta) \\ &= U'(\eta) [\sigma f'(\eta) - \Lambda(\eta)] - \Lambda'(\eta) [U(\eta) - U(\eta_L)] && \text{by definition of } F' \\ &= \Lambda'(\eta) \left( U'(\eta) (\eta - \eta_L) - [U(\eta) - U(\eta_L)] \right) && \text{by (5.3.5)} \\ &< 0 \end{aligned}$$

for  $\eta > \eta_L$  by (5.3.6) and (5.3.7). If  $\eta = \eta_L$ , there is no shock between  $\eta$  and  $\eta_L$ , so  $E(\eta_L) = 0$  and  $E'(\eta_L) = 0$ . Since we showed that  $E$  strictly decreases as  $\eta$  increases from  $\eta_L$ , it follows that  $E(\eta_R) < 0$  for  $\eta_R > \eta_L$ , as in Figure 5.3.1(c). Hence, for classical admissible shocks with  $\eta_L < \eta_R$ ,

$$-\Lambda [U(\eta_R) - U(\eta_L)] + F(\eta_R) - F(\eta_L) < 0, \quad (5.3.8)$$

which, in the sense of distributions, is equivalent to the entropy inequality in (5.3.3).  $\square$

### 5.3.2 Admissible Shock Entropy Inequality: Example

We have just showed that the entropy inequality holds across classical shocks for all convex entropy functions and concave flux functions. In this section, we demonstrate that, indeed, the inequality holds for a specific convex entropy and concave discontinuous flux.

Equation (2.4.2) has admissible stable shock solutions when  $\eta_L < \eta_R$  in the sense of Lax [25]. For this example, consider  $\mathcal{M} = 1$ . From Section 3.2,  $\sigma = 1$  across a forward shock, so the characteristics determined by the upper flux curve impinge on the shock; hence,  $\Lambda = 1 - \eta_L - \eta_R$  and  $f'(\eta_R) < \Lambda < f'(\eta_L)$ . Thus, for forward shocks, we need only consider the characteristics



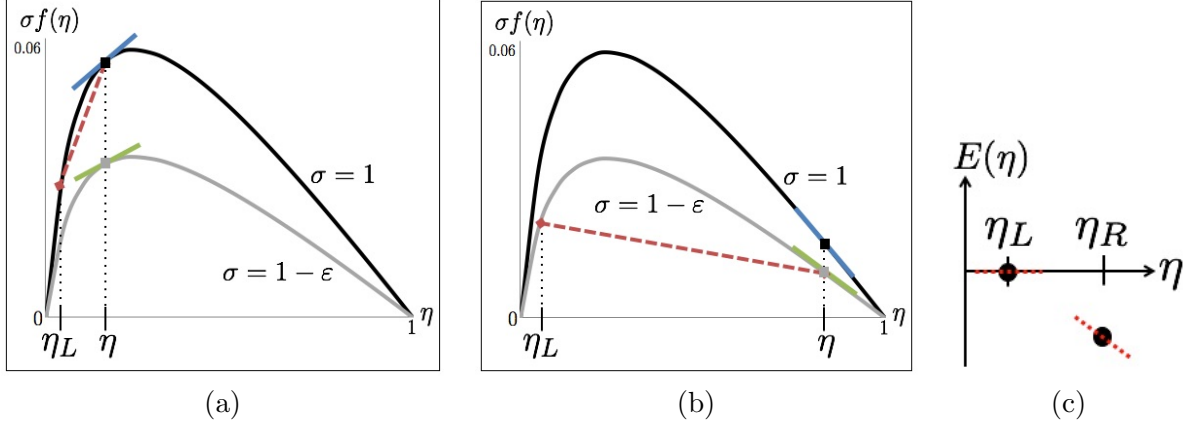


Figure 5.3.1: For forward shocks with  $\Lambda(\eta) > 0$  in (a) and backward shocks with  $\Lambda(\eta) < 0$  in (b), the characteristics determined by upper (in blue) and lower (in green) flux curves are slower (more negative) than the shocks (in red). (c) Since  $E(\eta_L) = E'(\eta_L) = 0$  and  $E'(\eta) < 0$  for all  $\eta > \eta_L$ , it follows that  $E(\eta_R) < 0$ .

from the upper flux curve with  $\sigma f(\eta) = \eta - \eta^2$  in (2.4.3). Suppose we let the convex entropy function be defined as

$$U(\eta) = \eta^2 - \eta. \quad (5.3.9)$$

Hence,  $F'(\eta) = \sigma f'(\eta) U'(\eta) = -4\eta^2 + 4\eta - 1$ . It follows that

$$\begin{aligned} \eta_L < \eta_R &\implies \frac{1}{3}(\eta_L - \eta_R)^3 < 0 \implies \\ &- [1 - \eta_L - \eta_R] \left[ \eta_R^2 - \eta_R - \eta_L^2 + \eta_L \right] - \frac{4}{3} \eta_R^3 + 2\eta_R^2 - \eta_R + \frac{4}{3} \eta_L^3 - 2\eta_L^2 + \eta_L < 0 \\ \implies &-\Lambda \left[ U(\eta_R) - U(\eta_L) \right] + F(\eta_R) - F(\eta_L) < 0, \end{aligned}$$

so the entropy inequality (5.3.3) is satisfied for admissible forward shock solutions of (2.4.2).

Similarly, recall Section 3.2 where  $\sigma = 1 - \varepsilon > 0$  across an admissible backward shock, so the characteristics determined by the lower flux curve impinge on the shock. For admissible backward shocks,  $\Lambda = \sigma [1 - \eta_L - \eta_R]$  and  $\sigma f'(\eta_R) < \Lambda < \sigma f'(\eta_L)$ . Hence, we consider the characteristics from the lower flux curve with  $\sigma f(\eta) = (1 - \varepsilon) [\eta - \eta^2]$  which leads to a separate entropy flux  $F$  such that  $F'(\eta) = (1 - \varepsilon) [-4\eta^2 + 4\eta - 1]$  for the previously defined entropy function  $U$  in (5.3.9). It follows that  $(1 - \varepsilon)(\eta_L - \eta_R)^3 < 0$ , and we obtain the entropy inequality as in the case of forward admissible shocks; hence, backward shock solutions of (2.4.2) that satisfy the Lax entropy condition are entropy admissible.

Since stationary shocks are a limiting case of either admissible forward or backward shocks, the entropy inequality (5.3.3) holds for a specific convex entropy function (5.3.9) and concave flux (2.4.3), despite the discontinuous switch parameter  $\sigma$  in the flux function.

### 5.3.3 Rarefaction Waves Satisfy the Entropy Inequality

In the wave-front tracking algorithm, as we construct solution  $\eta^{h,h}$ , recall that wave-fronts with  $\eta_R < \eta_L$  yield rarefaction fans which are replaced by expansion shocks (with magnitudes no greater than  $h$ ) to obtain a piecewise constant approximation. In  $\eta^{h,h}$ , a propagating front  $\xi = y_m(\tau)$  between two constant states can be either a classical or expansion shock. Define  $\eta_m^L := \eta^{h,h}(y_m(\tau)^-, \tau)$  as the constant solution to the left of wave-front  $y_m$  and  $\eta_m^R := \eta^{h,h}(y_m(\tau)^+, \tau)$  as the solution value just to the right of a given shock  $y_m$ . Since both admissible and expansion shocks in  $\eta^{h,h}$  are constructed to satisfy the Rankine-Hugoniot jump condition, we define the constant speed of propagation for wave-front  $y_m$  as

$$y'_m = \frac{\sigma \left[ f(\eta_m^L) - f(\eta_m^R) \right]}{\eta_m^L - \eta_m^R}, \quad (5.3.10)$$

for discontinuous switch parameter  $\sigma$  in (2.4.1). Expansion shocks  $y_m$  in  $\eta^{h,h}$  are constructed to satisfy

$$\left| \eta_m^L - \eta_m^R \right| \leq h. \quad (5.3.11)$$

Define  $V$  to be an arbitrary portion of the characteristic plane through which only wave-front  $\xi = y_m(\tau)$  propagates, as shown in Figure 5.3.2(a), and let  $\partial V$  denote the boundary of  $V$ . Let  $V_{-/ +}$  be the portion of  $V$  to the left/right of the propagating front. In Figure 5.3.2(b), notice that the unit outward normal vector from  $V_-$  along  $\xi = y_m(\tau)$  is  $\hat{n} = \frac{1}{\sqrt{(y'_m)^2 + 1}} (-y'_m, 1)$ .

Let  $\psi(\xi, \tau) \geq 0$  be an arbitrary smooth test function with compact support,  $\psi \in C_0^1(V)$ . For entropy pair  $(U, F)$ , define  $\omega(\psi)$  as

$$\omega(\psi) := - \iint_V \left[ U(\eta^{h,h}) \psi_\tau + F(\eta^{h,h}) \psi_\xi \right] d\xi d\tau = - \iint_{V_-} [\vec{\mathcal{F}} \cdot \nabla \psi] d\xi d\tau - \iint_{V_+} [\vec{\mathcal{F}} \cdot \nabla \psi] d\xi d\tau$$

where  $\vec{\mathcal{F}} = (U(\eta^{h,h}), F(\eta^{h,h}))$  and  $\nabla = (\frac{\partial}{\partial \tau}, \frac{\partial}{\partial \xi})$ . Integration by parts and Green's identity yield

$$\iint_{V_-} [\vec{\mathcal{F}} \cdot \nabla \psi] d\xi d\tau = \int_{\partial V_-} [\psi \vec{\mathcal{F}} \cdot \hat{n}] ds - \iint_{V_-} [\psi \nabla \cdot \vec{\mathcal{F}}] d\xi d\tau. \quad (5.3.12)$$

Since the solution  $\eta^{h,h}$  is smooth inside  $V_-$ , it follows from (5.3.2) that

$$\iint_{V_-} [\psi \nabla \cdot \vec{\mathcal{F}}] d\xi d\tau = \iint_{V_-} \psi \left( \left[ U(\eta^{h,h}) \right]_{\tau} + \left[ F(\eta^{h,h}) \right]_{\xi} \right) d\xi d\tau = 0.$$

From Figure 5.3.2(b), we can distinguish between portions of the boundary  $\partial V$ ,

$$\int_{\partial V_-} [\psi \vec{\mathcal{F}} \cdot \hat{n}] ds = \int_{\partial V_- | \xi = y_m(\tau)} [\psi \vec{\mathcal{F}} \cdot \hat{n}] ds + \int_{\partial V_- | \xi \neq y_m(\tau)} [\psi \vec{\mathcal{F}} \cdot \hat{n}] ds,$$

and find  $\int_{\partial V_- | \xi \neq y_m(\tau)} [\psi \vec{\mathcal{F}} \cdot \hat{n}] ds = 0$  because  $[\partial V_- | \xi \neq y_m(\tau)] \in \partial V$  and  $\psi$  has compact support on  $V$ . Expression (5.3.12) simplifies to

$$\iint_{V_-} [\vec{\mathcal{F}} \cdot \nabla \psi] d\xi d\tau = \int_{\partial V_- | \xi = y_m(\tau)} \frac{\psi(\xi, \tau)}{\sqrt{(y'_m)^2 + 1}} \left( -U(\eta^{h,h}) y'_m + F(\eta^{h,h}) \right) ds$$

for  $\hat{n}$  as previously defined. The propagating front passes through  $V$  between times  $\tau_1$  and  $\tau_2$  on Figure 5.3.2(a). We transform the above expression to obtain

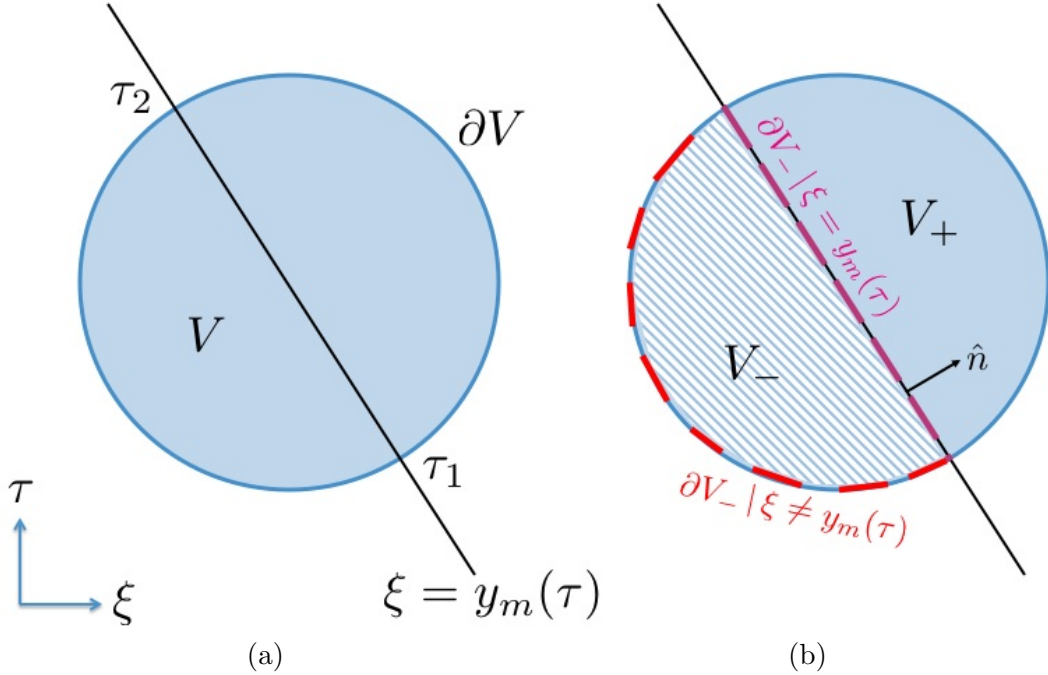


Figure 5.3.2: (a) Arbitrary volume  $V$  through which front  $\xi = y_m(\tau)$  propagates, and (b) details of volume  $V_-$  and  $\partial V_-$ .

$$\iint_{V_-} [\vec{\mathcal{F}} \cdot \nabla \psi] d\xi d\tau = \int_{\tau_1}^{\tau_2} \psi(y_m(\tau), \tau) [-U(\eta_m^L) y'_m + F(\eta_m^L)] d\tau.$$

Using the unit outward normal vector from  $V_+$  along  $\xi = y_m(\tau)$ , we obtain a similar expression for  $\iint_{V_+} [\vec{\mathcal{F}} \cdot \nabla \psi] d\xi d\tau$  from which it follows that

$$\omega(\psi) = \int_{\tau_1}^{\tau_2} \psi(y_m(\tau), \tau) \left[ -y'_m \left( U(\eta_m^R) - U(\eta_m^L) \right) + F(\eta_m^R) - F(\eta_m^L) \right] d\tau$$

for one arbitrary propagating front  $\xi = y_m(\tau)$  through an arbitrary volume  $V$  of the characteristic plane. This can be extended to the entire solution plane  $\mathbb{R} \times \mathbb{R}^+$  traversed by all propagating fronts as in LeFloch [26]. Let  $\varphi(\xi, \tau) \geq 0$  be an arbitrary smooth test function with compact support,  $\varphi \in C_0^1(\mathbb{R} \times \mathbb{R}^+)$ . Define  $\Omega(\varphi)$  such that

$$\Omega(\varphi) := - \int_0^\infty \int_{-\infty}^\infty \left[ U(\eta^{h,h}) \varphi_\tau + F(\eta^{h,h}) \varphi_\xi \right] d\xi d\tau.$$

Notice that  $\Omega$  sums  $\omega$  for each propagating front between interactions for  $\tau \in \mathbb{R}^+$  since portions of the characteristic plane between admissible and/or expansion shocks have constant solution and, by (5.3.2), are crushed and do not contribute to  $\Omega$ . It follows that

$$\Omega(\varphi) = \sum_{\text{shocks}} \int_0^\infty \varphi(y_m(\tau), \tau) \left[ -y'_m \left( U(\eta_m^R) - U(\eta_m^L) \right) + F(\eta_m^R) - F(\eta_m^L) \right] d\tau. \quad (5.3.13)$$

For admissible shocks,  $-y'_m \left( U(\eta_m^+) - U(\eta_m^-) \right) + F(\eta_m^+) - F(\eta_m^-) < 0$  by (5.3.8), and by definition,  $\varphi(y_m(\tau), \tau) \geq 0$ ; hence,

$$\sum_{\substack{\text{classical} \\ \text{shocks}}} \int_0^\infty \varphi(y_m(\tau), \tau) \left[ -y'_m \left( U(\eta_m^+) - U(\eta_m^-) \right) + F(\eta_m^+) - F(\eta_m^-) \right] d\tau \leq 0.$$

Since (5.3.13) is the sum over all classical shocks and expansion shocks, it follows that

$$\begin{aligned} \Omega(\varphi) &\leq \sum_{\substack{\text{expansion} \\ \text{shocks}}} \int_0^\infty \varphi(y_m(\tau), \tau) \left[ -y'_m \left( U(\eta_m^R) - U(\eta_m^L) \right) + F(\eta_m^R) - F(\eta_m^L) \right] d\tau \\ &\leq \sum_{\substack{\text{expansion} \\ \text{shocks}}} \int_0^\infty \varphi(y_m(\tau), \tau) \left| \int_{\eta_m^L}^{\eta_m^R} \left[ -y'_m U'(n) + F'(n) \right] dn \right| d\tau, \end{aligned} \quad (5.3.14)$$

since  $y'_m$  is a constant shock speed for any expansion shock from  $\eta_m^L$  to  $\eta_m^R$  with  $\eta_m^L > \eta_m^R$ .

Combining the piecewise definition of the flux (5.3.1) with the speed given by (5.3.10) for  $\sigma = 1$  or  $\sigma = 1 - \varepsilon$  yields

$$\begin{aligned} \left| \int_{\eta_m^L}^{\eta_m^R} \left[ -y'_m U'(n) + F'(n) \right] dn \right| &\leq \left| \int_{\eta_m^L}^{\eta_m^R} U'(n) \left[ \frac{\tilde{f}(\eta_m^R) - \tilde{f}(\eta_m^L)}{\eta_m^L - \eta_m^R} + \tilde{f}'(n) \right] dn \right| \\ &\leq \left| \int_{\eta_m^L}^{\eta_m^R} \frac{U'(n)}{\eta_m^L - \eta_m^R} \left[ \tilde{f}(\eta_m^R) - \tilde{f}(\eta_m^L) + \tilde{f}'(\eta_m^R)(\eta_m^L - \eta_m^R) \right] dn \right|, \end{aligned}$$

because  $\tilde{f}'(n) \leq \tilde{f}'(\eta_m^R)$  for any  $n \geq \eta_m^R$  as shown in Figure 5.3.3. For some  $\hat{\eta}$  between  $\eta_m^R$  and  $\eta_m^L$ , a Taylor approximation yields

$$\tilde{f}(\eta_m^L) = \tilde{f}(\eta_m^R) + \tilde{f}'(\eta_m^R)(\eta_m^L - \eta_m^R) + \frac{1}{2} \tilde{f}''(\hat{\eta})(\eta_m^L - \eta_m^R)^2.$$

Hence,

$$\begin{aligned} \left| \int_{\eta_m^L}^{\eta_m^R} \left[ -y'_m U'(n) + F'(n) \right] dn \right| &\leq \left| \frac{1}{\eta_m^R - \eta_m^L} \int_{\eta_m^L}^{\eta_m^R} U'(n) \tilde{f}''(\hat{\eta})(\eta_m^L - \eta_m^R)^2 dn \right| \\ &\leq \left| \frac{1}{\eta_m^R - \eta_m^L} \sup_{0 \leq \eta \leq 1} |U'| \sup_{0 \leq \eta \leq 1} |\tilde{f}''| (\eta_m^L - \eta_m^R)^2 \int_{\eta_m^L}^{\eta_m^R} dn \right| \end{aligned}$$

by the strict concavity of the flux  $f$  and entropy flux  $U$ .

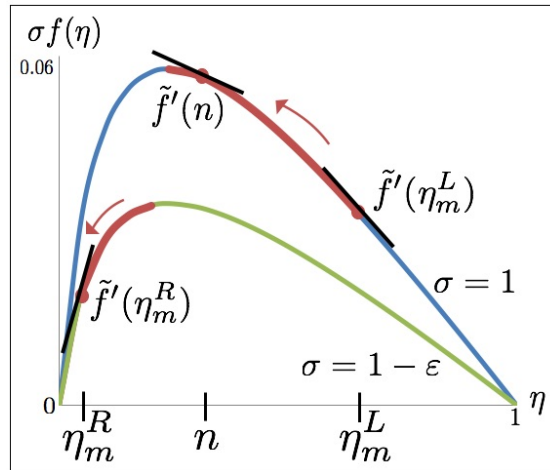


Figure 5.3.3: For expansion shock  $y_m$ , the black tangent lines to the discontinuous flux curves always have  $\tilde{f}'(\eta_m^L) \leq \tilde{f}'(n) \leq \tilde{f}'(\eta_m^R)$  for  $n \in [\eta_m^R, \eta_m^L]$  and  $\tilde{f}$  given by (5.3.1).

By (5.3.11),  $\left| \eta_m^L - \eta_m^R \right| \leq h$ , thus,

$$\left| \int_{\eta_m^L}^{\eta_m^R} \left[ -y'_m U'(n) + F'(n) \right] dn \right| \leq h \sup_{0 \leq \eta \leq 1} |U'| \sup_{0 \leq \eta \leq 1} |\tilde{f}''| \left| \eta_m^L - \eta_m^R \right|.$$

Recall that at any  $\tau \in \mathbb{R}^+$ , the total number of propagating fronts in  $\eta^{h,h}$  is finite; let  $\mathfrak{M}$  be the finite number of expansion shocks. Therefore, (5.3.14) becomes

$$\begin{aligned} \Omega(\varphi) &\leq \sum_{m=1}^{\mathfrak{M}} \int_0^\infty \varphi(y_m(\tau), \tau) h \sup_{0 \leq \eta \leq 1} |U'| \sup_{0 \leq \eta \leq 1} |\tilde{f}''| \left| \eta_m^L - \eta_m^R \right| d\tau \\ &\leq h \sup_{0 \leq \eta \leq 1} |U'| \sup_{0 \leq \eta \leq 1} |\tilde{f}''| \sup_{\tau \in \mathbb{R}^+} \left[ TV(\eta^{h,h}(\xi, \tau)) \right] \int_0^\infty \sup_{\xi \in \mathbb{R}} \varphi(\xi, \tau) d\tau. \end{aligned} \quad (5.3.15)$$

Since  $U$  is convex and continuous on a closed bounded interval,  $\sup_\eta |U'|$  is bounded. Since  $\eta^{h,h} \in [0, 1]$ , it follows from (2.4.3) that  $\sup_\eta |\tilde{f}''(\eta^{h,h})| = |f''(0)|$ , a bounded constant determined by the mobility in the aquifer. By Table 4.3, total variation is bounded for the approximation. Finally, since  $\varphi \in C_0^1(\mathbb{R} \times \mathbb{R}^+)$ , the final integral is bounded.

Hence, as  $h \rightarrow 0$  in (5.3.15),  $\Omega(\varphi) \leq 0$  for all convex entropy pairs  $(U, F)$ . From Section 3.4, as  $h \rightarrow 0$ , the strength of approximating expansion shocks given by (5.3.11) diminishes, and *continuous rarefaction solutions are obtained in the limit*; this limiting property is shown in Figure 5.3.4. By (5.2.2), as  $h \rightarrow 0$ ,  $\eta^{h,h}(\xi, \tau) \rightarrow \eta(\xi, \tau)$ . Consequently, in the limit as  $h \rightarrow 0$ ,

$$\begin{aligned} \Omega(\varphi) \leq 0 &\implies - \int_0^\infty \int_{-\infty}^\infty \left[ U(\eta) \varphi_\tau + F(\eta) \varphi_\xi \right] d\xi d\tau \leq 0 \\ &\implies \int_0^\infty \int_{-\infty}^\infty \varphi(\xi, \tau) \left[ U(\eta)_\tau + F(\eta)_\xi \right] d\xi d\tau + \int_{-\infty}^\infty \varphi(\xi, 0) U(\eta(\xi, 0)) d\xi \leq 0, \end{aligned}$$

so the entropy inequality (5.3.3) is satisfied in the weak sense across rarefaction fans.

## 5.4 Existence of a Classical Entropy Solution

Hence, we have completed the proof of Theorem 5.0.1, and the Cauchy problem (5.0.1) has a classical entropy solution. To summarize, in this chapter, it has been shown that:

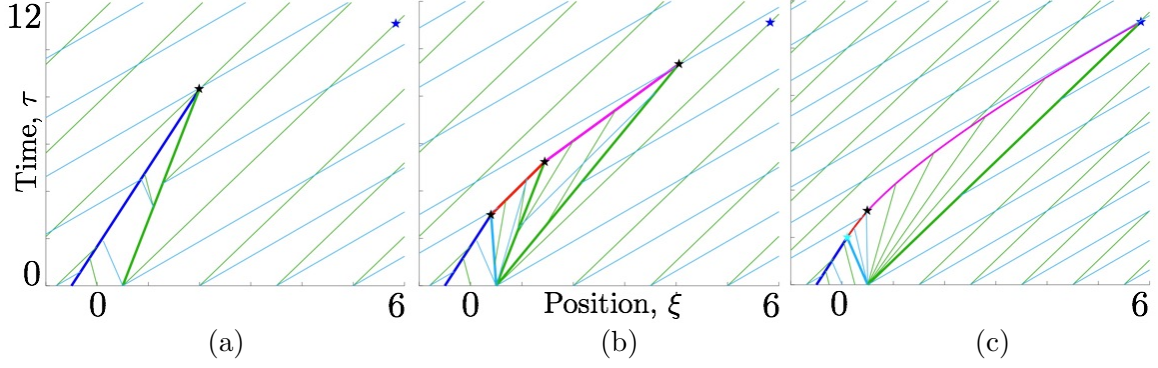


Figure 5.3.4: As the size of the expansion shocks decreases (and therefore the number of expansion shocks increases from one (a) to three (b)), the rarefaction is obtained in the limit (c). Here,  $\eta_L = \eta_R = 0.1$ ,  $\eta_M = 0.6$ , and  $\varepsilon = 0.4$ .

- The wave-front tracking approximations,  $\eta^h = \eta^h(\xi, \tau)$ , based on solutions to Riemann problems from Chapters 3 and 4 are well-defined globally in time. The total number of waves in  $\eta^h$  is uniformly bounded in time.
- As shown in Section 5.2.1, for  $\eta_0 \in L^1(\mathbb{R}) \cap BV(\mathbb{R})$  with  $0 \leq \eta_0 \leq 1$ , the approximate solutions,  $\eta^h$ , satisfy the uniform estimates

$$\inf(\eta_0) \leq \eta^h(\xi, \tau) \leq \sup(\eta_0), \quad \xi \in \mathbb{R}, \tau > 0,$$

$$TV(\eta^h(\xi, \tau)) \leq TV(\eta_0), \quad \xi \in \mathbb{R}, \tau \geq 0,$$

$$\left\| \eta^h(\xi, \tau_2) - \eta^h(\xi, \tau_1) \right\|_{L^1(\mathbb{R})} \leq TV(\eta_0) \sup |f'| |\tau_2 - \tau_1|, \quad \xi \in \mathbb{R}, \tau_1, \tau_2 \geq 0.$$

- A subsequence  $\eta^{h,h}$  of  $\eta^h$  converges to a classical entropy-admissible solution  $\eta = \eta(\xi, \tau)$  of the Cauchy problem (5.0.1),

$$\eta^{h,h}(\xi, \tau) \rightarrow \eta(\xi, \tau) \quad \text{in } L^1_{\text{loc}} \quad \text{for all } \tau \in \mathbb{R}^+, \xi \in \mathbb{R},$$

$$\text{and } \left[ U(\eta) \right]_{\tau} + \left[ F(\eta) \right]_{\xi} \leq 0 \text{ in the limit as } h \rightarrow 0 \text{ for every convex entropy pair } (U, F).$$

We also showed that the limit function  $\eta(\xi, \tau)$  satisfies

$$\inf(\eta_0) \leq \eta(\xi, \tau) \leq \sup(\eta_0), \quad \xi \in \mathbb{R}, \tau > 0,$$

$$TV(\eta(\xi, \tau)) \leq TV(\eta_0), \quad \xi \in \mathbb{R}, \tau \geq 0,$$

$$\left\| \eta(\xi, \tau_2) - \eta(\xi, \tau_1) \right\|_{L^1(\mathbb{R})} \leq TV(\eta_0) \sup |f'| |\tau_2 - \tau_1|, \quad \xi \in \mathbb{R}, \tau_1, \tau_2 \geq 0,$$

and, for all  $\tau \geq 0$ , the initial condition has the property

$$\left\| \eta(\xi, \tau) - \eta_0 \right\|_{L^1(\mathbb{R})} \leq TV(\eta_0) \sup |f'| \tau.$$



---

Comprehensive Example

---

In Chapter 5, we established the existence of entropy solutions of the Cauchy problem (5.0.1) for plumes of  $\text{CO}_2$  with bounded variation and any initial geometry. Chapter 4 provided new clarity on how the resulting wave interactions work, and we now understand new patterns that emerged during the construction of wave solutions. In this chapter, we provide an example that demonstrates the need to include cross-hatch characteristics whilst constructing solutions, and we illustratively justify the continuum case with expansion shocks. At the end of this chapter, we translate the results of an example with dimensionless parameters back to physical parameters.

## 6.1 Rarefaction-Shock-Rarefaction Solution

We consider the conservation law (2.4.2) and an initial plume with geometry shown in Figure 6.1.1(a) and given by:

$$\eta_0(\xi) = \begin{cases} 0, & \xi \leq -26, \\ \eta_L = 0.3, & -26 < \xi \leq -2.5, \\ \eta_{rare} = -0.1\xi + 0.05, & -2.5 < \xi \leq -0.5, \\ \eta_M = 1, & -0.5 < \xi \leq 0.5, \\ \eta_R = 0.2, & 0.5 < \xi < 10, \\ 0, & \xi \geq 10. \end{cases} \quad (6.1.1)$$

This initial condition has compact support since the plume height is zero when  $\xi \notin (-26, 10)$ . For  $\xi \in (-2.5, -0.5)$ , the initial plume features a non-centered rarefaction fan with  $\eta_{rare} < \eta^*$ ; hence, *the characteristic speeds in the non-centered rarefaction are determined by the lower flux curve*. Additionally, the initial plume has shock waves emanating from  $\xi = -26$  and  $-0.5$  and rarefaction waves centered at  $\xi = 0.5$  and  $10$ , as emphasized in Figure 6.1.1(b). The initial plume (6.1.1) satisfies the conditions of Theorem 5.0.1; hence, the resulting Cauchy problem admits an entropy solution.

For early time, the shock solution unfolds in a manner similar to the example in Section 4.2.1; however, the solution differs because, on the left, this example has a rarefaction rather than a constant state. The position for a shock abutting a non-centered rarefaction is determined numerically since we do not have a closed formula for the result of this wave interaction. In the Case A example, the initial backward shock travels at a constant speed until the shock begins to interact with the rarefaction on the right, whereas in this example, the interaction between the non-centered rarefaction fan on the left and  $\eta_M=1$  on the right yields a shock with increasing shock speed, shown in blue in Figure 6.1.2. At time (a) in the same figure, the non-centered rarefaction on the left begins to interact with the rarefaction on the right between  $\eta_M$  and  $\eta_R$ , resulting in a backward shock until point (b) where the shock becomes stationary then advances as a forward shock until time (c). After this point, the characteristics entering the shock from the rarefaction on the left and from the rarefaction on the right have characteristic speeds determined by the lower flux curve. The resulting *forward shock speed is determined by the upper flux curve*.

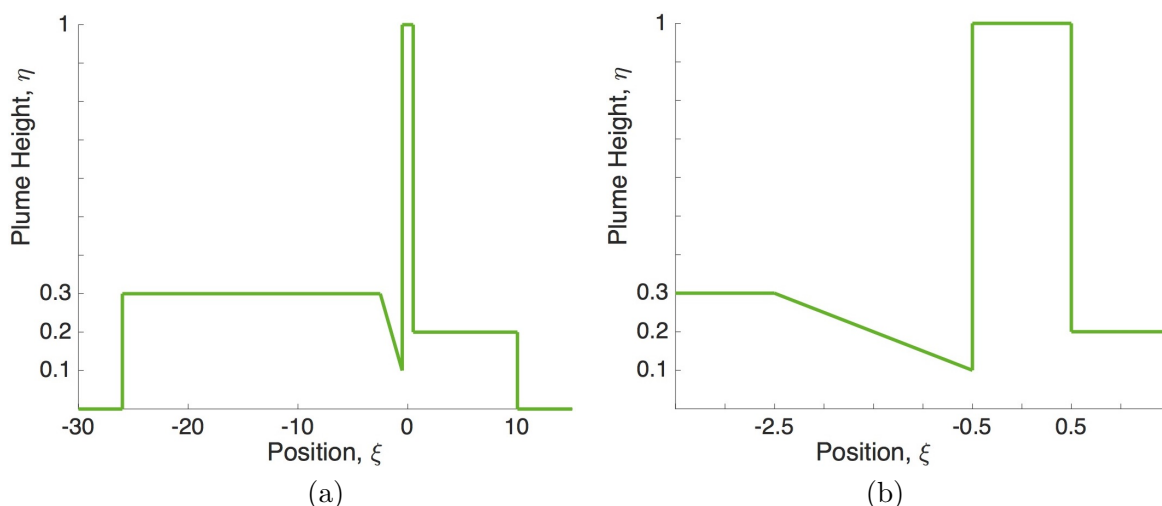


Figure 6.1.1: Initial condition where (b) is a magnification of a portion of (a).

## 6.2 Graze Characteristic Leads to Cross-hatch Characteristics

At point (d) in Figure 6.1.2, the shock speed equals the speed of the entering characteristic from the non-centered rarefaction on the left; we define  $\eta_{\text{graze}}$  as the solution associated with

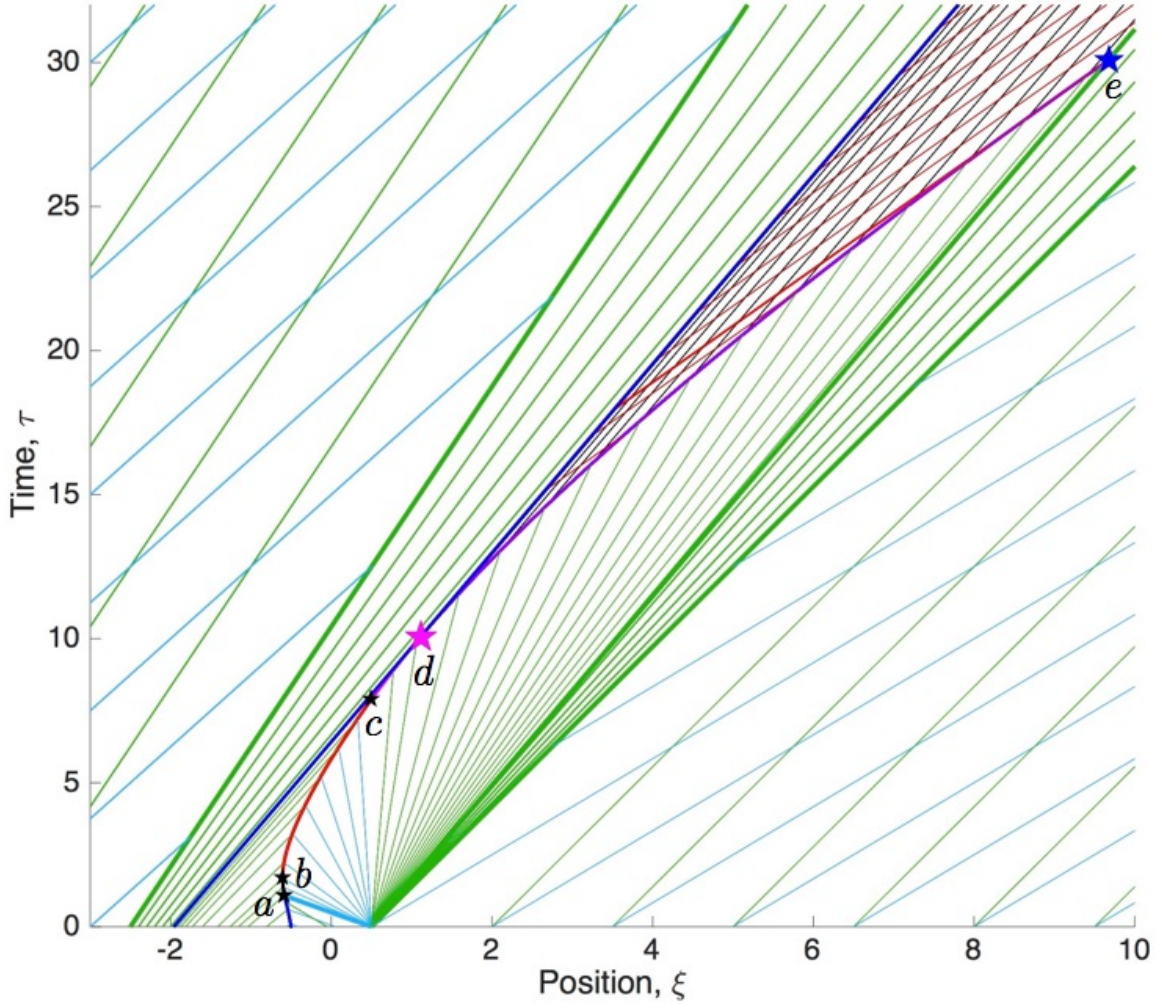


Figure 6.1.2: Exact solution for  $\eta_L = 0.3$ ,  $\eta_0(-0.5) = 0.1$ ,  $\eta_M = 1$ ,  $\eta_R = 0.2$ ,  $\mathcal{M} = 1$  and  $\varepsilon = 0.4$ . The non-centered rarefaction on the right interacts with  $\eta_M$  until point (a), when the plume breaks away from the bottom of the aquifer. The two rarefactions begin to interact at point (a) to yield a shock that becomes stationary at (b). After point (c), the speeds of both rarefactions are reduced due to trapping. At point (d), the shock speed equals the speed of the entering characteristic corresponding to  $\eta_{\text{graze}}$  in the non-centered rarefaction, resulting in a constant region with cross-hatch characteristics. The faster characteristics, in red, now enter the shock from the left. The shock persists until time  $\tau_e$ , when the  $\eta_{\text{graze}}$  characteristic within the rarefaction enters the shock from the right, point (e).

this characteristic. Though this result resembles point ① in Figure 4.2.1(b) where the slower characteristic on the left grazed the shock, there is a significant caveat in this example: characteristics within rarefactions are well-defined from Chapter 3. Hence, unlike Section 4.2.1, there is no faster characteristic on the left that can bring information into the shock; however, the speed of the shock continues to increase because the solution within the rarefaction on the right is continuously decreasing.

After point (d), interesting phenomena arise since the constant solution value  $\eta_{\text{graze}}$  persists, yielding a constant region between the characteristic associated with  $\eta_{\text{graze}}$  in the rarefaction on the left and the shock on the right. This constant region of the characteristic plane is filled with cross-hatch characteristics, per Section 3.1. Without cross-hatch characteristics, there would be a non-physical gap in the characteristic plane. Regarding the resulting shock between the constant state  $\eta_{\text{graze}}$  on the left and the rarefaction on the right: sans cross-hatch characteristics, there would be no incoming information from the left side of the shock. *The faster characteristics, determined by the upper flux curve, will now enter the shock.*

### 6.3 Expansion Shock Justification

We use expansion shocks to provide a justification of the emergent constant state  $\eta_{\text{graze}}$  in Figure 6.1.2. The non-centered rarefaction and the rarefaction centered at  $\xi = 0.5$  in the initial condition, Figure 6.1.1(b), are approximated with expansion shocks, see Figure 6.3.1. The expansion shock speeds are indicated by the directions and lengths of corresponding red arrows, and the backward shock between  $\eta = 0.1$  and 1 is shown.

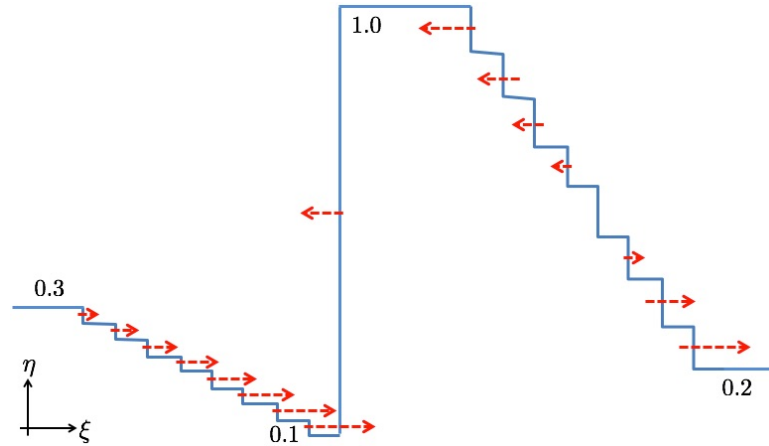


Figure 6.3.1: Expansion shock approximations of initial rarefactions.

Figures 6.3.2(a)-(c) correspond to points (a)-(c) on Figure 6.1.2. In (a), the backward shock interacts with the fastest expansion shock on the left; in (b), the expansion shocks on the left reduce the classical shock speed to zero. In (c), the forward classical shock encounters the expansion shock with zero speed approximating the vertical characteristic in the rarefaction on the right. After this, the shock continues to gain speed due to the interactions with faster expansion shocks on the left.

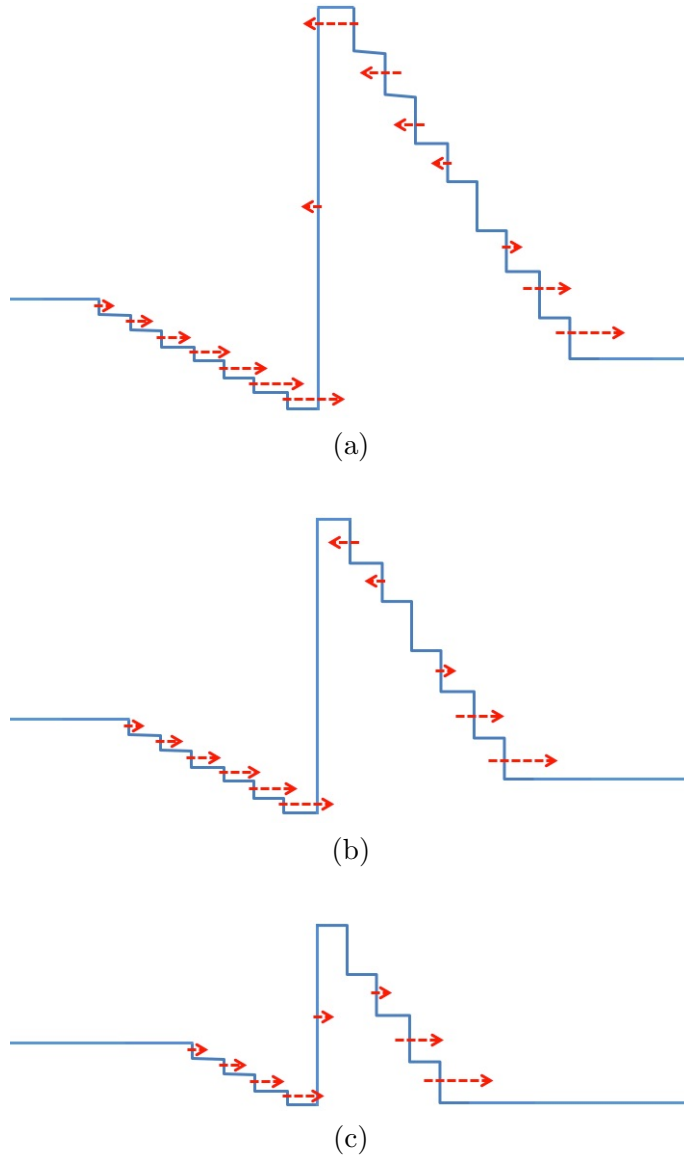


Figure 6.3.2: Expansion shock representation of the continuous solution in Figure 6.1.2, with corresponding points (a)-(c).

The grazing characteristic from the continuous rarefaction on the left grazes the classical shock at point (d) in Figure 6.1.2. The corresponding piecewise constant states are shown in Figure 6.3.3(d) where the speed of the expansion shock on the left equals the speed of the entropy-satisfying shock. Henceforth, *the expansion shock and classical shock will not approach each other*; however, the classical compressive shock will continue to gain speed as it interacts with slower expansion shocks on the right, Figure 6.3.3(de). This continues until the shock encounters the expansion shock corresponding to a jump down from  $\eta_{\text{graze}}$ , rendering the shock speed zero, at  $\tau_e$ . Since expansion shocks do not approach, Section 4.1, after point (e), the result is a constant state  $\eta_L$  on the left, then expansion shocks down to constant state to  $\eta_{\text{graze}}$ , followed by other expansion shocks down to constant state  $\eta_R$ , Figure 6.3.3(e). We have used expansion shocks to show that the constant  $\eta_{\text{graze}}$  persists. Increasing the number of expansion shocks will yield entropy-satisfying rarefactions in the limit, justifying the constant state  $\eta_{\text{graze}}$  from the continuum case in Figure 6.1.2.

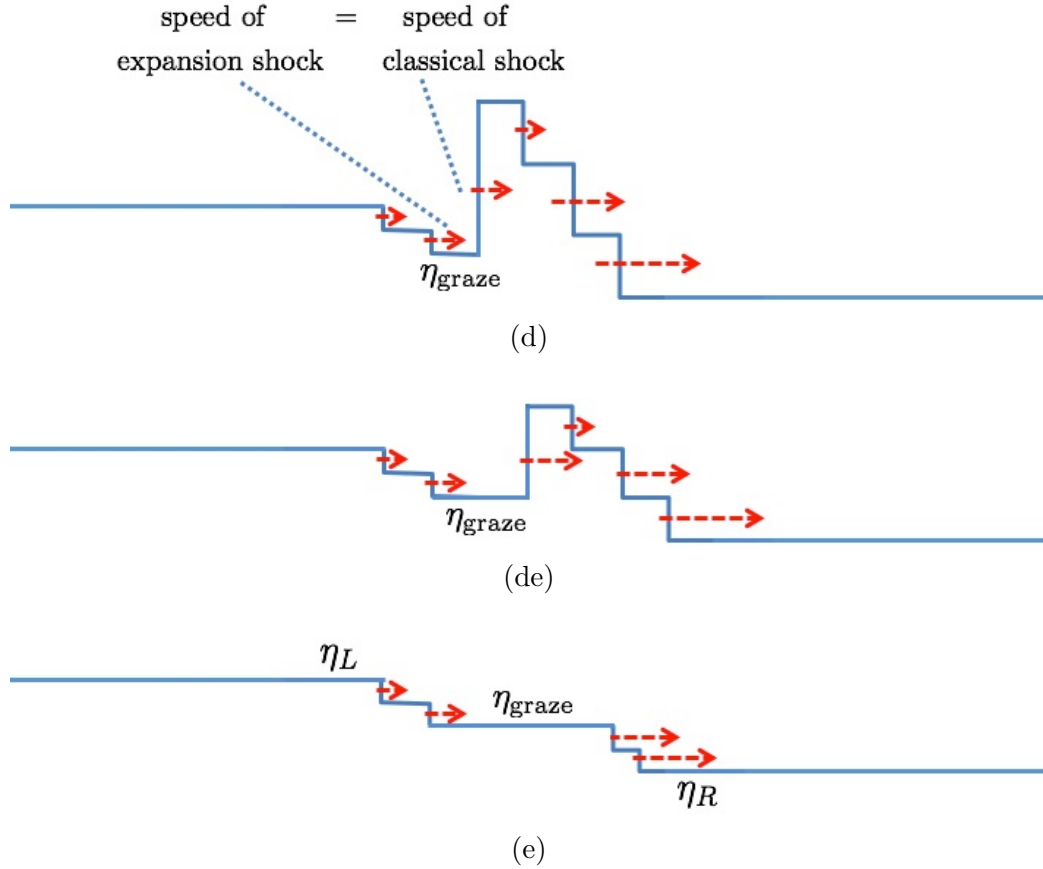


Figure 6.3.3: Expansion shock justification of constant state  $\eta_{\text{graze}}$ .

## 6.4 Solution After Constant $\eta_{\text{graze}}$ Region Emerges

The shock between  $\eta_{\text{graze}}$  and the rarefaction on the right advances forward until point (e) in Figure 6.1.2. Here,  $\eta$  within the rarefaction on the right equals  $\eta_{\text{graze}}$ , so the shock strength diminishes to zero. Point (e) also corresponds to the time,  $\tau_e = 30.1$ , where the faster characteristic, shown in red, becomes parallel to the resulting shock; the faster characteristic and the forward shock are both determined by the upper flux curve.

After  $\tau_e$ , we examine the solution resulting from the entire finite initial plume, Figure 6.1.1(a), and combine the attractive wave dynamics generated by the initial condition (6.1.1) with the resulting shock emanating from  $\xi = -26$  and the rarefaction centered at  $\xi = 10$ . To the left of this shock,  $\eta = 0$ , and to the right of this rarefaction,  $\eta = 0$ , corresponding to a brine-filled aquifer outside of the initial plume extent. Hence, moving from left to right at  $\tau_e$ , we have a constant region - shock - constant region - rarefaction - constant region - rarefaction - constant region - rarefaction - constant region:

$$\eta(\xi, \tau_e) = \begin{cases} 0, & \xi \lesssim -4.9, \\ \eta_L, & -4.9 < \xi \lesssim 4.7, \\ -0.0217\xi + 0.4024, & 4.7 < \xi \lesssim 7.2, \\ \eta_{\text{graze}} \approx 0.2458, & 7.2 < \xi \lesssim 9.7, \\ -0.0277\xi + 0.5140, & 9.7 < \xi \lesssim 11.3, \\ \eta_R, & 11.3 < \xi \lesssim 20.8, \\ -0.0277\xi + 0.7769, & 20.8 < \xi \lesssim 28.1, \\ 0, & \xi > 28.1. \end{cases} \quad (6.4.1)$$

The three rarefactions cannot approach, as shown in Chapter 3. After  $\tau_e$ , the compact support,  $\eta = 0$ , to the left of the plume drives the solution, and the resulting forward shock eventually interacts with the remnants of the non-centered rarefaction from  $\eta_L$  down to  $\eta_{\text{graze}}$ , resulting in a faster forward shock; this analytic solution is shown in Figure 6.4.1. The shock continues to gain speed as it interacts with the constant state  $\eta_{\text{graze}}$ , then the rarefaction from  $\eta_{\text{graze}}$  down to  $\eta_R$ , the constant state  $\eta_R$ , and finally the rarefaction from  $\eta_R$  down to  $\eta = 0$ , shown in blue and purple in Figure 6.4.1. The shock persists until it reaches the characteristic in the right-most rarefaction that corresponds to  $\eta = 0$ . After this point,  $\eta = 0$  throughout the aquifer, and the plume is completely trapped within pore space. For this example, we determined that the final interaction time is  $\tau_{\text{end}} = 168.45$  at a final interaction position of  $\xi_{\text{final}} = 111.07$ , shown as a blue star in Figure 6.4.1.



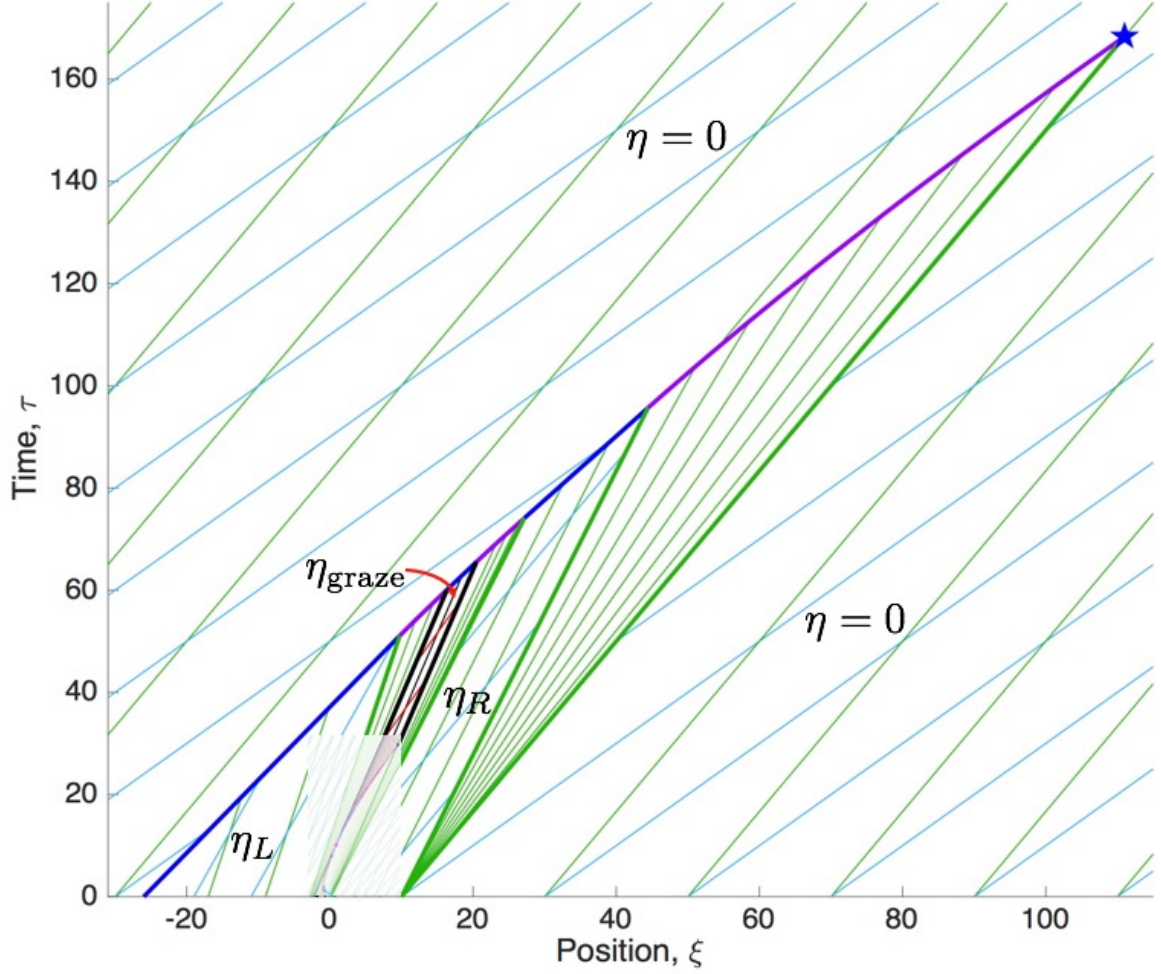


Figure 6.4.1: Analytic solution of initial condition that is completely trapped as residual bubbles after a finite time,  $\tau_{\text{end}} = 168.45$ , and at a finite position,  $\xi_{\text{final}} = 111.07$ , the blue star. Here,  $\mathcal{M} = 1$ ,  $\varepsilon = 0.4$ , and the plume has  $\eta_L = 0.3$ ,  $\eta_{\text{graze}} \approx 0.25$ , and  $\eta_R = 0.2$ , with  $\eta = 0$  in the rest of the aquifer.

## 6.5 Results with Dimensional Parameters

We now translate the non-dimensional analytic results from Section 6.4 back to physical quantities. In this modeling example, we solved (2.4.2) throughout the characteristic plane for the initial plume given in Figure 6.1.1(a) to find that the final interaction time was  $\tau_{\text{end}} = 168.45$  at a final interaction position of  $\xi_{\text{final}} = 111.07$ . After this point, there is no more plume migration, as the entire volume of  $\text{CO}_2$  has been deposited as droplets within the pore space.



To obtain estimates of the finite migration time and distance of the injected plume in Figure 6.1.1(a), we assume parameter values estimated by geotechnical data given in [17, 31, 33]:  $\phi = 0.15$ ,  $\Delta\rho = 300 \frac{\text{kilograms}}{\text{meter}^3}$ , and  $k = 0.5$  darcy  $\approx 4.93 \times 10^{-13}$  square meters. We consider an aquifer where the mobility of the two fluids is equal,  $\mathcal{M} = 1$ , and we assume that the aquifer has  $S_{cr} = S_{br} \approx 0.285$ . Consequently,  $\varepsilon = 0.4$  is the trapping parameter,  $k_{rc}$  is taken as 0.37 [5], and  $\mu_c = 2 \times 10^{-3} \frac{\text{kilograms}}{\text{m s}}$  [12]. An appropriate length scale for this model is the initial lateral extent of the plume, assumed to be 1000 meters, so  $L \approx 27.8$  meters, based on the initial extent of  $\xi = 36$  in Figure 6.1.1(a). The Viking Formation is an aquifer in western Canada that is 30 meters thick [33], but carbon sequestration projects also occur in formations with  $H > 300$  meters [31]. In this modeling exercise,  $\theta = 1.5^\circ$  [17]. The units given guarantee that  $\tau$  is dimensionless.

It follows from (2.2.4) that  $\kappa_1 \approx 4.17 \times 10^{-6}$  meters per second. Hence, from (2.3.1), we find that the plume is completely trapped as bubbles at time

$$\tau_{\text{end}} = 168.45 \quad \implies \quad t_{\text{end}} \approx 1358 \text{ years} . \quad (6.5.1)$$

In Figure 6.1.1(a), we see that the initial plume spanned from  $\xi = -26$  to  $\xi = 10$ , with compact support,  $\eta = 0$ , outside of that region of the aquifer. The analytic results in Figure 6.4.1 indicate the final migration position is  $\xi_{\text{final}} = 111.07$ ; hence, the residual surface has a lateral extent of  $\xi_{\text{end}} = 137.07$  underground. From (2.3.1), it follows that

$$\xi_{\text{end}} = 137.07 \quad \implies \quad x_{\text{end}} \approx 3808 \text{ meters} . \quad (6.5.2)$$

Hence, a plume with initial geometry (6.1.1),  $\eta_0 \in L^1(\mathbb{R}) \cap BV(\mathbb{R})$ , and aquifer parameters subject to (2.4.2) is completely residually trapped in a finite time and after a finite distance. The plume, which was originally one kilometer across like a crossword, displaced the in situ brine and left bubbles over a span of almost four kilometers within the subsurface rock matrix of the aquifer.

---

Exact Numerical Solutions

---

In this chapter, we present results from an implementation of the wave-front tracking method. We developed a numerical scheme to capture changing plume shape during migration, and the annotated MATLAB code that we wrote to obtain solutions and figures in this chapter is included in Appendix B.2. The code yields wave-front tracking solutions for any general initial plume configuration; for demonstrative purposes, we consider one initial condition for the remainder of this chapter.

## 7.1 Wave-front Tracking Algorithm

In this section, we derive exact wave-front tracking solutions for a specific initial plume geometry, shown in Figure 7.1.1(a). To run the MATLAB code that we developed, the user decides how many middle plume height values within the initial plume will be used to construct approximations for the initial condition; as shown in Figure 7.1.1(b), we approximate the smooth initial plume in this section with seven  $\eta$  values that are evenly-spaced along the initial lateral extent of the plume.

To implement the wave-front tracking method, a piecewise constant approximation of the initial condition is constructed, as in Figure 7.1.1(c). At each jump discontinuity, the resulting Riemann problem is solved; resulting rarefaction fans are approximated by expansion shocks. All shock speeds are well-defined on the dual flux curves, as shown in Figures 7.1.2 and 7.1.3. The speed of a forward compression shock is determined by the upper flux curve, Figure 7.1.2(a), because  $\eta_\tau < 0$  across the shock which implies  $\sigma = 1$ . The speed of a backward compression shock is

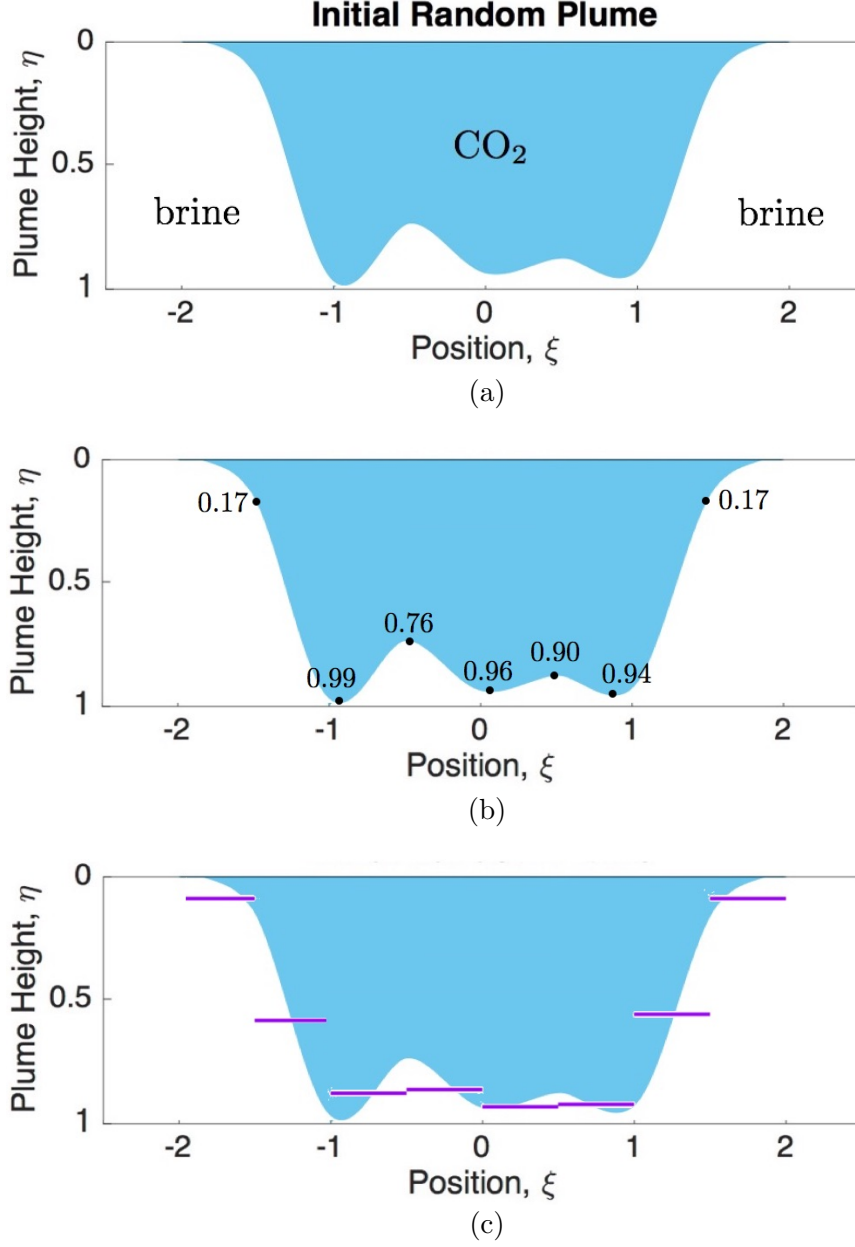


Figure 7.1.1: (a) Initial condition  $\eta_0 \in L^1(\mathbb{R}) \cap BV(\mathbb{R})$ , (b) seven middle  $\eta$  values within initial plume, and (c) piecewise constant approximation.

determined by the lower flux curve, Figure 7.1.2(b), because  $\eta_\tau > 0$  across the shock which implies  $\sigma = 1 - \varepsilon$ . Correspondingly, because  $\eta_\tau > 0$  across a forward expansion shock, the speed is determined by the lower flux curve, Figure 7.1.3(a), and the speed of a backward expansion shock is determined by the upper flux curve, Figure 7.1.3(b), since  $\eta_\tau < 0$  across

the shock. Throughout this chapter, the colors of the wave-front solutions in the characteristic plane will correspond to the colors in Figures 7.1.2 and 7.1.3: forward compression shocks are blue, backward compression shocks are pink, forward expansion shocks are grey, and backward expansion shocks are orange.

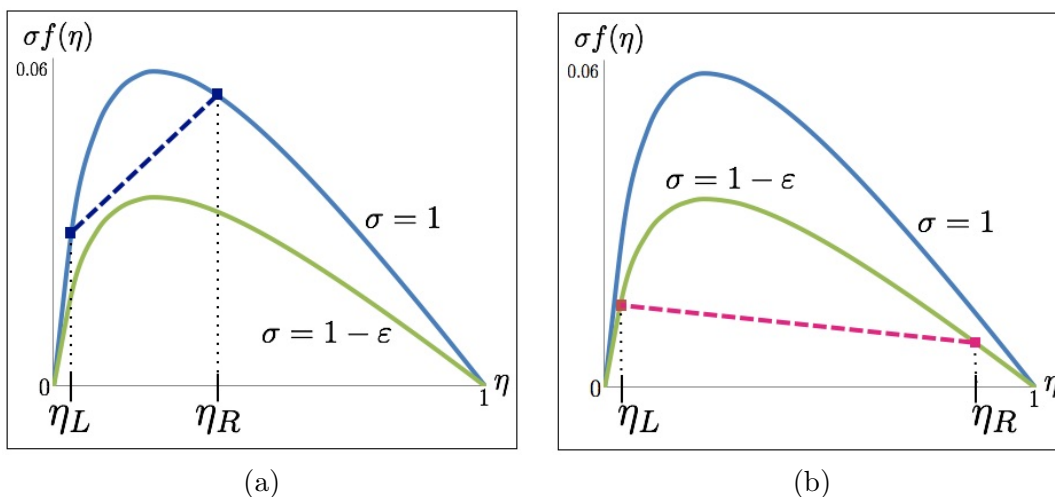


Figure 7.1.2: Compression shocks have  $\eta_L < \eta_R$ . (a) Speed of forward compression shock determined by upper flux curve. (b) Speed of backward compression shock determined by lower flux curve.

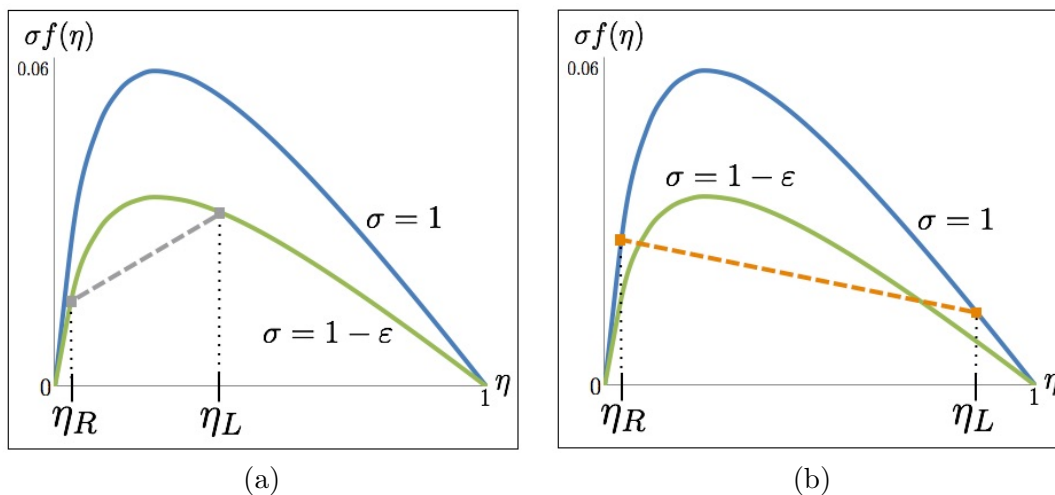


Figure 7.1.3: Expansion shocks have  $\eta_L > \eta_R$ . (a) Speed of forward expansion shock determined by lower flux curve. (b) Speed of backward expansion shock found on upper flux curve.

To initiate the algorithm for this example, the positions of the initial shock wave-fronts are determined in the characteristic plane. For increasing position  $\xi$  in Figure 7.1.4(a) and (b), there are two forward shocks, then five backward shocks (three of which are expansion shocks), then two forward expansion shocks. On the left side of any plume with compact support, there will always be a forward classical shock because the discontinuity at this point is always a jump

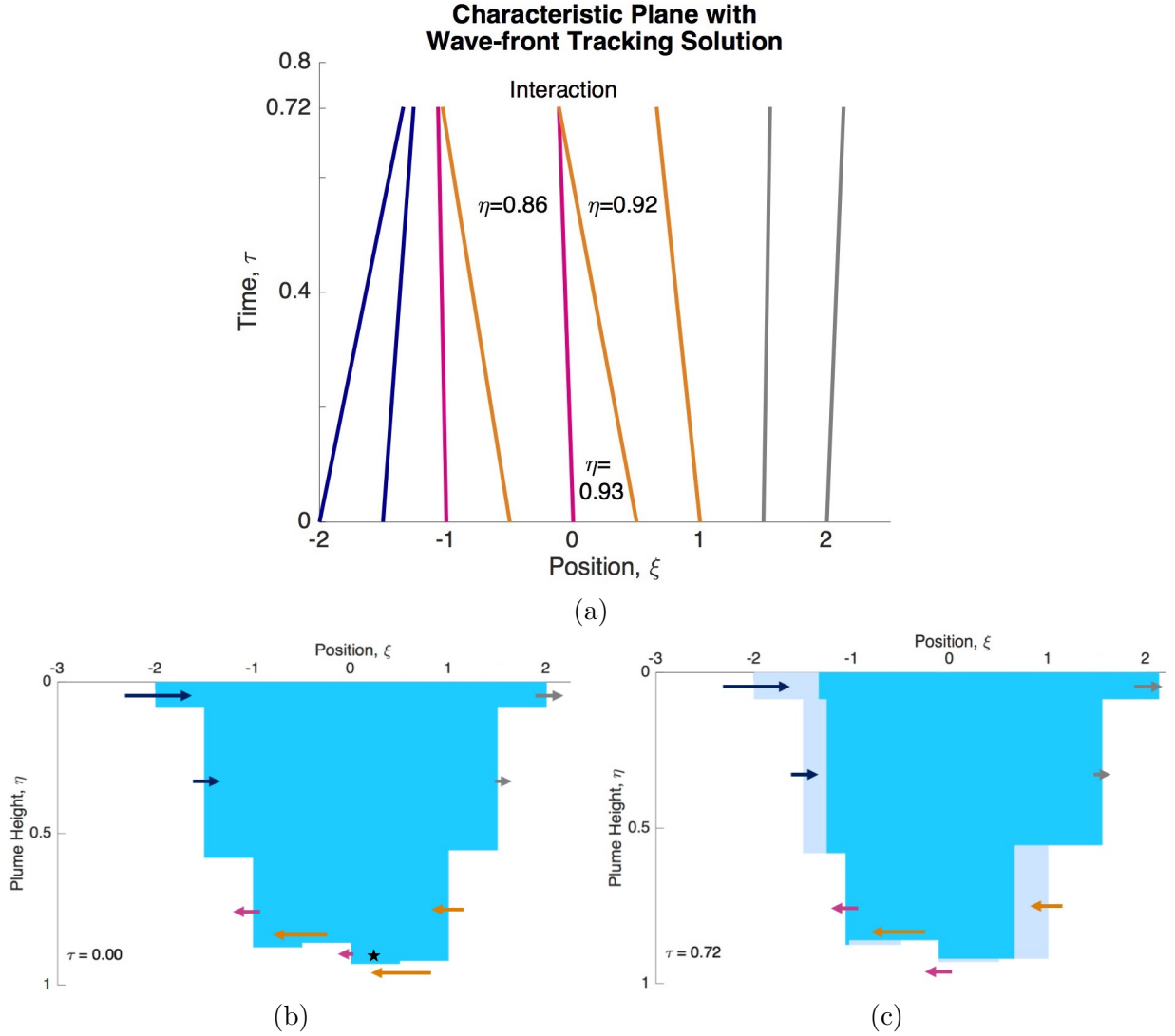


Figure 7.1.4: Exact wave-front solutions of initial Riemann problems up to the first shock collision in (a) characteristic plane and (b) solution space, where shocks are shown as vertical interfaces. In (b) and (c), arrows indicate directions and magnitudes of propagating shocks. (c) At this interaction time,  $\tau = 0.72$ , an orange backward expansion shock collides with a pink classical backward shock and eliminates the solution state  $\eta = 0.93$ , the black star in (b).

*up* from  $\eta = 0$  to any value of  $\eta$  within the plume. Similarly, the right-most shock will always be a forward expansion shock from any  $\eta$  value in the plume *down* to  $\eta = 0$  outside of the plume.

The initial wave-fronts propagate until two adjacent shocks collide at the first interaction time, labeled in Figure 7.1.4(a). At this point, the middle state in common with both incoming shock waves,  $\eta = 0.93$  (indicated by the black star in Figure 7.1.4(b)), is eliminated. The resulting shock emanating from this first point of interaction is a backward classical shock from  $\eta = 0.86$  up to  $\eta = 0.92$ ; all other shocks in the characteristic plane maintain their initial speeds. The entropy-satisfying classical compressive shock waves and the expansion shock waves propagate, and, as adjacent shocks interact, those resulting shock waves are also tracked throughout the characteristic plane, as shown in Figure 7.1.5(a). In that figure, it is apparent that the entire left

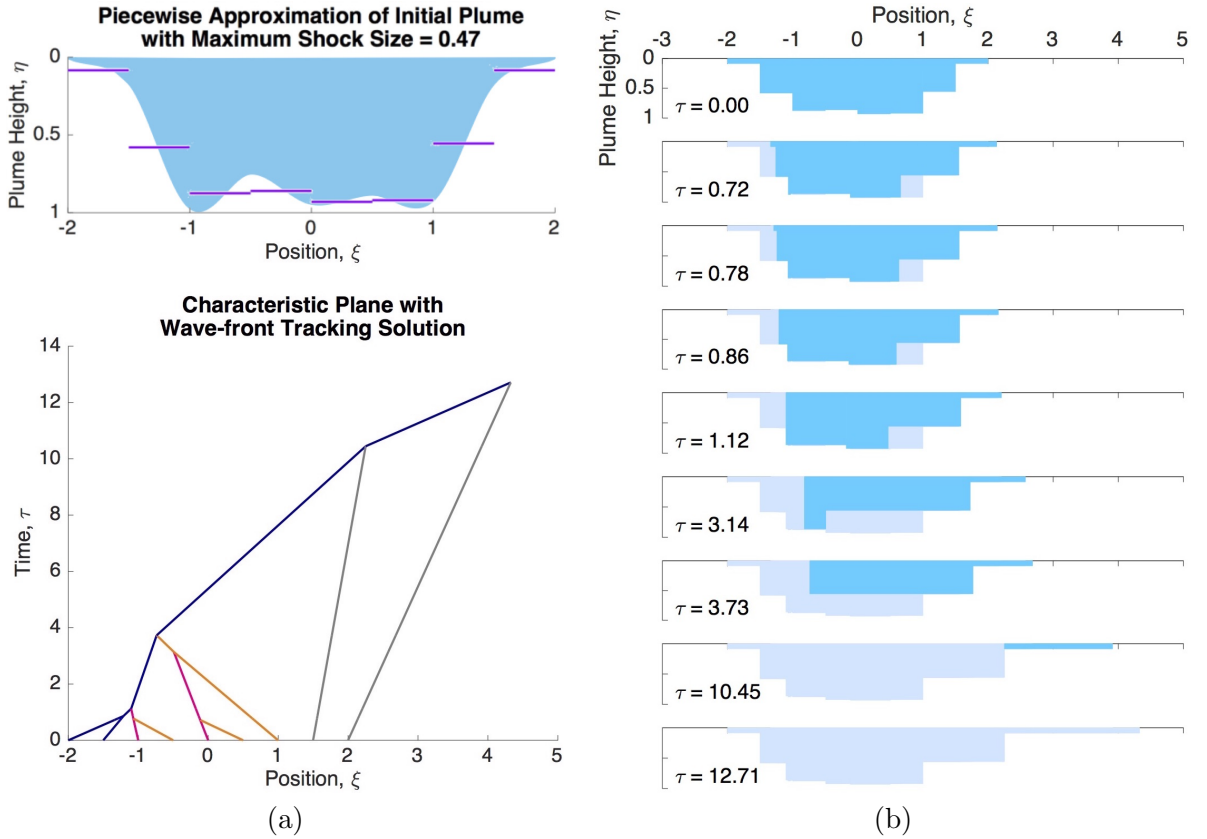


Figure 7.1.5: (a) Initial plume approximated by piecewise constant states (top) such that the maximum jump up (compressive shock) and jump down (expansion shock) is  $h_{\max} = 0.47$ , and (bottom) the resulting exact wave-front tracking solution for  $\varepsilon = 0.8$  in characteristic space. (b) Corresponding migrating plume and residual surface in solution space at interaction times.

wave-front is always a classical forward shock [28]; the final forward shock on the left interacts with the right-most expansion shock at a finite final interaction time and position. At this point, all constant middle states within the plume have been eliminated, and after this time, the solution is  $\eta = 0$  throughout the characteristic plane.

The evolution of the plume in characteristic space, Figure 7.1.5(a), corresponds to a time progression of the plume migration underground, Figure 7.1.5(b). For  $\varepsilon = 0.8$  and  $\mathcal{M} = 1$ , this schematic has numerical solutions for the plume shape at interaction times, where two shocks collide in the characteristic plane. In engineering practice, the value of the mobility ratio  $\mathcal{M}$  is larger (usually between 10 and 20), and the impact of the trapping parameter  $\varepsilon$  is even smaller [17, 28]. In Figure 7.1.5(b), we visualize plume migration, which is generally to the right due to a combination of groundwater flow and aquifer slope. The mobile  $\text{CO}_2$  invades new pore space and leaves trapped  $\text{CO}_2$  in its wake. The shape of the migrating plume at each interaction time is simulated in Figure 7.1.5(b), with mobile  $\text{CO}_2$  within the plume shown in dark blue, the residual surface region containing trapped  $\text{CO}_2$  drawn in light blue, and brine in white.

## 7.2 Trapping Comparison of Wave-front Tracking Solutions

The wave-front tracking results obtained in Section 7.1 correspond to plume migration in an aquifer with a trapping parameter of  $\varepsilon = 0.8$ . The initial piecewise constant plume shape and final residual surface of trapped bubbles from Figure 7.1.5(b) are superimposed in Figure 7.2.1. The scant residual surface outside of the initial plume location indicates the plume did not migrate very far, and most of the droplets of  $\text{CO}_2$  were deposited in the initial plume location.

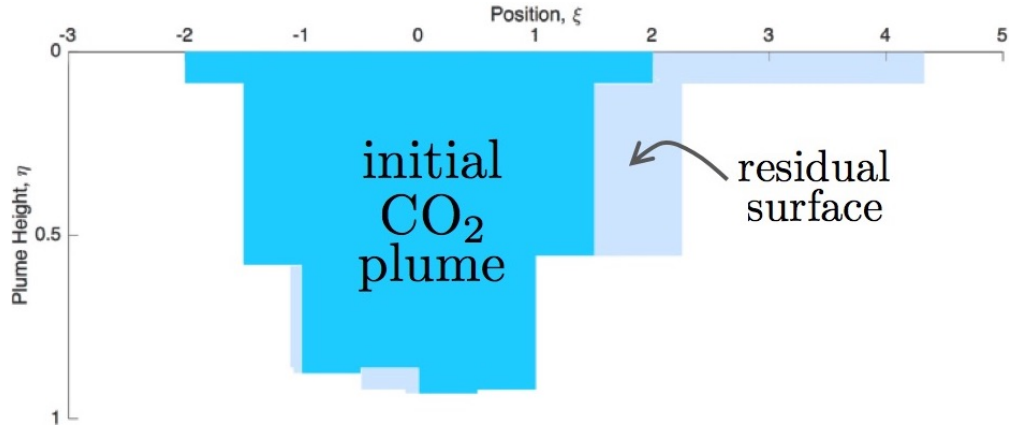


Figure 7.2.1: Initial plume and resulting residual surface for trapping parameter  $\varepsilon = 0.8$  and maximum shock size  $= 0.47$ .

Varying the trapping parameter in simulations will alter the final migration distances and times of the plume. In this section, we obtain results when the trapping parameter,  $\varepsilon$ , is decreased, meaning that less of the pore space is available to trap  $\text{CO}_2$ .

A decrease in the trapping parameter,  $\varepsilon$ , implies that  $\sigma = 1 - \varepsilon$  increases. With less trapping, the lower flux curve increases in height, and the magnitudes of the speeds of backward compressive shocks and forward expansion shocks increase, as those shock speeds are determined by the lower flux curve. The speeds of forward compressive shocks and backward expansion shocks are unchanged, because those shocks are determined on the upper flux curve, which is not dependent on the amount of trapping.

For this trapping comparison, we track the wave-fronts when  $\varepsilon = 0.4$  and assume the same initial condition approximated the same way as in Section 7.1 when  $\varepsilon = 0.8$ . The piecewise constant plume in Figure 7.2.2(a) is the same as the initial condition in Figure 7.1.4(b); the horizontal scale is the only difference between those figures. In Figure 7.2.2(a), the arrows corresponding to the forward compressive shocks and backward expansion shocks are the same as in Figure 7.1.4(b); however, when the trapping parameter is decreased from  $\varepsilon = 0.8$ , as

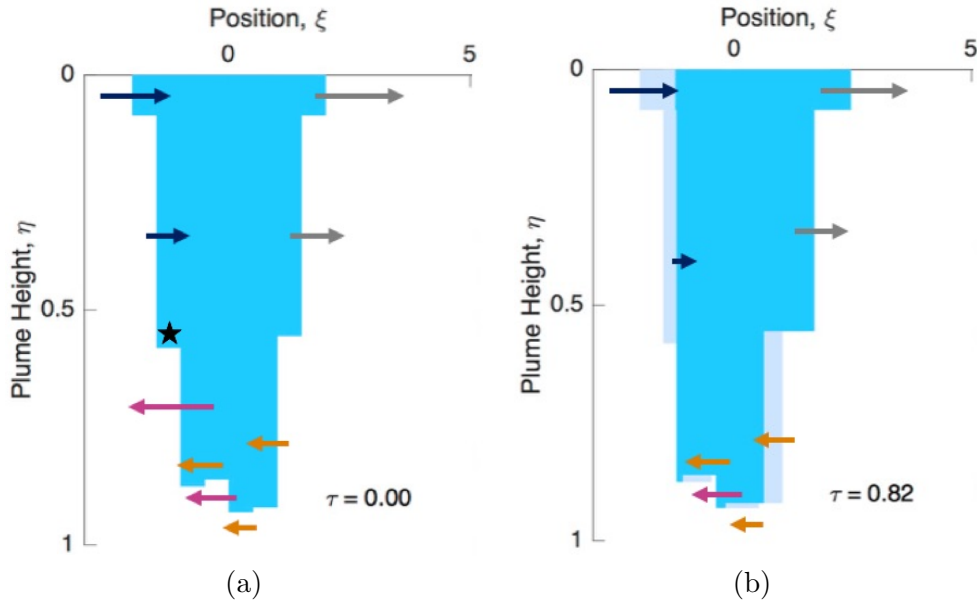


Figure 7.2.2: Trapping parameter is decreased to  $\varepsilon = 0.4$ . (a) Initial shock speeds and directions for piecewise constant plume approximation with maximum shock size = 0.47. (b) Wave-front propagation of plume migration after one interaction, when the constant state indicated by the black star in (a) is eliminated.



in the previous section, to  $\varepsilon = 0.4$ , the forward expansion shocks, in grey, are faster to the right, and the backward compressive shocks, in pink, are faster to the left. The first interaction between neighboring wave-fronts occurs at a different location, indicated by a black star, for this different trapping parameter; in Figure 7.2.2(b), the first interaction occurs when the second- and third-from-the-left wave-fronts interact, whereas in Figure 7.1.4(b), the first interaction occurs when the fifth- and sixth-from-the-left wave-fronts interact. When  $\varepsilon = 0.4$ , wave-fronts are tracked in characteristic space, Figure 7.2.3(a), and solution space, Figure 7.2.3(b), until the final interaction point, at which point the plume is fully sequestered.

We consider the same approximation of the same initial condition to deduce impact of changes in trapping parameter,  $\varepsilon$ , on the final plume migration time and distance. The final interaction point is defined as the time,  $\tau$ , and position,  $\xi$ , when the last two remaining wave-fronts collide; beyond this point,  $\eta = 0$  throughout the aquifer, indicating that the plume is completely

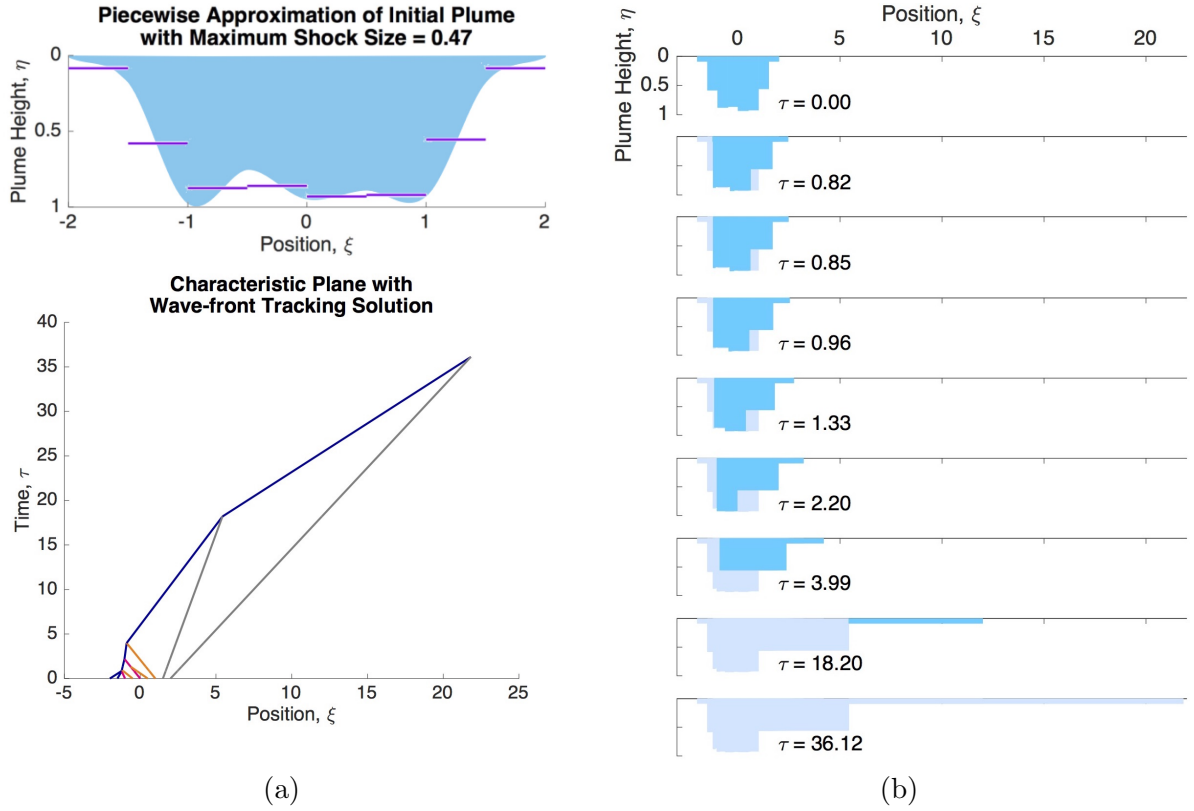


Figure 7.2.3: (a) (top) Initial plume approximated as in Section 7.1, and (bottom) the resulting exact wave-front tracking solution for  $\varepsilon = 0.4$  in characteristic space. (b) Corresponding migrating plume and exact residual surface for  $\varepsilon = 0.4$  in solution space.

residually trapped. When  $\varepsilon = 0.8$ , the final interaction point is  $(\tau, \xi) \approx (12.71, 4.33)$  from Figure 7.1.5. When  $\varepsilon = 0.4$ , the final interaction is  $(\tau, \xi) \approx (36.12, 21.83)$  from Figure 7.2.3. A decrease in trapping leads to an increase in final migration distance, as shown in Figure 7.2.4.

We translate the dimensionless results for this trapping comparison to dimensional time and length. Parameters for the porous aquifer and fluids are taken as in Section 6.5 [5, 12, 17, 31, 33]. For trapping parameter  $\varepsilon = 0.8$ , it follows that the final interaction point is  $t \approx 239$  years and  $x \approx 1.6$  kilometers, whereas, when trapping is decreased to  $\varepsilon = 0.4$ , the final interaction point is  $t \approx 2620$  years and  $x \approx 6.0$  kilometers. Hence, when pore space available to trap  $\text{CO}_2$  is more limited, the trapping parameter decreases, and results from this section show that plume migration continues over a longer time and distance.

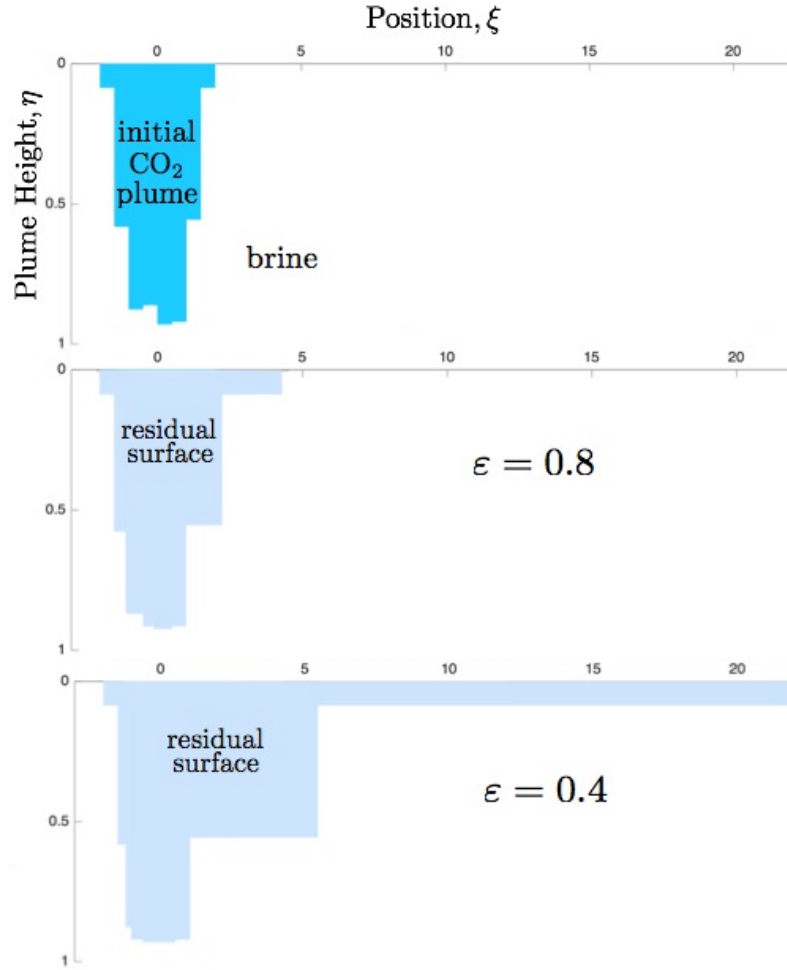


Figure 7.2.4: Residual surfaces when  $\varepsilon = 0.8$  (more trapping) and  $\varepsilon = 0.4$  (less trapping).

### 7.3 Sequence of Numerical Wave-front Tracking Solutions

In this section, we illustrate the construction of a sequence of exact wave-front tracking solutions resulting from a sequence of piecewise constant approximations to an initial condition with bounded variation. The maximum size of compression shocks (jumps up) and expansion shocks (jumps down) in the piecewise constant approximation of the initial condition in Figure 7.1.5 was  $h_{\max} = 0.47$ . In the limit as  $h_{\max} \rightarrow 0$ , an entropy-satisfying solution with rarefactions would be obtained. In Figures 7.3.1-7.3.4, we approximate the initial condition with an increasing number of piecewise constant states thereby decreasing  $h_{\max}$ , the maximum size of classical and expansion shocks. We use the sequence of approximations of the initial condition to construct a sequence of wave-front tracking solutions to the Cauchy problem for five decreasing values

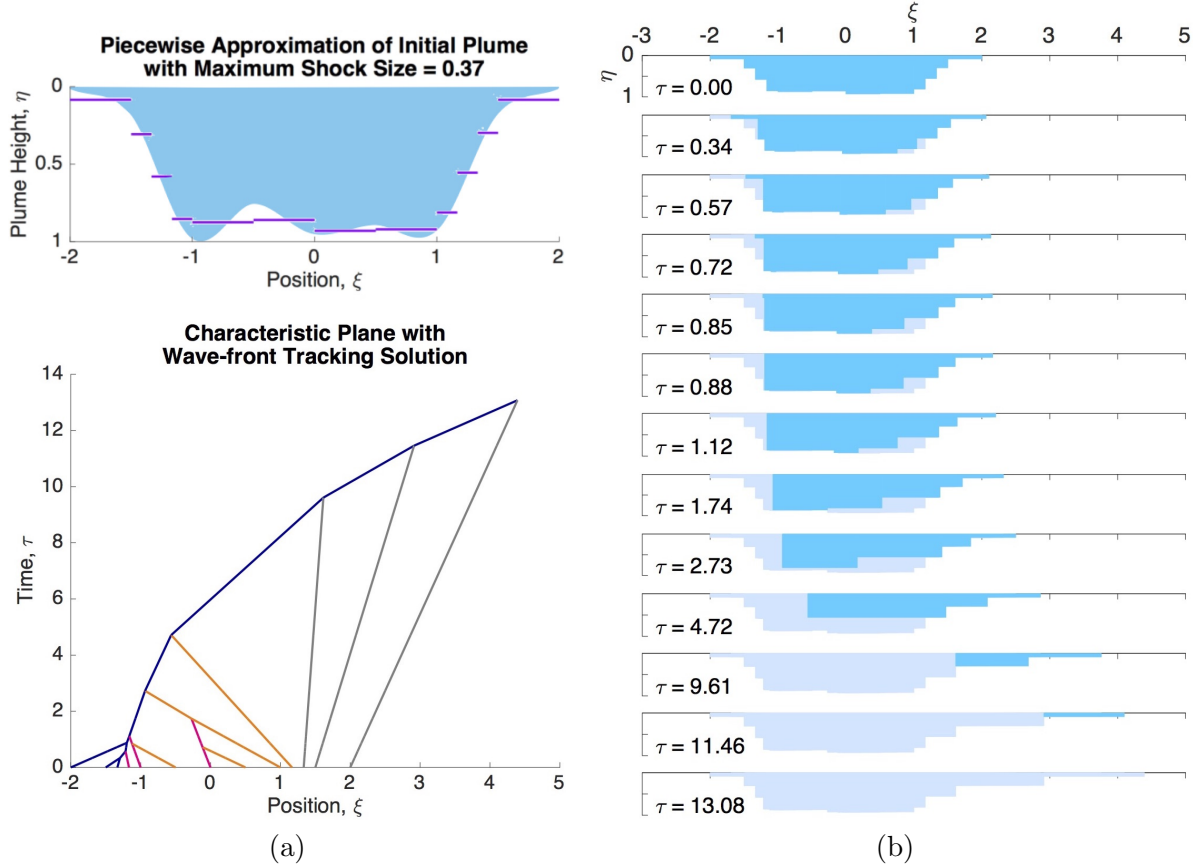


Figure 7.3.1: (a) Initial approximation with  $h_{\max} = 0.37$  and resulting exact wave-front tracking solution. (b) The plume migrates until the final interaction time,  $\tau_{\text{end}} = 13.08$ , after which point, a residual surface is all that remains.

of  $h_{\max}$ . With  $h_{\max} = 0.37$  in Figure 7.3.1, larger jumps are approximated by an increased number of smaller shocks, slightly altering interaction times and positions. We further refine the initial approximation of the given CO<sub>2</sub> plume by decreasing the allowable jump between  $\eta$  values of adjacent constant states to  $h_{\max} = 0.27$  in Figure 7.3.2, then down to  $h_{\max} = 0.17$  in Figure 7.3.3, and finally, in Figure 7.3.4(a), the maximum size of compression and expansion shocks in the piecewise constant approximation of the initial condition is set at  $h_{\max} = 0.07$ ; in Figure 7.3.4(b), wave-fronts are tracked until the first interaction point, at which time the constant state indicated by a black star in Figure 7.3.4(a), is eliminated. In Figures 7.3.4(c) and 7.3.5, wave-fronts are tracked until the final interaction point.

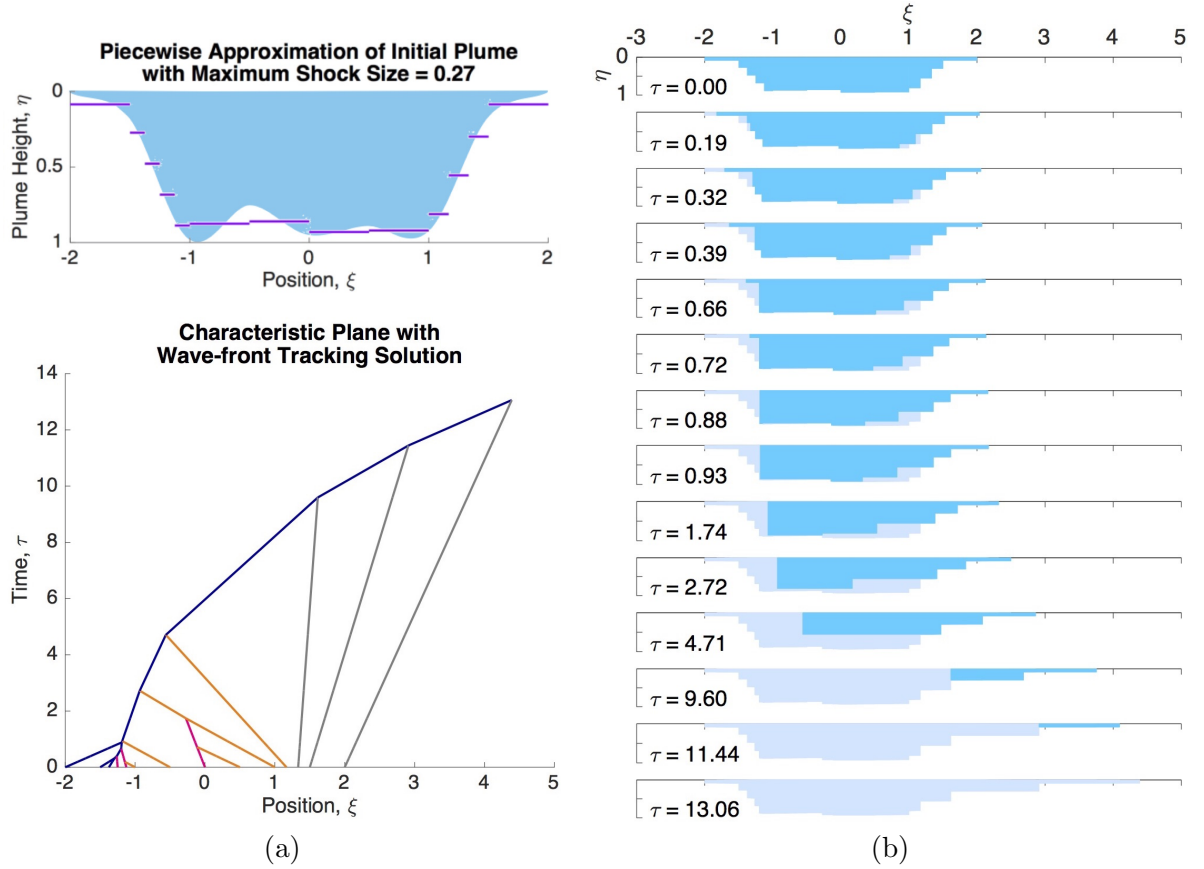


Figure 7.3.2: Results of numerical implementation of the wave-front tracking method for an approximation of the initial condition with  $h_{\max} = 0.27$ .

In this chapter, we considered the wave-front tracking solutions of the Cauchy problem for (2.4.2), a nonlinear conservation law with discontinuous dual flux functions, and initial  $\text{CO}_2$  plume in Figure 7.1.1(a). If  $h_{\max}$  is allowed to vary and decrease, we see the result of Helly's Compactness Theorem A.1.1: a subsequence of a sequence of solutions, such as those in Figures 7.3.1-7.3.5, will converge to an entropy-satisfying solution, as proven in Chapter 5.

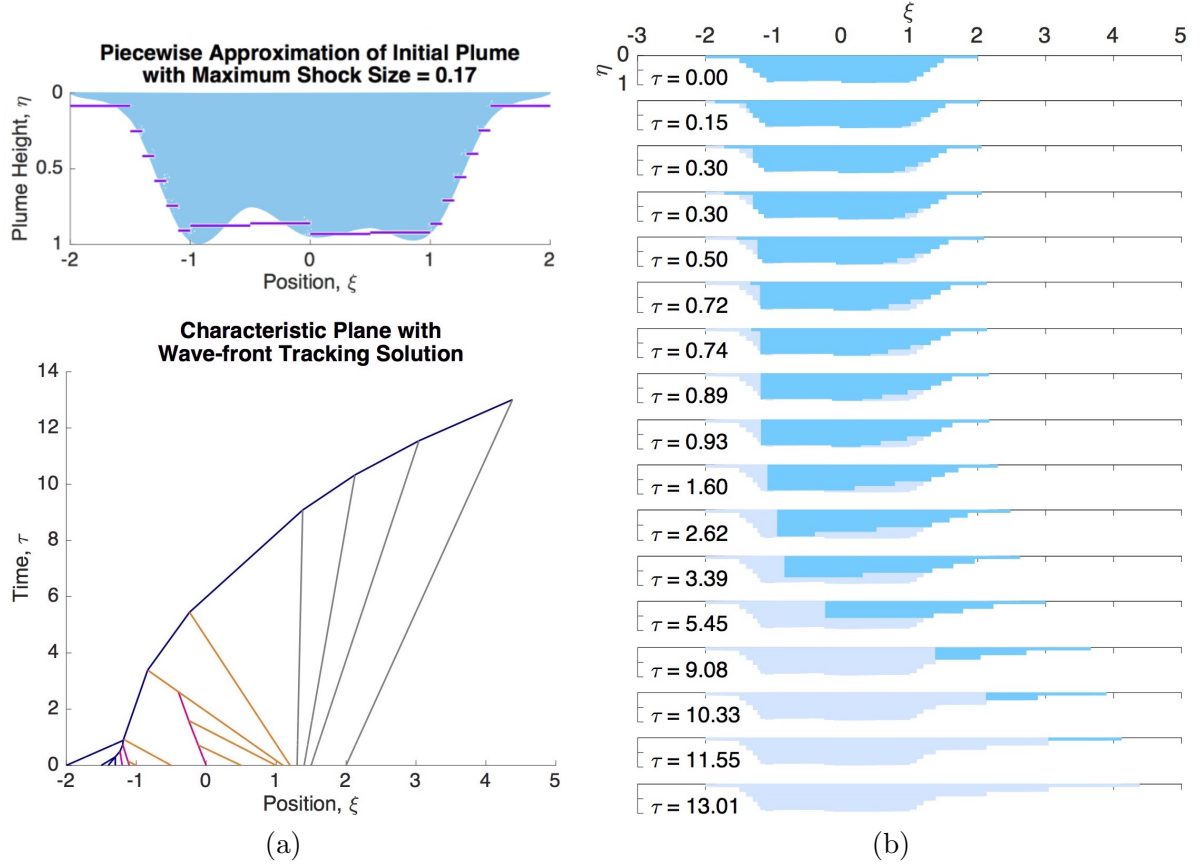


Figure 7.3.3: Results of numerical implementation of the wave-front tracking method for an approximation of the initial condition with  $h_{\max} = 0.17$ .

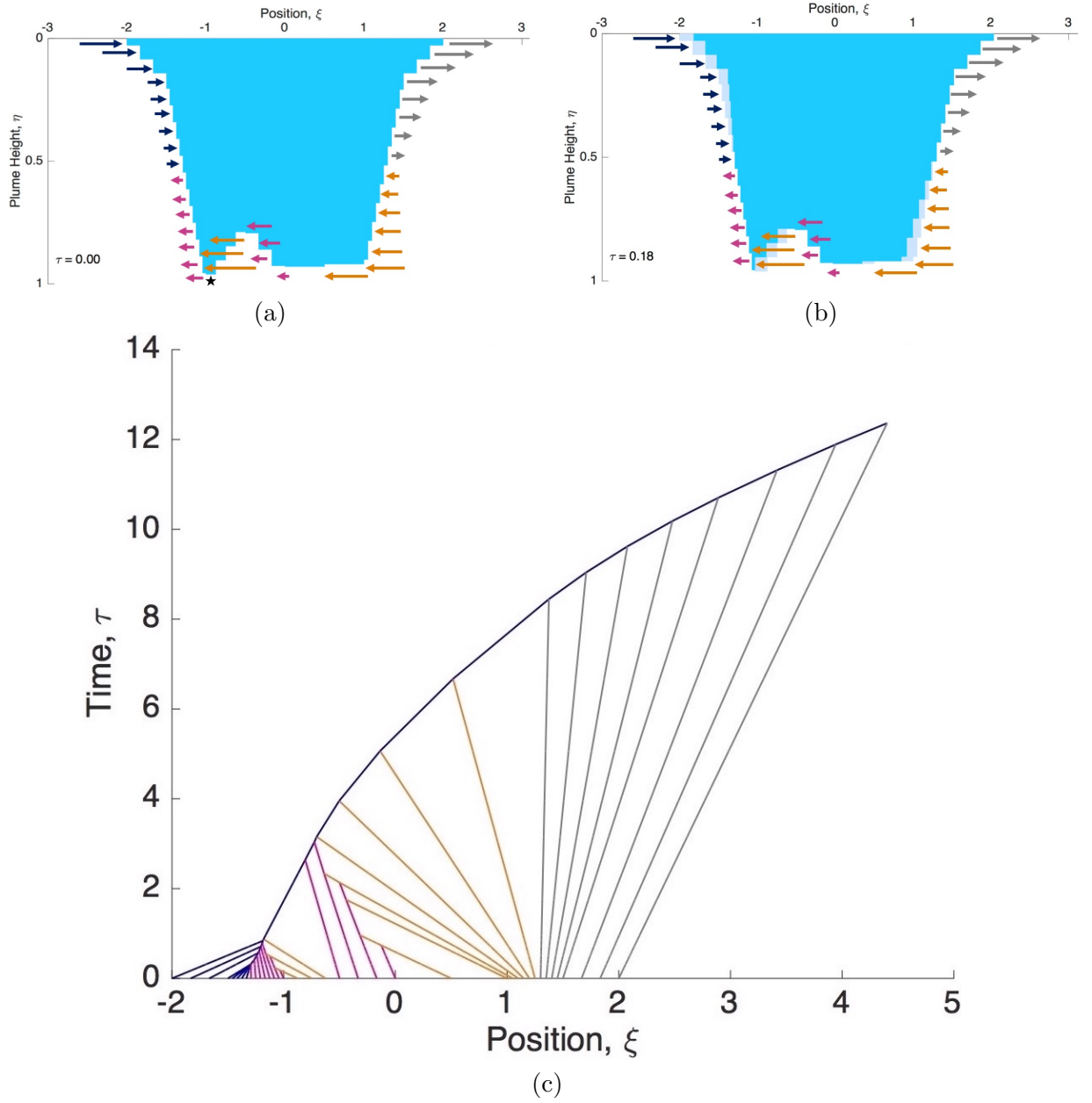


Figure 7.3.4: Initial plume is approximated with 37 constant states due to the restriction,  $h_{\text{max}} = 0.07$ , on maximum sizes of jumps up (classical shocks) and down (expansion shocks). (a) Wave-fronts corresponding to 37 initial constant states and shock speeds and directions. (b) Plume location after one interaction. (c) Exact locations of the wave-fronts are tracked throughout the characteristic plane until final interaction point of  $\tau_{\text{end}} = 12.36$  and  $\xi_{\text{final}} = 4.40$ .

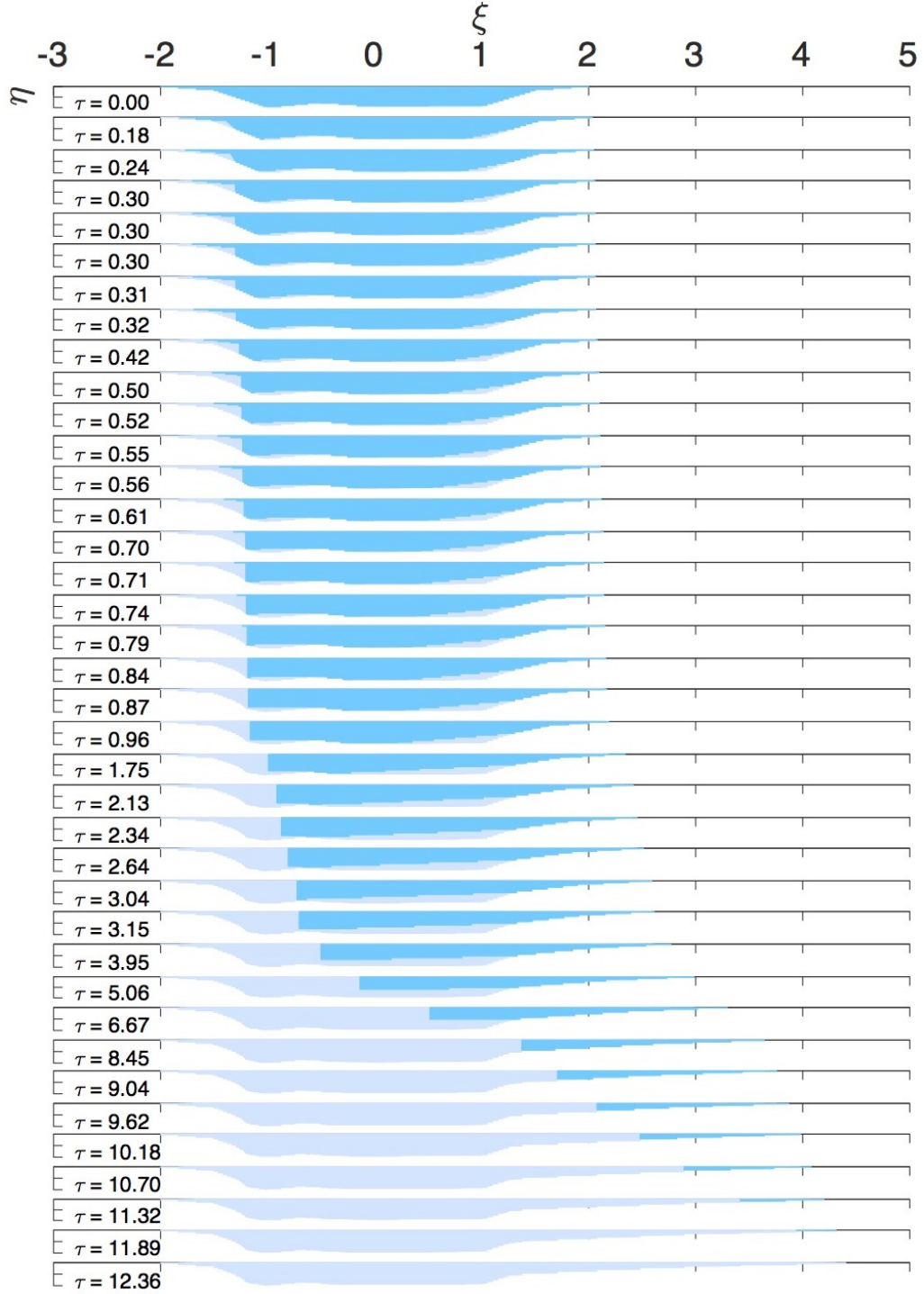


Figure 7.3.5: An exact wave-front tracking solution, for maximum allowable initial shock sizes of  $h_{\max} = 0.07$ , provides a visualization of plume migration at each interaction time. The mobile plume is blue, the residual surface of trapped bubbles is light blue, and the brine is white.

---

## Concluding Remarks

---

The dual flux model given by (2.4.1)-(2.4.3) and [17] captures underlying large-scale behavior of carbon dioxide ( $\text{CO}_2$ ) plume migration in porous media. In Chapter 2, we showed that the evolution of a gravity current with residual trapping can be modeled as a nonlinear conservation law given by

$$\eta_\tau + (\sigma f(\eta))_\xi = 0 ,$$

for fractional plume height  $\eta = \eta(\xi, \tau)$  at any position  $\xi$  and time  $\tau$  in a brine aquifer, with a discontinuous flux given by

$$\sigma f(\eta) = \sigma \frac{\eta(1-\eta)}{\eta(\mathcal{M}-1)+1} \quad \text{with} \quad \sigma = \begin{cases} 1-\varepsilon , & \eta_\tau > 0 , \\ 1 , & \eta_\tau < 0 , \end{cases}$$

for trapping parameter  $\varepsilon$  and mobility  $\mathcal{M}$ . Dual flux curves emerge in this model, giving rise to flux discontinuities. One flux describes the invasion of the  $\text{CO}_2$  plume into pore space, and the other captures the flow as the plume drains and leaves a residual surface of trapped  $\text{CO}_2$  droplets behind. The switch between the two flux functions is prescribed to occur at points where the height of the plume changes from increasing to decreasing in time.

During the analysis in Chapter 3 of this dissertation, we introduced a new construction with cross-hatch characteristics in regions of the characteristic plane where the solution is constant, and the characteristic speed depends on which flux is invoked. By including cross-hatch characteristics, we resolved ambiguous gaps in the characteristic plane of [17] related to regions of constant solution. The analytic solution of the example in Chapter 6 exhibits a shock curve on



which the shock speed becomes one of the characteristic speeds, thus risking loss of admissibility. Continuation of the solution depends on cross-hatch characteristics. Chapter 4 includes a detailed description of wave interactions, including some properties that do not occur in conventional scalar conservation laws, such as non-increasing total variation and non-increasing number of propagating waves.

The main result of this dissertation is Theorem 5.0.1. In Chapter 5, we proved the existence of an entropy solution of the Cauchy problem for any initial  $\text{CO}_2$  plume using wave-front tracking. In Chapter 7, we implemented a numerical construction of piecewise constant approximate solutions of the Cauchy problem using expansion shocks in place of rarefaction waves. We had to account for the dual fluxes carefully in order to establish that a subsequence of approximate solutions converges to an entropy solution of the Cauchy problem and thus complete the existence proof of Theorem 5.0.1.

A striking feature of this simple model is that, because of its dual flux curves, solutions can include the prediction that the entire  $\text{CO}_2$  plume is deposited as bubbles in a finite time. To prevent detrimental leakage from a sequestration site, plume migration must be stymied before the plume reaches natural and manmade fractures that exist along the cap rock [14, 19, 40, 44]. Residual trapping decreases the distances traversed by buoyant plumes [17], and final migration distances can be calculated, as in Chapters 6 and 7. Hence, the potential for leakage through a fractured cap rock diminishes if the distance between the injection site and known fracture is greater than the predicted migration distance from the model; the plume would be completely trapped before the advancing tip of the plume reached the conduit to the atmosphere.

Results from models that predict final migration distances of sequestered carbon dioxide are used within the legal realm of subsurface property rights [23]. The model analyzed throughout this dissertation neglected the dissolution of  $\text{CO}_2$  into brine and undulations in the cap rock, both of which decrease the amount of migrating  $\text{CO}_2$  [19, 21, 30]. Hence, the final migration times and distances obtained by this model may be overestimates when compared to solutions from a  $\text{CO}_2$  sequestration equation that incorporates other physics and geology. The model considered in this dissertation is just simple enough to capture the basic transport properties of the migration of the supercritical carbon dioxide plume.

This dissertation sparks future research in several directions. We conjecture that if a finite amount of  $\text{CO}_2$  is injected into the subsurface, the Cauchy problem (5.0.1) yields a solution where the plume is completely stored in finite time. Though the dual flux curves add complexity to this conjecture, the examples in Chapters 4, 6, and 7 have solutions where plume size diminishes to zero in finite time as bubbles become trapped in pore spaces. Progress was made

in this dissertation regarding a proof structure for this conjecture, as follows. Any compactly supported plume will have  $\eta = 0$  as a constant state outside of the initial lateral extent of the plume. Hence, on the right, there will always be a rarefaction from any value of  $\eta > 0$  within the plume down to  $\eta = 0$  outside of the plume; the right-most propagating characteristic in the rarefaction will have speed determined from the lower flux curve since  $0 < \eta^*$ . The left-most wave interaction will always be a shock up from  $\eta = 0$  to any value of  $\eta > 0$  within the plume; this classical forward shock speed is determined from the upper flux curve. From the wave interaction catalog in Chapter 4, we have shown that shock-rarefaction (Case A) or shock-shock (Case B) interactions always lead to an elimination of the constant middle state. The resulting shock (from 0 on the left up to any adjacent  $\eta$  on the right) would propagate until another interaction time, when the interaction would again eliminate a middle state. The iterative shock construction continues until the shock interacts with the leading characteristic of the final rarefaction. The positive shock speed will always be greater than the corresponding positive characteristic speed because of the dual flux curves. We conjecture that, for a plume with a given initial lateral extent, all resulting final interaction points are within the ideal envelope case in [17] corresponding to an aquifer completely filled with  $\text{CO}_2$  throughout its initial lateral extent. It remains to prove that any initial compactly supported  $\text{CO}_2$  plume with bounded variation will be deposited as bubbles in finite time when modeled by the considered conservation law.

While improvements have been made to the model considered throughout this dissertation, [7, 14, 15, 28, 32, 48], possible future work includes modifications of the model of [17]. The model has a problem if  $\eta(\xi, 0)$  has more than one turning point, since if there are two or more, then the plume is invading a region that already has  $\text{CO}_2$  bubbles. If the bubbles reconnect with the plume, the plume height would increase, thereby violating an assumption that the maximum plume height decreases as shown in Figure 2.3.1. To remedy this, a change could be made regarding the model assumption of constant saturations of each fluid along the advancing fronts of the plume so as to distinguish advancing fronts that are propagating into portions of the aquifer with existing  $\text{CO}_2$  deposition. Modifying the carbon sequestration model to capture plume invasion into a region that already has  $\text{CO}_2$  bubbles would impact the flux, and the result might be more than two flux functions.

Another direction for future work is the formulation of a uniqueness proof for the nonlinear conservation law with a dual flux (2.4.1)-(2.4.3). This stems from the existence argument that we proved in Chapter 5 of this dissertation. Though the general uniqueness proof for a scalar conservation law with convex flux is outlined in [3], this problem requires a nontrivial extension of the general case due to the dual flux curves.

## REFERENCES

- [1] Bear, J. (2000). Lecture 2: Extensions of Darcy's law. *Computer-mediated distance learning course on modeling groundwater flow and contaminant transport*, Haifa, Israel. Found at: [interpore.org/reference\\_material/mgfc-course/mgfc-darcyext.html](http://interpore.org/reference_material/mgfc-course/mgfc-darcyext.html).
- [2] Big Sky Carbon Sequestration Partnership. (2016). *Site Characterization*. Found at: [bigskyco2.org/kevin\\_dome\\_site\\_characterization](http://bigskyco2.org/kevin_dome_site_characterization).
- [3] Bressan, A. (1991). Global solutions of systems of conservation laws by wave-front tracking. *Mathematical Analysis and Applications*, 170, 414-432.
- [4] Bressan, A. (2000). *Hyperbolic systems of conservation laws: the one-dimensional Cauchy problem*. Oxford Lecture Series in Mathematics and its Applications, 20.
- [5] Burnside, N. & Naylor, M. (2014). Review and implications of relative permeability of CO<sub>2</sub>/brine systems and residual trapping of CO<sub>2</sub>. *International Journal of Greenhouse Gas Control*, 23, 1-11.
- [6] Carbon Capture & Sequestration Technologies MIT. (2015). *Sleipner Fact Sheet: Carbon Dioxide Capture and Storage Project*. Found at: [sequestration.mit.edu/tools/projects/sleipner.html](http://sequestration.mit.edu/tools/projects/sleipner.html).
- [7] Celia, M., Bachu, S., Nordbotten, J., & Bandilla, K. (2015). Status of CO<sub>2</sub> storage in deep saline aquifers with emphasis on modeling approaches and practical simulations. *Water Resources Research*, 51, 6846-6892.
- [8] Chen, G., Even, N., & Klingenberg, C. (2008). Hyperbolic conservation laws with discontinuous fluxes and hydrodynamic limit for particle systems. *Differential Equations*, 245, 3095-3126.
- [9] Colombo, R. (2004). Wave front tracking in systems of conservation laws. *Applications of Mathematics*, 6, 501-537.
- [10] Dafermos, C. (1972). Polygonal approximations of solutions of the initial value problem for a conservation law. *Mathematical Analysis and Applications*, 38, 33-41.

- [11] DiPerna, R. (1976). Global existence of solutions to nonlinear hyperbolic systems of conservation laws. *Differential Equations*, 20, 187-212.
- [12] Economides, M., Ehlig-Economides, C., Hill, D., & Zhu, D. (2012). *Petroleum production systems, 2nd edition*. Prentice Hall. 1.4.
- [13] Garavello, M. & Piccoli, B. (2006). *Traffic flow on networks: conservation laws models*. AIMS Series on Applied Mathematics, 1.
- [14] Golding, M., Neufeld, J., Hesse, M., & Huppert, H. (2011). Two-phase gravity currents in porous media. *Fluid Mechanics*, 678, 248-270.
- [15] Guo, B., Zheng, Z., Bandilla, K., Celia, M., & Stone, H. (2016). Flow regime analysis for geologic CO<sub>2</sub> sequestration and other subsurface fluid injections. *International Journal of Greenhouse Gas Control*, 53, 284-291.
- [16] Hayek, M., Mouche, E., & Mugler, C. (2009). Modeling vertical stratification of CO<sub>2</sub> injected into a deep layered aquifer. *Advances in Water Resources*, 32, 450-462.
- [17] Hesse, M., Orr, F., & Tchelepi, H. (2008). Gravity currents with residual trapping. *Fluid Mechanics*, 611, 35-60.
- [18] Hesse, M. & Woods, A. (2010). Buoyant dispersal of CO<sub>2</sub> during geological storage. *Geophysical Research Letters*, 37, L01403.
- [19] Huppert, H. & Neufeld, J. (2014). The fluid mechanics of carbon dioxide sequestration. *Annual Review of Fluid Mechanics*, 46, 255-272.
- [20] Intergovernmental Panel on Climate Change (2005). *IPCC Special Report on Carbon Dioxide Capture and Storage*, Prepared by Working Group III of the Intergovernmental Panel on Climate Change [Metz, B., Davidson, O., de Coninck, H., Loos, M., & Meyer, L. (eds.)]. Cambridge University Press, Cambridge, 1-442.
- [21] Juanes, R., MacMinn, C., & Szulczewski, M. (2010). The footprint of the CO<sub>2</sub> plume during carbon dioxide storage in saline aquifers: storage efficiency for capillary trapping at the basin scale. *Transport in Porous Media*, 82, 19-30.

- [22] Kestin, J., Khalifa, E., & Correla, R. (1981). Tables of the dynamic and kinematic viscosity of aqueous NaCl solutions in the temperature range 20-150°C and the pressure range 0.1-35 MPa. *Physical Chemistry Reference Data*, 10, 71-87.
- [23] Klass, A. & Wilson, W. (2010). Climate change, carbon sequestration, and property rights. *University of Illinois Law Review*, 2, 363-428.
- [24] Kochina, I., Mikhailov, N., & Filinov, M. (1983). Groundwater mound damping. *International Journal of Engineering Science*, 21, 413-421.
- [25] Lax, P. (1957). Hyperbolic systems of conservation laws II. *Communications on Pure and Applied Mathematics*, 10, 537-566.
- [26] LeFloch, P. (2002). Hyperbolic systems of conservation laws: the theory of classical and nonclassical shock waves. *Lectures in Mathematics*. ETH Zurich, Birkhauser, 29-30, 88-93, 257-261.
- [27] Lie, K. (2001). The front tracking method. Found at: [folk.uio.no/kalie/fronttrack/ftrack/scalar.html](http://folk.uio.no/kalie/fronttrack/ftrack/scalar.html).
- [28] MacMinn, C., Szulczewski, M., & Juanes, R. (2010). CO<sub>2</sub> migration in saline aquifers. Part 1. Capillary trapping under slope and groundwater flow. *Journal of Fluid Mechanics*, 662, 329-351.
- [29] May, L., Shearer, M., & Daniels, K. (2010). Scalar conservation laws with non constant coefficients with application to particle size segregation in granular flow. *Nonlinear Science*, 20, 689-707.
- [30] Neufeld, J., Hesse, M., Riaz, A., Hallworth, M., Tchelepi, H., & Huppert, H. (2010). Convective dissolution of carbon dioxide in saline aquifers. *Geophysical Research Letters*, 37, L22404.
- [31] Nicot, J. (2008). Evaluation of large-scale CO<sub>2</sub> storage on fresh-water sections of aquifers: an example from the Texas Gulf Coast Basin. *International Journal of Greenhouse Gas Control*, 2, 4, 582-593.

- [32] Nilsen, H., Lie, K. & Andersen, O. (2016). Robust simulation of sharp-interface models for fast estimation of CO<sub>2</sub> trapping capacity in large-scale aquifer systems. *Computational Geosciences*, 20, 1, 93-113.
- [33] Nordbotten, J., Celia, M., & Bachu, S. (2005). Injection and storage of CO<sub>2</sub> in deep saline aquifers: analytical solution for CO<sub>2</sub> plume evolution during injection. *Transport in Porous Media*, 58, 339-360.
- [34] Olivier, J., Janssens-Maenhout, G., Muntean, M., & Peters, J. (2015). *Trends in global CO<sub>2</sub> emissions: 2015 report*, PBL Netherlands Environmental Assessment Agency, European Commission Joint Research Centre, The Hague.
- [35] Ouyang, L. (2011). New correlations for predicting the density and viscosity of supercritical carbon dioxide under conditions expected in carbon capture and sequestration operations. *The Open Petroleum Journal*, 4, 13-21.
- [36] Qi, R., LaForce, T., & Blunt, M. (2009). Design of carbon dioxide storage in aquifers. *Greenhouse Gas Control*, 3, 195-205.
- [37] Shearer, M. & Dafermos, C. (2010). Finite time emergence of a shock wave for scalar conservation laws. *Journal of Hyperbolic Differential Equations*, 7, 1, 1-10.
- [38] Shearer, M. & Levy, R. (2016). *Partial differential equations: an introduction to theory and applications*, Princeton University Press, 201-204.
- [39] Shen, C. & Sun, M. (2015). Instability of Riemann solutions to a scalar conservation law with discontinuous flux, *Applied Mathematics and Physics*, 66, 499-515.
- [40] Silin, D., Patzek, T., & Benson, S. (2009). A one-dimensional model of vertical gas plume migration through a heterogeneous porous medium. *Greenhouse Gas Control*, 3, 300-310.
- [41] Statoil. (2013). *The Sleipner area*. Found at: [statoil.com/en/OurOperations/ExplorationProd/ncs/sleipner](http://statoil.com/en/OurOperations/ExplorationProd/ncs/sleipner).
- [42] Terpolilli, P. (2014). Flow in porous media: physical, mathematical and numerical aspects. *Stavanger-CFD Workshop*, 26.
- [43] United States Environmental Protection Agency. (2016). *Carbon Dioxide Capture and Sequestration Schematic*. Found at: [epa.gov/climatechange/ccs/](http://epa.gov/climatechange/ccs/).

- [44] Vella, D. & Huppert, H. (2006). Gravity currents in a porous medium at an inclined plane. *Fluid Mechanics*, 555, 353-362.
- [45] Wikipedia contributors. (2013). *Capillary pressure*. Wikipedia, The Free Encyclopedia. Found at: [en.wikipedia.org/wiki/Capillary\\_pressure](http://en.wikipedia.org/wiki/Capillary_pressure).
- [46] Wyckoff, R. & Botset, H. (1936). The flow of gas-liquid mixtures through unconsolidated sands. *Journal of Applied Physics*, 7, 325-345.
- [47] Zheng, J. (2011). *Value distribution of meromorphic functions*, Springer Science & Business Media, 277.
- [48] Zhu, C., Zhang, G., Lu, P., Meng, L., & Ji, X. (2015). Benchmark modeling of the Sleipner CO<sub>2</sub> plume: calibration to seismic data for the uppermost layer and model sensitivity analysis. *Greenhouse Gas Control*, 43, 233-246.

## APPENDICES



---

Preliminary Proofs

---

In this appendix, we develop proofs for preliminary theorems that were referenced in Chapter 5: Helly's Compactness Theorem and the Time-Dependent Helly's Theorem. We also present a proof to the precursor Arzela-Ascoli Theorem which also utilizes the process of creating a diagonal sequence with special properties.

## A.1 Helly's Compactness Theorem

**Theorem A.1.1.** *Given a sequence of functions,  $\eta^h : (a, b) \rightarrow \mathbb{R}^N$ , with bounded variation, which is defined at every point  $\xi \in (a, b)$ , and satisfies, for some constant  $C > 0$ ,*

$$\left\| \eta^h \right\|_{L^\infty((a,b);\mathbb{R}^N)} + TV(\eta^h; (a, b)) \leq C, \quad (\text{A.1.1})$$

*then there exists a subsequence,  $\eta^{n,n}$ , and there exists a function,  $\eta : (a, b) \rightarrow \mathbb{R}^N$ , with bounded variation such that*

$$\eta^{n,n}(\xi) \rightarrow \eta(\xi) \quad (\text{A.1.2})$$

*at every  $\xi \in (a, b)$ .*

*Also, we have the lower semi-continuity property whereby*

$$TV(\eta; (a, b)) \leq \liminf_{n \rightarrow \infty} TV(\eta^{n,n}; (a, b)). \quad (\text{A.1.3})$$

**Proof:**

We assume that  $(a, b) \in \mathbb{R}$  is some bounded or unbounded interval. We recall that an arbitrary function,  $\eta^h : (a, b) \rightarrow \mathbb{R}^N$ , has bounded variation if its total variation is finite:

$$\begin{aligned} TV(\eta^h; (a, b)) &= \sup \left\{ \sum_{k=1}^{q-1} \left| \eta^h(\xi_{k+1}) - \eta^h(\xi_k) \right| \text{ where } a < \xi_1 < \cdots < \xi_q < b \right\} \\ &= C_1 < C < \infty. \end{aligned}$$

We know that total variation is nondecreasing. Let us also assume that

$$\left\| \eta^h \right\|_{L^\infty((a, b); \mathbb{R}^N)} = \sup \left\{ |\eta^h(\xi)| : \xi \in (a, b) \right\} = C_2 < \infty. \quad (\text{A.1.4})$$

Hence,  $C_2 + C_1 \leq C$  by (A.1.1).

Let  $n = \frac{1}{h}$  be a given positive integer. Let the total variation of  $\eta^h$  on  $(a, \xi]$  be defined as

$$T_n(\xi) \equiv \sup \left\{ \sum_{j=1}^{q-1} \left| \eta^h(\xi_{j+1}) - \eta^h(\xi_j) \right| \text{ where } a < \xi_1 < \cdots < \xi_q = \xi \right\}.$$

Notice each  $T_n$  is nondecreasing, since total variation can only accumulate with increasing  $\xi$ . For each  $T_n$ , we also have

$$|\eta^h(\Xi) - \eta^h(\xi)| \leq T_n(p_2) - T_n(p_1) \quad (\text{A.1.5})$$

for all  $a \leq p_1 \leq \xi \leq \Xi \leq p_2 \leq b$ .

Since the functions  $\eta^h$  have bounded variation, it follows that  $T_n(\xi) \leq TV(\eta^h; (a, b)) = C_1$  for all  $\xi \in (a, b)$ . We know total variation is the sum of nonnegative quantities and is hence itself a nonnegative quantity, so  $T_n(\xi) \geq 0$  for all  $\xi \in (a, b)$ . Hence,

$$0 \leq T_n(\xi) \leq C_1 \quad \forall \xi \in (a, b). \quad (\text{A.1.6})$$

Consider the rational numbers,  $\mathbb{Q}$ , between  $a$  and  $b$ . Define this set of numbers as

$$X \equiv \{q \in \mathbb{Q} : q \in (a, b)\}.$$

Since the rational numbers have countably many elements between  $a$  and  $b$ , we can list them:  $\{q_1, q_2, q_3, \dots\} \in (a, b)$ .

We start with  $q_1$ . Consider  $\{T_n(q_1)\}_{n=1}^\infty = \{T_1(q_1), T_2(q_1), \dots, T_n(q_1), \dots\}$ . Since  $q_1 \in (a, b)$  and the total variation up to any point in  $(a, b)$  is bounded by (A.1.6), we know  $\forall n, T_n(q_1) \leq C_1 < \infty$ . So, the numerical sequence  $\{T_n(q_1)\}_{n=1}^\infty$  is bounded. By the Bolzano-Weierstrass Theorem,  $\{T_n(q_1)\}_{n=1}^\infty$  has a convergent subsequence, which we will call  $\{T_{1,n}(q_1)\}_{n=1}^\infty$ .

Next consider  $q_2$ . Consider  $\{T_{1,n}(q_2)\}_{n=1}^\infty = \{T_{1,1}(q_2), T_{1,2}(q_2), \dots, T_{1,n}(q_2), \dots\}$ . This is a numerical sequence which is bounded. Again, by the Bolzano-Weierstrass Theorem,  $\{T_{1,n}(q_2)\}_{n=1}^\infty$  has a convergent subsequence, which we will call  $\{T_{2,n}(q_2)\}_{n=1}^\infty$ .

Notice  $\{T_{2,n}\}_{n=1}^\infty$  is a subsequence of  $\{T_{1,n}\}_{n=1}^\infty$ , and  $\{T_{2,n}\}_{n=1}^\infty$  is convergent at both  $q_1$  and  $q_2$ !

We continue and obtain a countable collection of subsequences:

$$\begin{array}{cccc}
T_{1,1} & T_{2,1} & T_{3,1} & \cdots \\
T_{1,2} & T_{2,2} & T_{3,2} & \cdots \\
T_{1,3} & T_{2,3} & T_{3,3} & \cdots \\
\vdots & \vdots & \vdots & \ddots \\
|| & || & & \\
\{T_{1,n}\}_{n=1}^\infty & \{T_{2,n}\}_{n=1}^\infty & & \\
\uparrow & \uparrow & \uparrow & \\
\text{converges} & \text{converges} & \text{converges} & \\
\text{at } q_1 & \text{at } q_1, q_2 & \text{at } q_1, q_2, q_3 & 
\end{array}$$

where the elements of the  $(i+1)^{\text{th}}$  column form a subsequence of the elements of the  $i^{\text{th}}$  column.

Then, the *diagonal sequence*  $\{T_{n,n}\}_{n=1}^\infty$  converges at  $q_1, q_2, \dots, q_n, \dots$  which are all the points of  $X$ .

This diagonal sequence  $\{T_{n,n}\}_{n=1}^\infty$  is a subsequence of  $\{T_n\}_{n=1}^\infty$  which converges at all points of  $X$ . Hence, the limit of  $\{T_{n,n}\}_{n=1}^\infty$  exists at every rational number between  $a$  and  $b$ . Let

$$T(q) = \lim_{n \rightarrow \infty} T_{n,n}(q) \quad \forall q \in X. \quad (\text{A.1.7})$$

The function  $T$  is nondecreasing, and by (A.1.6), the function maps  $X$  into  $[0, C_1]$ . For each  $k \geq 1$ , we define the set of jump points to be

$$J_k \equiv \left\{ \xi \in (a, b) : \left( \lim_{\Xi \rightarrow \xi^+} T(\Xi) - \lim_{\Xi \rightarrow \xi^-} T(\Xi) \right) \geq \frac{1}{k} \right\} \quad (\text{A.1.8})$$

where  $\Xi$  ranges over  $X$ , and  $\xi$  ranges over  $\mathbb{R}$ . Let

$$J = \bigcup_{k \geq 1} J_k,$$

so  $J$  is the set of real values  $\xi \in (a, b)$  where the right and left limits of  $T$  are distinct. By the construction of  $T$ , each set  $J_k$  can contain at most  $C_1 k$  points which implies that  $J$  is countable. Since  $J$  and  $X$  are both countable,  $J \cup X$  has countably many elements, and we can list them:  $\{x_1, x_2, x_3, \dots\} \in (a, b)$ .

We start with  $x_1$ . Consider the sequence  $\{\eta^h(x_1)\}$  as  $h \rightarrow 0^+$ . Since  $x_1 \in (a, b)$ , and  $|\eta^h(\xi)| \leq C_2$  for any point  $\xi$  in  $(a, b)$  by (A.1.4), we know  $\forall h, |\eta^h(x_1)| \leq C_2 < \infty$ . So, the numerical sequence  $\{\eta^h(x_1)\}_{h \rightarrow 0^+}$  is bounded. By the Bolzano-Weierstrass Theorem,  $\{\eta^h(x_1)\}_{h \rightarrow 0^+}$  has a convergent subsequence, which we will call  $\{\eta^{1,n}(x_1)\}_{n=1}^\infty$ .

Next consider  $x_2$ . Consider  $\{\eta^{1,n}(x_2)\}_{n=1}^\infty$ . This is a numerical sequence which is bounded. Again, by the Bolzano-Weierstrass Theorem, the infinite sequence  $\{\eta^{1,n}(x_2)\}_{n=1}^\infty$  has a convergent subsequence, which we will call  $\{\eta^{2,n}(x_2)\}_{n=1}^\infty$ .

Notice that  $\{\eta^{2,n}\}_{n=1}^\infty$  is a subsequence of  $\{\eta^{1,n}\}_{n=1}^\infty$ , and  $\{\eta^{2,n}\}_{n=1}^\infty$  is convergent at both  $x_1$  and  $x_2$ !

We continue and obtain a countable collection of subsequences:

$\eta^{1,1}$	$\eta^{2,1}$	$\eta^{3,1}$	$\dots$
$\eta^{1,2}$	$\eta^{2,2}$	$\eta^{3,2}$	$\dots$
$\eta^{1,3}$	$\eta^{2,3}$	$\eta^{3,3}$	$\dots$
$\vdots$	$\vdots$	$\vdots$	$\ddots$
$\parallel$	$\parallel$		
$\{\eta^{1,n}\}_{n=1}^\infty$	$\{\eta^{2,n}\}_{n=1}^\infty$		
$\uparrow$	$\uparrow$	$\uparrow$	
converges	converges	converges	
at $x_1$	at $x_1, x_2$	at $x_1, x_2, x_3$	

where the elements of the  $(i+1)^{\text{th}}$  column form a subsequence of the elements of the  $i^{\text{th}}$  column.

Then, the *diagonal sequence*  $\{\eta^{n,n}\}_{n=1}^\infty$  converges at  $x_1, x_2, \dots, x_n, \dots$  which are all the points of  $J \cup X$ .

This diagonal sequence  $\{\eta^{n,n}\}_{n=1}^{\infty}$  is a subsequence of  $\{\eta^h\}_{h \rightarrow 0^+}$  which converges at all points of  $J \cup X$ . Since each of the functions in the sequence  $\{\eta^h\}_{h \rightarrow 0^+}$  has bounded variation, we know that the subsequence  $\{\eta^{n,n}\}_{n=1}^{\infty}$  also has bounded variation. Hence, the limit of  $\{\eta^{n,n}\}_{n=1}^{\infty}$  exists at every point in the countable set  $J \cup X$ . Let

$$\eta(\xi) = \lim_{n \rightarrow \infty} \eta^{n,n}(\xi) \quad \forall \xi \in J \cup X. \quad (\text{A.1.9})$$

Let  $\xi \notin J$  be an arbitrary real point in  $(a, b)$ . Hence,  $\xi \notin J_k$  for all  $k \geq 1$ . Then, by (A.1.8),  $\forall k \geq 1, \exists p_1, p_2 \in X$  with  $p_1 < \xi < p_2$  such that

$$T(p_2) - T(p_1) < \frac{2}{k}. \quad (\text{A.1.10})$$

It follows that

$$\begin{aligned} \limsup_{i,j \rightarrow \infty} |\eta^{i,i}(\xi) - \eta^{j,j}(\xi)| &= \limsup_{i,j \rightarrow \infty} |\eta^{i,i}(\xi) - \eta(p_1) + \eta(p_1) - \eta^{j,j}(\xi)| \\ &\leq \limsup_{i,j \rightarrow \infty} |\eta^{i,i}(\xi) - \eta(p_1)| + \limsup_{i,j \rightarrow \infty} |\eta(p_1) - \eta^{j,j}(\xi)| \\ &= \limsup_{i \rightarrow \infty} |\eta^{i,i}(\xi) - \eta(p_1)| + \limsup_{j \rightarrow \infty} |\eta^{j,j}(\xi) - \eta(p_1)| \\ &= \limsup_{n \rightarrow \infty} |\eta^{n,n}(\xi) - \eta(p_1)| + \limsup_{n \rightarrow \infty} |\eta^{n,n}(\xi) - \eta(p_1)| \\ &= 2 \limsup_{n \rightarrow \infty} |\eta^{n,n}(\xi) - \lim_{n \rightarrow \infty} \eta^{n,n}(p_1)| \quad \text{by (A.1.9) since } p_1 \in X \\ &= 2 \limsup_{n \rightarrow \infty} |\eta^{n,n}(\xi) - \limsup_{n \rightarrow \infty} \eta^{n,n}(p_1)| \quad \text{since } \exists \lim, \limsup = \lim \\ &= 2 \limsup_{n \rightarrow \infty} |\eta^{n,n}(\xi) - \eta^{n,n}(p_1)| \quad \text{where } \eta^{n,n} \text{ are functions in } \eta^n \\ &\leq 2 \limsup_{n \rightarrow \infty} [T_n(p_2) - T_n(p_1)] \quad \text{by (A.1.5) since } p_1 < \xi < p_2 \\ &= 2 \limsup_{n \rightarrow \infty} [T_{n,n}(p_2) - T_{n,n}(p_1)] \quad T_{n,n} \text{ is a subsequence of } T_n \\ &= 2 \lim_{n \rightarrow \infty} [T_{n,n}(p_2) - T_{n,n}(p_1)] \quad T_{n,n} \text{ convergent } \rightarrow \limsup = \lim \\ &= 2 [T(p_2) - T(p_1)] \quad \text{by (A.1.7) since } p_1, p_2 \in X \\ &< 2 \left[ \frac{2}{k} \right] = \frac{4}{k}. \quad \text{by (A.1.10).} \end{aligned}$$

Since  $\xi \notin J$  was an arbitrary real point in  $(a, b)$ , this result is true for all real points in  $(a, b)$  with  $\xi \notin J$ . Hence,  $\forall \xi \notin J$ ,  $\limsup_{i,j \rightarrow \infty} |\eta^{i,i}(\xi) - \eta^{j,j}(\xi)| < \frac{4}{k}$  for some given  $k \geq 1$ .

Hence, the sequence  $\{\eta^{n,n}\}_{n=1}^{\infty}$  is *uniformly Cauchy* for points not in  $J$ .

Let  $\eta(\xi) = \lim_{n \rightarrow \infty} \eta^{n,n}(\xi) \quad \forall \xi \notin J$ . Uniformly Cauchy implies  $\limsup_{n \rightarrow \infty} |\eta^{n,n}(\xi) - \eta^{n+i,n+i}(\xi)| < \frac{\varepsilon}{2}$  for some  $\varepsilon > 0$  and some natural number  $i$ . Hence,

$$\begin{aligned} \limsup_{n \rightarrow \infty} |\eta^{n,n}(\xi) - \eta(\xi)| &= \limsup_{n \rightarrow \infty} \left| \eta^{n,n}(\xi) - \lim_{i \rightarrow \infty} \eta^{n+i,n+i}(\xi) \right| \\ &= \limsup_{n \rightarrow \infty} \left| \eta^{n,n}(\xi) - \limsup_{i \rightarrow \infty} \eta^{n+i,n+i}(\xi) \right| \\ &= \limsup_{n \rightarrow \infty} |\eta^{n,n}(\xi) - \eta^{n+i,n+i}(\xi)| \\ &< \frac{\varepsilon}{2} < \varepsilon. \end{aligned}$$

Hence, the sequence  $\{\eta^{n,n}\}_{n=1}^{\infty}$  is *uniformly convergent* for points not in  $J$ !

So, the sequence  $\{\eta^{n,n}\}_{n=1}^{\infty}$  is a convergent subsequence, with bounded variation, of  $\{\eta^h\}_{h \rightarrow 0^+}$  for points not in  $J$ . Combination with (A.1.9) yields

$$\eta(\xi) = \lim_{n \rightarrow \infty} \eta^{n,n}(\xi) \implies \eta(\xi) = \lim_{h \rightarrow 0^+} \eta^{h,h}(\xi) \quad \forall \xi \in (a, b). \quad (\text{A.1.11})$$

For any given points  $a < \xi_1 < \dots < \xi_q < b$  where  $q \geq 1$ , by (A.1.11) we know

$$\begin{aligned} TV(\eta; (a, b)) &= \sup \left\{ \sum_{j=1}^{q-1} |\eta(\xi_{j+1}) - \eta(\xi_j)| \right\} \\ &= \sup \left\{ \sum_{j=1}^{q-1} \left| \lim_{n \rightarrow \infty} \eta^{n,n}(\xi_{j+1}) - \lim_{n \rightarrow \infty} \eta^{n,n}(\xi_j) \right| \right\}. \end{aligned}$$

Hence,

$$\begin{aligned}
TV(\eta; (a, b)) &= \sup \left\{ \lim_{n \rightarrow \infty} \left[ \sum_{j=1}^{q-1} \left| \eta^{n,n}(\xi_{j+1}) - \eta^{n,n}(\xi_j) \right| \right] \right\} \\
&= \limsup_{n \rightarrow \infty} \left[ \sup \left\{ \sum_{j=1}^{q-1} \left| \eta^{n,n}(\xi_{j+1}) - \eta^{n,n}(\xi_j) \right| \right\} \right] \\
&\leq \limsup_{n \rightarrow \infty} [TV(\eta^{n,n}; (a, b))] \\
&\leq \limsup_{h \rightarrow 0^+} [TV(\eta^h; (a, b))] \\
&= C_1 < C < \infty.
\end{aligned} \tag{A.1.12}$$

Therefore, the function  $\eta$  has bounded variation. Hence, we have shown that there exists a subsequence,  $\eta^{n,n}$ , and a function,  $\eta$ , with bounded variation such that  $\eta^{n,n}(\xi) \rightarrow \eta(\xi)$  at every  $\xi \in (a, b)$ , which proves (A.1.2).

Since  $\{\eta^{n,n}\}_{n=1}^{\infty}$  is convergent, it follows that  $TV(\eta^{n,n}; (a, b))$  is convergent. Hence,

$$\lim_{n \rightarrow \infty} TV(\eta^{n,n}; (a, b)) = \limsup_{n \rightarrow \infty} TV(\eta^{n,n}; (a, b)) = \liminf_{n \rightarrow \infty} TV(\eta^{n,n}; (a, b)).$$

By (A.1.12), we have

$$\begin{aligned}
TV(\eta; (a, b)) &\leq \limsup_{n \rightarrow \infty} TV(\eta^{n,n}; (a, b)) \\
&= \liminf_{n \rightarrow \infty} TV(\eta^{n,n}; (a, b)) = \liminf_{h \rightarrow 0^+} TV(\eta^h; (a, b)),
\end{aligned}$$

which proves (A.1.3) and completes the proof of the Helly's Compactness Theorem A.1.1.  $\square$

## A.2 Time-Dependent Helly's Theorem

**Theorem A.2.1.** *Given a sequence of functions,  $\eta^h : (a, b) \times \mathbb{R}^+ \rightarrow \mathbb{R}^N$  that satisfies*

$$\left\| \eta^h(\tau) \right\|_{L^\infty((a,b);\mathbb{R}^N)} + TV\left(\eta^h(\tau); (a, b)\right) \leq C \quad (\text{A.2.1})$$

*for all  $\tau \in \mathbb{R}^+$  and some constant  $C > 0$ , and*

$$\left\| \eta^h(\tau_2) - \eta^h(\tau_1) \right\|_{L^1((a,b);\mathbb{R}^N)} \leq C |\tau_2 - \tau_1| \quad (\text{A.2.2})$$

*for all  $\tau_1, \tau_2 \in \mathbb{R}^+$ , then there exists a subsequence,  $\eta^{n,n}$ , and there exists a function with bounded variation,  $\eta : (a, b) \times \mathbb{R}^+ \rightarrow \mathbb{R}^N$ , such that*

$$\eta^{n,n}(\tau) \rightarrow \eta(\tau) \quad \text{in } L^1_{loc}, \quad (\text{A.2.3})$$

$$\left\| \eta(\tau) \right\|_{L^\infty((a,b);\mathbb{R}^N)} + TV\left(\eta(\tau); (a, b)\right) \leq C, \text{ and} \quad (\text{A.2.4})$$

$$\left\| \eta(\tau_2) - \eta(\tau_1) \right\|_{L^1((a,b);\mathbb{R}^N)} \leq C |\tau_2 - \tau_1| \quad (\text{A.2.5})$$

*for all  $\tau \in \mathbb{R}^+$  and all  $\tau_1, \tau_2 \in \mathbb{R}^+$ .*

**Proof:**

Assume that  $(a, b) \in \mathbb{R}$  is some bounded or unbounded interval. Let  $\tau_R \geq 0$  be an arbitrary rational number. By (A.2.1),

$$\left\| \eta^h(\tau_R) \right\|_{L^\infty((a,b);\mathbb{R}^N)} + TV\left(\eta^h(\tau_R); (a, b)\right) \leq C$$

for some constant  $C > 0$ . Since  $\eta^h$  is a sequence of functions with bounded variation, by Helly's Compactness Theorem it follows that there exists a subsequence,  $\eta^{n,n}$ , of  $\eta^h$ , and there exists a function  $\eta$  with bounded variation such that

$$\eta^{n,n}(\xi, \tau_R) \rightarrow \eta(\xi, \tau_R)$$

for all  $\xi \in (a, b)$ . Since  $\tau_R$  was an arbitrary rational time,

$$\eta^{n,n}(\tau_R) \rightarrow \eta(\tau_R) \quad \forall \tau_R \geq 0 \quad \text{and} \quad \forall \xi \in (a, b). \quad (\text{A.2.6})$$



Since  $\eta^{n,n}$  is a subsequence of  $\eta^h$ , it follows from (A.2.6) that

$$\left\| \eta(\tau_R) \right\|_{L^\infty((a,b);\mathbb{R}^N)} + TV\left(\eta(\tau_R); (a,b)\right) \leq C$$

for the limit function  $\eta(\tau_R)$ .

Let  $\varepsilon > 0$ . Let  $\tau \in \mathbb{R}^+$  be an arbitrary real number. Hence, there exists  $\tau_R \in \mathbb{R}^+$  such that

$$|\tau - \tau_R| < \frac{\varepsilon}{4C}. \quad (\text{A.2.7})$$

Since  $\eta^{n,n}$  converges to  $\eta$  at all rational times, (A.2.6), the subsequence is Cauchy at all rational times, and it holds that there exists  $N > 0$  such that

$$\left| \eta^{p,p}(\tau_R) - \eta^{q,q}(\tau_R) \right| < \frac{\varepsilon}{2} \quad (\text{A.2.8})$$

for all  $p$  and  $q > N$ . Thus,

$$\begin{aligned} \left\| \eta^{p,p}(\tau) - \eta^{q,q}(\tau) \right\|_{L^1} &= \left\| \eta^{p,p}(\tau) - \eta^{p,p}(\tau_R) + \eta^{p,p}(\tau_R) - \eta^{q,q}(\tau_R) + \eta^{q,q}(\tau_R) - \eta^{q,q}(\tau) \right\|_{L^1} \\ &\leq \left\| \eta^{p,p}(\tau) - \eta^{p,p}(\tau_R) \right\|_{L^1} + \left\| \eta^{p,p}(\tau_R) - \eta^{q,q}(\tau_R) \right\|_{L^1} \\ &\quad + \left\| \eta^{q,q}(\tau_R) - \eta^{q,q}(\tau) \right\|_{L^1} \quad \text{by Minkowski's inequality} \\ &\leq C |\tau - \tau_R| + \left\| \eta^{p,p}(\tau_R) - \eta^{q,q}(\tau_R) \right\|_{L^1} + C |\tau_R - \tau| \quad \text{by (A.2.2)} \\ &< C \left( \frac{\varepsilon}{4C} \right) + \frac{\varepsilon}{2} + C \left( \frac{\varepsilon}{4C} \right) \quad \text{by (A.2.7) and (A.2.8)} \\ &= \varepsilon, \end{aligned}$$

and thus  $\eta^{n,n}$  is Cauchy for all  $\tau \in \mathbb{R}^+$ . Since  $L^1$  is a complete metric space,  $\eta^{n,n}$  is convergent in  $L^1$  for all  $\tau \in \mathbb{R}^+$ . Combination with (A.2.6) yields

$$\eta^{n,n}(\tau) \rightarrow \eta(\tau) \quad \text{in } L^1 \text{ and therefore in } L^1_{\text{loc}}$$

and thus we have shown (A.2.3). Since  $\eta(\tau)$  is the limit function for a subsequence of the given sequence of functions, combination with (A.2.1) and (A.2.2) yields the bounds in (A.2.4) and (A.2.5) and completes the proof of the Time-Dependent Helly's Theorem A.2.1.  $\square$

### A.3 Arzela-Ascoli Theorem

**Theorem A.3.1.** *If a sequence  $\{f_n\}_{n=1}^{\infty}$  in  $C(X)$  is bounded and equicontinuous, then it has a uniformly convergent subsequence.*

**Proof:**

Let  $n$  be a given positive integer, and let  $x \in X$ . Define  $B\left(x, \frac{1}{n}\right) = \left\{y \in X : d(x, y) < \frac{1}{n}\right\}$  as the open ball centered at  $x$  with radius  $\frac{1}{n}$  where  $d$  is the metric on  $X$ . For this given  $n$  and  $\forall x \in X$ , the open balls  $B\left(x, \frac{1}{n}\right)$  completely cover  $X$ .

Suppose  $X$  is closed. Then  $X$  is compact since it is closed and bounded. Then,  $\exists$  a finite collection of open balls for a given  $n$  which also covers  $X$ . Let  $S_n$  be the finite collection of the  $x$ -values which are the centers of this subcollection's balls. Hence,  $\forall y \in X$ ,  $d(s, y) < \frac{1}{n}$  where  $s \in S_n$ . So,  $S_n$  is a finite subset of  $X$  which is " $\frac{1}{n}$ -dense."

When  $n$  proceeds through the integers, we obtain a collection of sets  $S_n$ . Let  $S$  be the union of all sets  $S_n$ . We see that  $S$  is countable since each  $S_n$  is finite and therefore countable.  $S$  is also dense in  $X$ . Since  $S$  has countably many elements, we can list them:  $\{x_1, x_2, x_3, \dots\} \in X$ .

We start with  $x_1$ . Consider  $\{f_n(x_1)\}_{n=1}^{\infty} = \{f_1(x_1), f_2(x_1), \dots, f_n(x_1), \dots\}$ . Since  $x_1 \in X$  and the sequence  $\{f_n\}_{n=1}^{\infty}$  is bounded, we know  $\forall n, |f_n(x_1)| \leq M < \infty$  for some  $M > 0$ . So, the numerical sequence  $\{f_n(x_1)\}_{n=1}^{\infty}$  is bounded. By the Bolzano-Weierstrass Theorem,  $\{f_n(x_1)\}_{n=1}^{\infty}$  has a convergent subsequence, which we will call  $\{f_{1,n}(x_1)\}_{n=1}^{\infty}$ .

Next consider  $x_2$ . Consider  $\{f_{1,n}(x_2)\}_{n=1}^{\infty} = \{f_{1,1}(x_2), f_{1,2}(x_2), \dots, f_{1,n}(x_2), \dots\}$ . This is a numerical sequence which is bounded. Again, by the Bolzano-Weierstrass Theorem,  $\{f_{1,n}(x_2)\}_{n=1}^{\infty}$  has a convergent subsequence, which we will call  $\{f_{2,n}(x_2)\}_{n=1}^{\infty}$ .

Notice that each of functions within the sequences of functions  $\{f_{2,n}\}_{n=1}^{\infty}$  is a function in  $\{f_{1,n}\}_{n=1}^{\infty}$ , so  $\{f_{2,n}\}_{n=1}^{\infty}$  is a subsequence of  $\{f_{1,n}\}_{n=1}^{\infty}$ , and  $\{f_{2,n}\}_{n=1}^{\infty}$  is convergent at both  $x_1$  and  $x_2$ !

We continue and obtain a countable collection of subsequences:

$$\begin{array}{cccc}
f_{1,1} & f_{2,1} & f_{3,1} & \cdots \\
f_{1,2} & f_{2,2} & f_{3,2} & \cdots \\
f_{1,3} & f_{2,3} & f_{3,3} & \cdots \\
\vdots & \vdots & \vdots & \ddots \\
\parallel & \parallel & & \\
\{f_{1,n}\}_{n=1}^{\infty} & \{f_{2,n}\}_{n=1}^{\infty} & & \\
\uparrow & \uparrow & \uparrow & \\
\text{converges} & \text{converges} & \text{converges} & \\
\text{at } x_1 & \text{at } x_1, x_2 & \text{at } x_1, x_2, x_3 & 
\end{array}$$

where the elements of the  $(i+1)^{\text{th}}$  column form a subsequence of the elements of the  $i^{\text{th}}$  column.

Then, the *diagonal sequence*  $\{f_{n,n}\}_{n=1}^{\infty}$  converges at  $x_1, x_2, \dots, x_n, \dots$  which are all the points of  $S$ . This diagonal sequence  $\{f_{n,n}\}_{n=1}^{\infty}$  is a subsequence of  $\{f_n\}_{n=1}^{\infty}$  which converges at all points of  $S$ .

Let  $\varepsilon > 0$ . Since the original sequence  $\{f_n\}_{n=1}^{\infty}$  is equicontinuous, by definition, we know  $\forall \varepsilon > 0, \exists \delta(\varepsilon) > 0 \ni \forall x, y \in X$  with  $d(x, y) < \delta \implies |f_n(x) - f_n(y)| < \varepsilon$ .

Now choose  $\delta > 0 \ni$  if  $d(x, y) < \delta \ \forall x, y \in X$ , then

$$|f_{n,n}(x) - f_{n,n}(y)| < \frac{\varepsilon}{3} \quad (\text{A.3.1})$$

for all positive integers  $n$ . We know this  $\delta$  exists due to the equicontinuity of the original sequence and knowledge that each  $f_{n,n}$  is a function within the original sequence  $\{f_n\}_{n=1}^{\infty}$ .

Let  $M > 0$  be an integer  $\ni \frac{1}{\delta} < M$ . We know  $S_M \subset S$  and  $S_M$  is finite. It follows that  $S_M$  is “ $\frac{1}{M}$ -dense” in  $X$  and therefore “ $\delta$ -dense” in  $X$  since  $\frac{1}{M} < \delta$ .

Since  $\{f_{n,n}\}_{n=1}^{\infty}$  converges at each point in  $S$ , we know  $\{f_{n,n}\}_{n=1}^{\infty}$  is a convergent sequence at each point in  $S_M$ . Hence,  $\{f_{n,n}\}_{n=1}^{\infty}$  is a Cauchy sequence in  $S_M$ . Hence, there exists an integer  $N > 0 \ni \forall n, m > N$ , and  $\forall s \in S_M$ ,

$$|f_{n,n}(s) - f_{m,m}(s)| < \frac{\varepsilon}{3}. \quad (\text{A.3.2})$$

Let  $x \in X$  be arbitrary. Since  $S_M$  is “ $\delta$ -dense” in  $X$ , we know  $d(x, s) < \delta$  for some  $s \in S_M \subset X$ .

Let  $N^* = \max\{M, N\}$ . If  $n, m > N^*$ , then  $\forall s \in S_M$ ,

$$\begin{aligned}
|f_{n,n}(x) - f_{m,m}(x)| &= |f_{n,n}(x) - f_{n,n}(s) + f_{n,n}(s) - f_{m,m}(s) + f_{m,m}(s) - f_{m,m}(x)| \\
&\leq |f_{n,n}(x) - f_{n,n}(s)| + |f_{n,n}(s) - f_{m,m}(s)| + |f_{m,m}(s) - f_{m,m}(x)| \\
&\hspace{15em} \text{by triangle inequality} \\
&< |f_{n,n}(x) - f_{n,n}(s)| + \frac{\varepsilon}{3} + |f_{m,m}(x) - f_{m,m}(s)| \hspace{2em} \text{by (2)} \\
&< \frac{\varepsilon}{3} + \frac{\varepsilon}{3} + |f_{m,m}(x) - f_{m,m}(s)| \hspace{2em} \text{by (1)} \\
&\hspace{4em} \text{since } d(x, s) < \delta \text{ where } x, s \in X \text{ and } n \text{ is a positive integer} \\
&< \frac{\varepsilon}{3} + \frac{\varepsilon}{3} + \frac{\varepsilon}{3} \hspace{10em} \text{by (1)} \\
&\hspace{4em} \text{since } d(x, s) < \delta \text{ where } x, s \in X \text{ and } m \text{ is a positive integer} \\
&= \varepsilon.
\end{aligned}$$

Since  $x \in X$  was arbitrary, this result is true  $\forall x \in X$ . Hence,  $\forall x \in X$ ,  $|f_{n,n}(x) - f_{m,m}(x)| < \varepsilon$  for some given  $\varepsilon > 0$  when  $n, m > N^*$ .

Hence, the sequence  $\{f_{n,n}\}_{n=1}^{\infty}$  is *uniformly Cauchy* on  $X$ . Let  $f(x) = \lim_{n \rightarrow \infty} f_{n,n}(x) \forall x \in X$ . When  $n > N^*$ , uniformly Cauchy implies  $|f_{n,n}(x) - f_{n+k,n+k}(x)| < \frac{\varepsilon}{2}$  for some  $\varepsilon > 0$  and some natural number  $k$ . Hence,

$$\begin{aligned}
|f_{n,n}(x) - f(x)| &= \left| f_{n,n}(x) - \lim_{k \rightarrow \infty} f_{n+k,n+k}(x) \right| \\
&= \lim_{k \rightarrow \infty} |f_{n,n}(x) - f_{n+k,n+k}(x)| \\
&< \frac{\varepsilon}{2} < \varepsilon.
\end{aligned}$$

Hence the sequence  $\{f_{n,n}\}_{n=1}^{\infty}$  is *uniformly convergent*!

So, the sequence  $\{f_{n,n}\}_{n=1}^{\infty}$  is a uniformly convergent subsequence of  $\{f_n\}_{n=1}^{\infty}$ . This completes the proof of the Arzela-Ascoli Theorem A.3.1.  $\square$

## B.1 MATLAB Implementation of Analytic Results

In this appendix section, we include a MATLAB code that plots the analytic solution for the initial plume of  $\text{CO}_2$  in Section 4.2.1. The output from this code is the exact solution in the characteristic  $(\xi, \tau)$ -plane, shown in Figure 4.2.1(b). A user could modify this code for any combination of three constant states from Pair 2b in Table 4.1 that are arranged in any spatial configuration by changing the  $\eta$  values in lines 16-18 and the  $\xi$  values in lines 19-20.

Figure B.1.1: Analytic Case A Example MATLAB code.

```

1 %%%%%%%%%%%%%%%%%%%%%%%%%%%%%%%%%%%%%%%%%%%%%%%%%%%%%%%%%%%%%%%%%%%%%%%%%%
2 %%%%%%%%%%%%%%%%%%%%%%%%%%%%%%%%%%%%%%%%%%%%%%%%%%%%%%%%%%%%%%%%%%%%%%%%%% Analytic Case A Example MATLAB code %%%%%%%%%%%%%%%%%%%%%%%%%%%%%%%%%%%%%%%%%%%%%%%%%%%%%%%%%%%%%%%%%%%%%%%%%%
3 %%%%%%%%%%%%%%%%%%%%%%%%%%%%%%%%%%%%%%%%%%%%%%%%%%%%%%%%%%%%%%%%%%%%%%%%%%
4 -*-*-*-*-*-*- USER DEFINES PARAMETERS SHOWN IN ORANGE -*-*-*-*-*-*-
5 % characteristics with speeds determined by the upper flux curve are
   plotted in this blue: [0 0.7 1]
6 % characteristics with speeds determined by the upper flux curve are
   plotted in this green: [0 0.7 0]
7 hold on
8 % set solution parameters to define lower flux curve
9 eps = 0.4 ;
10 sig = 1 - eps ;
11 % let mobility be 1 here because there is an analytic solution
12 M = 1 ;
13 etastar = 1 / ( 1 + sqrt(M) ) ;
14
15 % set three constant initial states that have a jump up at position
   xil and a jump down at xi2, as in equation (4.1.1)
16 etaL = 0.2 ; -*-*-*-*-*-*- USER DEFINED -*-*-*-*-*-*-
17 etaM = 1 ; -*-*-*-*-*-*- USER DEFINED -*-*-*-*-*-*-
18 etaR = 0.3 ; -*-*-*-*-*-*- USER DEFINED -*-*-*-*-*-*-
19 xil = -0.5 ; -*-*-*-*-*-*- USER DEFINED -*-*-*-*-*-*-
20 xi2 = 0.5 ; -*-*-*-*-*-*- USER DEFINED -*-*-*-*-*-*-
21
22 % calculate upper flux values for the three eta values
23 fetaL = etaL * (1 - etaL);
24 fetaM = etaM * (1 - etaM);
25 fetaR = etaR * (1 - etaR);
26 % calculate characteristic speeds as determined by upper flux curve
27 fpetaL = -2*etaL+1;
28 fpetaM = -2*etaM+1;
29 fpetaR = -2*etaR+1;
30
31 % find speed of classical shock from etaL to etaM
32 shockslope = (fetaM - fetaL)/(etaM-etaL);
33 if shockslope < 0

```

```

34     shockslope = sig * shockslope;
35 end
36
37 % find characteristic speed of trailing edge of rarefaction
38 if etaM > etastar
39     trailslope = fpetaM;
40 else
41     trailslope = sig * fpetaM;
42 end
43
44 % find time when shock and trailing edge of rarefaction collide
45 tauT = (xi2-xi1)/(shockslope-trailslope);
46
47 % plot shock
48 plot([xi1;shockslope*tauT+xi1],[0;tauT],'b','LineWidth',3)
49 % plot trailing edge of rarefaction
50 plot([xi2;trailslope*tauT+xi2],[0;tauT],'color',[0 0.7 1])
51
52 % initiate algorithm to plot solution eta at (xi,tau) along shock
53 xi = shockslope * tauT + xi1 ;
54 tau = tauT ;
55 etaa = etaM ;
56 shockk = 1 - etaL - etaM ;
57
58 %%%%%%%%%%%%%%%%%%%%%%%%%%%%%%%%%%%%%%%%%%%%%%%%%%%%%%%%%%%%%%%%%%%%%%%%%%
59 %%%%%%%%% Plot shock position before sigma kicks in %%%%%%%%%
60 %%%%%%%%%%%%%%%%%%%%%%%%%%%%%%%%%%%%%%%%%%%%%%%%%%%%%%%%%%%%%%%%%%%%%%%%%%
61 while etaa>etastar
62     if shockk <= 0
63         % determine shock position xi from equation (4.2.2)
64         xi = (sig/(2-sig))*(1-2*etaL)*tau+xi2+(tauT^(-sig/2)*
            xi1-xi2)+tauT^((2-sig)/2)*(shockslope+(sig/(2-sig))
            *(2*etaL-1))*tau^(sig/2);
65         % use equation (4.2.1) for eta in rarefaction here
66         etaa = (1/2)*(1-(xi-xi2)/tau);
67         xijf = xi;
68         taujf = tau;

```



```

69         etaajf = etaa;
70         % backward shock results in this region
71         shockk = sig*(1-etaL-etaa);
72         plot(xi,tau, '.k')
73     else
74         xi = (1-2*etaL)*tau+xi2+((xijf-xi2)*taujf^(-1/2)-(1-2*
75             etaL)*taujf^(1/2))*tau^(.5);
76         % forward shock given by equation (4.2.3)
77         shockk = 1-etaL-etaa;
78         etaa = (1/2)*(1-(xi-xi2)/tau);
79         taustarish = tau;
80         plot(xi,tau, '.r')
81     end
82     tau=tau+0.01;
83 end
84 % calculate taustar corresponding to time when shock and vertical
85 % characteristic from rarefaction interact
86 taustarish = taujf*(((1-etaL)-etaL)/(etastar-etaL))^2;
87 % calculate analytic solution of final interaction time
88 tf=taustarish*((etaR*(2*eps-1)-eps*(1-2*etaL))/(etastar*(2*eps-1)+
89     eps*(2*etaL-1))) ...
90     ^((2*(1-eps)/(2*eps-1)));
91 % initiate forward shock resulting from interaction with
92 % characteristics determined by lower flux curve
93 tau = taustarish ;
94 %%%%%%%%%%%%%%%%%%%%%%%%%%%%%%%%%%%%%%%%%%%%%%%%%%%%%%%%%%%%%%%%%%%%%%%%%%%
95 %%%%%%%%% Plot shock position after sigma kicks in %%%%%%%%%
96 %%%%%%%%%%%%%%%%%%%%%%%%%%%%%%%%%%%%%%%%%%%%%%%%%%%%%%%%%%%%%%%%%%%%%%%%%%%
97 while tau < tf
98     % determine shock position xi from equation (4.2.5)
99     xi = (sig/(2*sig-1))*(1-2*etaL) * tau + xi2 + (tau^(1/(2*sig
100         ))) * (2*etaL-1) * (sig/(2*sig-1)) * taustarish^((2*sig
101         -1)/(2*sig)) ;
102     plot(xi,tau, '.m');
103     tau=tau+0.01;

```

```

100         endspot = (xi2+sig*(1-2*etaR)*tau)-xi;
101     end
102
103 % Find slope of leading edge of rarefaction %
104 if etaR > etastar
105     leadslope = fpetaR;
106 else
107     leadslope = sig * fpetaR;
108 end
109 % plot leading edge of rarefaction
110 plot([xi2;xi2+(tau-0.01)*leadslope],[0;tau-0.01],'color',[0 0.7 0]);
111
112 % format figure to Ralph-level of perfection and readability
113 left = '\eta_L';
114 middle = '\eta_M';
115 right = '\eta_R';
116 siglegend = '\sigma';
117 %title([left '=' num2str(etaL) ', ' middle '=' num2str(etaM) ', '
118         right '=' num2str(etaR) ', ' siglegend '=' num2str(sig)])
119 h = gca;
120 set(h,'FontSize',[15]);
121 h=xlabel('Position', \xi);
122 h=ylabel('Time', \tau);
123 set(h,'interpreter','tex');
124 axis([-1.5 6 0 22])
125
126 % find resulting shock speed from etaL to etaR
127 shockresult = (fetaR - fetaL)/(etaR-etaL);
128 if shockresult < 0
129     shockresult = sig * shockresult;
130 else
131     shockresult = shockresult;
132 end
133 % plot resulting shock
134 plot([xi2 + tf * leadslope , xi2 + tf * leadslope + 3*shockresult],
135     [tf,tf+3],'c');

```

```

135 % plot example characteristic in rarefaction where sigma=1
136 plot([xi2; xijf],[0; taujf], 'color',[0 0.7 1], 'LineWidth',1)
137 % plot example characteristic in rarefaction where sigma=1-eps
138 plot([xi2; xi2],[0; taustarish], 'color',[0 0.7 1], 'LineWidth',1)
139
140 % plot cross-hatch characteristics in constant regions of
    characteristic plane
141 % plot cross-hatch characteristics in etaM region
142 plot([0; trailslope*.568182],[0;.568182], 'color',[0 0.7 1])
143 plot([0.25; sig*trailslope*.625+0.25],[0;.625], 'color',[0 0.7 0])
144 % plot cross-hatch characteristics in etaR region
145 taucrossR = 22;
146 plot([1.5; 1.5+taucrossR*leadslope],[0; taucrossR], 'color',[0 0.7 0]);
147 plot([1.5; 1.5+taucrossR*leadslope/sig],[0; taucrossR], 'color',[0 0.7
    1]);
148 % plot cross-hatch characteristics in etaL region
149 plot([-7.1490; -7.1490+taucrossR*fpetaL],[0; taucrossR], 'color',[0 0.7
    1]);
150 plot([-7.9180; -7.9180+taucrossR*fpetaL*sig],[0; taucrossR], 'color',[0
    0.7 0]);
151 % characteristics from slower on left LEAVE the resulting shock
152 plot([3.7733; 3.7733+taucrossR*fpetaL*sig], [16.1255; 16.1255+
    taucrossR], 'color',[0 0.7 0]);
153 % characteristic that GRAZES shock at (1) in Figure 4.2.1(b) is from
    the slower family of characteristics corresponding to etaL
154 plot([-2.4180; -2.4180+taucrossR*fpetaL*sig],[0; taucrossR], 'color',[0
    0.7 0]);
155 % indicate (with a star!) the graze point where the resulting shock
    has the same speed as the slower characteristics on left
156 plot(1.2090, 10.075, 'mp')

```

## B.2 Wave-front Tracking Numerical Code

In this section, we include a MATLAB code that generates wave-front tracking solutions for any initial plume of CO<sub>2</sub> with compact support. There are two user-defined values that can be adjusted to refine the solution. In line 24, the user sets the number of points within the initial condition at which the plume heights will be determined and used to generate an initial piecewise constant approximation. In line 66, the user sets the maximum size of expansion shocks, as in equation (5.3.11). If the desired results need appropriately small (magnitude  $h$  or smaller) jumps *up and down* between constant states, lines 75-80 can be modified, by including an absolute value, to restrict the size of allowed *compression and expansion shocks*, as was done to generate the wave-front tracking solutions in Chapter 7. This code produces three figures: (1) an initial plume approximated with piecewise constant functions in the  $(\xi, \eta)$ -plane, and the wave-front tracking solution in the  $(\xi, \tau)$ -plane (2) and  $(\xi, \eta)$ -plane (3).

Figure B.2.1: Wave-front tracking MATLAB code.

```

1 %%%%%%%%%%%%%%%%%%%%%%%%%%%%%%%%%%%%%%%%%%%%%%%%%%%%%%%%%%%%%%%%%%%%%%%%%%
2 %%%%%%%%%%%%%%%%%%%%%%%%%%%%%%%%%%%%%%%%%%%%%%%%%%%%%%%%%%%%%%%%%%%%%%%%%% Wave-front tracking MATLAB code %%%%%%%%%%%%%%%%%%%%%%%%%%%%%%%%%%%%%%%%%%%%%%%%%%%%%%%%%%%%%%%%%%%%%%%%%%
3 %%%%%%%%%%%%%%%%%%%%%%%%%%%%%%%%%%%%%%%%%%%%%%%%%%%%%%%%%%%%%%%%%%%%%%%%%%
4 -*-*-*-*-*-*- USER DEFINES PARAMETERS SHOWN IN ORANGE -*-*-*-*-*-*-
5 clear
6 % initiate figure 1 – initial plume configuration and piecewise
   constant approximation of initial condition
7 figure('units','normalized','position',[0 0 .4 1])
8 subplot(12,1,[1 3])
9 hold on
10
11 % compact support (all brine) outside of initial CO2 plume
12 etaL = 0 ;
13 etaR = 0 ;
14
15 %%%%%%%%%%%%%%%%%%%%%%%%%%%%%%%%%%%%%%%%%%%%%%%%%%%%%%%%%%%%%%%%%%%%%%%%%%
16 %%%%%%%%%%%%%%%%%%%%%%%%%%%%%%%%%%%%%%%%%%%%%%%%%%%%%%%%%%%%%%%%%%%%%%%%%% Generate random plume shape %%%%%%%%%%%%%%%%%%%%%%%%%%%%%%%%%%%%%%%%%%%%%%%%%%%%%%%%%%%%%%%%%%%%%%%%%%
17 %%%%%%%%%%%%%%%%%%%%%%%%%%%%%%%%%%%%%%%%%%%%%%%%%%%%%%%%%%%%%%%%%%%%%%%%%%
18
19 % non-dimensional plume height is between 0 (no CO2 – all brine)
   and 1 (all CO2 – no brine)
20 minplume = 0 ;
21 maxplume = 1 ;
22
23 % set the number of middle plume height values within the initial
   plume: i.e. if the number of middle values is 2, then the random
   plume shape will be 0 – first middle plume height value – second
   middle value – 0.
24 nummids = 7 ; -*-*-*-*-*-*-*-*-*- USER DEFINED -*-*-*-*-*-*-*-*-*-
25 % finds the number of constant states approximating initial
   condition: each constant state occupies one subinterval of the
   plume's initial lateral extent
26 numsubints = nummids + 1 ;
27 % finds the number of endpoints of all subintervals and determines
   the initial number of jumps up and down which will approximate
   initial condition

```

```

28 numendpts = nummids + 2 ;
29 % finds the number of constant states in piecewise approximation of
    the initial condition , including eta = 0 to the left and to the
    right of plume
30 numconsts = nummids + 3 ;
31
32 % sets grid for xi position
33 xx(:,1) = linspace(-2,2,numendpts) ;
34
35 % generates random initial plume geometry each time user runs code
36 r = minplume + (maxplume-minplume).*rand(nummids,1) ;
37 % example of r vector that generated figures shown in defense.
    values correspond to last to digits of years PhDs were earned by
    committee members (and me!): EB AC MS MH RS BB EB
38 % r = [ 0.17 ; 0.99 ; 0.76 ; 0.96 ; 0.90 ; 0.94 ; 0.17 ] ;
39 rzeros = [ etaL ; r ; etaR ] ;
40
41 % plot initial plume condition in xi-eta plane in figure 1
42 h = area(xx(:,1),rzeros) ;
43 h.FaceColor = [0 0.8 1];
44 plot(xx(:,1),rzeros,'color',[0 0.8 1])
45
46 %%%%%%%%%%%%%%%%%%%%%%%%%%%%%%%%%%%%%%%%%%%%%%%%%%%%%%%%%%%%%%%%%%%%%%%%%%
47 %%%%%%%%%% Determine piecewise constant approximation %%%%%%%%%%
48 %%%%%%%%%% of initial condition %%%%%%%%%%
49 %%%%%%%%%%%%%%%%%%%%%%%%%%%%%%%%%%%%%%%%%%%%%%%%%%%%%%%%%%%%%%%%%%%%%%%%%%
50 i = 1 ;
51 for i = 1:numconsts
52     if i == 1
53         etaxx(i,1) = etaL ;
54     elseif i == numconsts
55         etaxx(i,1) = etaR ;
56     % take the average of the plume heights at the endpoints of the
        subinterval to determine the constant approximation of the
        initial condition in that subinterval
57     else
58         etaxx(i,1) = ( rzeros(i) + rzeros(i-1) ) / 2 ;

```

```

59     end
60     i = i + 1 ;
61 end
62
63 %%%%%%%%%%%%%%%%%%%%%%%%%%%%%%%%%%%%%%%%%%%%%%%%%%%%%%%%%%%%%%%%%%%%%%%%%%
64 %%%%%%%%%%%%%%%%%%%%%%%%%%%%%%%%%%%%%%%%%%%%%%%%%%%%%%%%%%%%%%%%%%%%%%%%%% Set maximum size of expansion shocks , h %%%%%%%%%%%%%%%%%%%%%%%%%%%%%%%%%%%%%%%%%%%%%%%%%%%%%%%%%%%%%%%%%%%%%%%%%%
65 %%%%%%%%%%%%%%%%%%%%%%%%%%%%%%%%%%%%%%%%%%%%%%%%%%%%%%%%%%%%%%%%%%%%%%%%%%
66 hMAXjumpSIZE = 0.5 ; ----- USER DEFINED -----
67
68 numexp = 0;
69 position = 2;
70 % define first entry in piecewise constant initial condition as 0
71 % since we assume plume has compact support
72 etasmallrars(1,1) = etaL;
73 xxsmallrars(1,1) = xx(1,1);
74 for i = 1:numsubints
75     % find jumps DOWN exceeding threshold size h, equation (6.3.11)
76     if ((rzeros(i)-rzeros(i+1))/2) > hMAXjumpSIZE
77         % size of jump down determines number of expansion shocks
78         if rem((rzeros(i)-rzeros(i+1)) , hMAXjumpSIZE) == 0
79             numexp = fix((rzeros(i)-rzeros(i+1)) / hMAXjumpSIZE);
80         else
81             numexp = fix((rzeros(i)-rzeros(i+1)) / hMAXjumpSIZE)+1;
82         end
83     % determine values of constant states between expansion
84     % shocks and initial locations of new expansion shocks
85     for j = 1:numexp
86         etasmallrars(position+j-1,1) = rzeros(i) - ( rzeros(i)
87             - rzeros(i+1) ) / (numexp*2) * (2*j-1) ;
88         xxsmallrars(position+j-1,1) = xx(i+1,1) - ( xx(i+1,1)
89             - xx(i,1) ) / numexp * (numexp - j) ;
90         % plot piecewise constant approx of initial plume
91         plot( [ xxsmallrars(position+j-2,1) ; xxsmallrars(
92             position+j-1,1) ] , [ etasmallrars(position+j-1,1)
93             ; etasmallrars(position+j-1,1) ], 'color',[.6 0 1])
94         plot( [ xxsmallrars(position+j-2,1) ; xxsmallrars(
95             position+j-1,1) ] , [ etasmallrars(position+j-1,1)
96             ; etasmallrars(position+j-1,1) ], 'color',[.6 0 1])

```



```

89         ; etasmallrares(position+j-1,1) ], 'color',[.6 0 1])
90     j = j + 1 ;
91     end
92     position = position + numexp ;
93     % plot expansion shocks that are initially sufficiently small
94     % enough and classical shocks of any size
95     else
96         etasmallrares(position,1) = etaxx(i+1,1) ;
97         xxsmallrares(position,1) = xx(i+1,1) ;
98         % plot constant states (horizontal lines)
99         plot( [ xxsmallrares(position-1,1) ; xxsmallrares(position
100             ,1) ] , [ etasmallrares(position,1) ; etasmallrares(
101                 position,1) ], 'color',[.6 0 1])
102         % vertical lines connecting constant states
103         plot( [ xxsmallrares(position-1,1) ; xxsmallrares(position
104             -1,1) ] , [ etasmallrares(position-1,1) ; etasmallrares(
105                 position,1) ], 'color',[.6 0 1])
106         position = position + 1;
107     end
108     i = i + 1 ;
109 end
110 % define final entry in piecewise constant initial condition as 0
111 % since we assume plume has compact support
112 etasmallrares(position,1) = etaR ;
113 % plot final expansion shock down to eta = 0
114 plot( [ xxsmallrares(position-1,1) ; xxsmallrares(position-1,1) ] ,
115     [ etasmallrares(position-1,1) ; etasmallrares(position,1) ])
116 % format figure to Ralph-level of perfection and readability
117 h = gca;
118 set(h,'FontSize',[18]);
119 h=xlabel('Position', \xi');
120 h=ylabel('Plume Height', \eta');
121 set(h,'interpreter','tex');
122 title({'Initial Random Plume with Piecewise Approximation' ; '&
123     Small Expansion Shocks'})

```

```

117 %%%%%%%%%%%%%%%%%%%%%%%%%%%%%%%%%%%%%%%%%%%%%%%%%%%%%%%%%%%%%%%%%%%%%%%%%%
118 %%%%%%%%%%%%%%%%%%%%%%%%%%%%%%%%%%%%%%%%%%%%%%%%%%%%%%%%%%%%%%%%%%%%%%%%%% Solve initial Riemann problems %%%%%%%%%%%%%%%%%%%%%%%%%%%%%%%%%%%%%%%%%%%%%%%%%%%%%%%%%%%%%%%%%%%%%%%%%%
119 %%%%%%%%%%%%%%%%%%%%%%%%%%%%%%%%%%%%%%%%%%%%%%%%%%%%%%%%%%%%%%%%%%%%%%%%%%
120
121 % initiate figure 2 – solution in characteristic xi–tau plane!
122 subplot(12,1,[6 12])
123 hold on
124 % set solution parameters to define lower flux curve
125 eps = 0.4 ;
126 sig = 1 – eps ;
127 % let mobility be 1 here because there is an analytic solution
128 M = 1 ;
129 etastar = 1 / ( 1 + sqrt(M) ) ;
130
131 tausmallrares(1,1) = 0 ;
132 j = 1 ;
133 % determine shock speeds for all shocks where another file , f.m, has
    function y = f(eta) defined as y = eta * ( 1 – eta ) ;
134 for j = 1:(position–1)
135     shockslope(j,1) = ( f(etasmallrares(j+1,1)) – f(etasmallrares(j
        ,1)) ) / ( etasmallrares(j+1,1)– etasmallrares(j,1)) ;
136     % classical shocks (jumps up in initial condition) have backward
        shock speeds reduced due to trapping
137     if etasmallrares(j+1,1)>etasmallrares(j,1)
138         if shockslope(j,1) < 0
139             shockslope(j,1) = sig * shockslope(j,1);
140         end
141     % expansion shocks (jumps down in initial condition) have
        forward shock speeds reduced due to trapping
142     else
143         if shockslope(j,1) > 0
144             shockslope(j,1) = sig * shockslope(j,1);
145         end
146     end
147     j = j + 1 ;
148 end
149

```



```

180         xxsmallrares(i2,loop-1) ;
181     elseif i2 > intloc(loop-1,1)
182         xxsmallrares(i2-1,loop) = shockslope(i2,loop-1) * (
183             tausmallrares(loop,1) - tausmallrares(loop-1,1)) +
184             xxsmallrares(i2,loop-1) ;
185     end
186     i2 = i2 + 1 ;
187 end
188 % the collision of shocks indicates the elimination of a
189 % constant state from the solution: i.e. if interaction
190 % location = 1, then shock 1 (between states 1 and 2) collides
191 % with shock 2 (between states 2 and 3) - hence, state 2 is
192 % eliminated, and we are left with a shock, call it shock 1,
193 % between previous states 1 and 3, call them states 1 and 2.
194 j3 = 1 ;
195 for j3 = 1:((position-1) + 2 - loop)
196     if j3 <= intloc(loop-1,1)
197         etasmallrares(j3,loop) = etasmallrares(j3,loop-1) ;
198     elseif j3 > intloc(loop-1,1)
199         etasmallrares(j3,loop) = etasmallrares(j3+1,loop-1) ;
200     end
201     j3 = j3 + 1 ;
202 end
203 % determine all shock speeds after previous interaction time
204 j4 = 1 ;
205 for j4 = 1:(position - loop)
206     % if shock is not involved in interaction, shock speed
207     % remains as it was before this interaction time
208     if j4 < intloc(loop-1,1)
209         shockslope(j4,loop) = shockslope(j4,loop-1) ;
210     % if shock collides at this interaction time, determine
211     % outgoing shock speed using flux curves and solution
212     % values of new adjacent constant states
213     elseif j4 == intloc(loop-1,1)
214         shockslope(j4,loop) = ( f(etasmallrares(intloc(loop
215             -1,1)+1,loop)) - f(etasmallrares(intloc(loop-1,1),

```

```

loop)) ) / ( etasmallrares(intloc(loop-1,1)+1,loop)
- etasmallrares(intloc(loop-1,1),loop)) ;
205 % classical shocks (jumps up in initial condition) have
backward shock speeds reduced due to trapping
206 if etasmallrares(intloc(loop-1,1)+1,loop)>etasmallrares
(intloc(loop-1,1),loop)
207 if shockslope(j4,loop) < 0
208 shockslope(j4,loop) = sig * shockslope(j4,
loop);
209 end
210 % expansion shocks (jumps down in initial condition)
have forward shock speeds reduced due to trapping
211 else
212 if shockslope(j4,loop) > 0
213 shockslope(j4,loop) = sig * shockslope(j4,
loop);
214 end
215 end
216 % if shock is not involved in interaction, shock speed
remains as it was before this interaction time
217 elseif j4 > intloc(loop-1,1)
218 shockslope(j4,loop) = shockslope(j4+1,loop-1) ;
219 end
220 j4 = j4 + 1 ;
221 end
222
223 % calculate all times when adjacent shocks would interact
224 k2 = 1 ;
225 for k2 = 1:((position-1)-loop)
226 tauint(k2,loop) = tausmallrares(loop,1) + (xxsmallrares(k2
+1,loop) - xxsmallrares(k2,loop)) / ( shockslope(k2,loop)
- shockslope(k2+1,loop) ) ;
227 k2 = k2 + 1 ;
228 end
229 tauintfind = tauint(:,loop) ;
230
231 % find next interaction time when two adjacent shocks collide

```

```

232     tausmallrares(loop+1,1) = min(tauintfind(tauintfind>
        tausmallrares(loop,1))) ;
233
234     % determine which two shocks collided at this interaction time
235     intloc(loop,1) = ( find( tauint(:,loop) == tausmallrares(loop
        +1,1) ) );
236
237     % plot all shocks after this most recent interaction time: this
        will include all shocks that did not interact (with speeds
        equal to speeds before interaction time) and shock resulting
        from the interaction (with newly calculated shock speed)
238     j5 = 1 ;
239     for j5 = 1:(position-loop)
240         plot( [ xxsmallrares(j5,loop) ; xxsmallrares(j5,loop) +
            shockslope(j5,loop) * ( tausmallrares(loop+1,1) -
            tausmallrares(loop,1)) ] , [ tausmallrares(loop,1) ;
            tausmallrares(loop+1,1) ] )
241         j5 = j5 + 1 ;
242     end
243
244     % now loop to repeat and crush it all again!
245     loop = loop + 1 ;
246 end
247
248 % determine final lateral extent of residual surface position
249 finalxi = xxsmallrares(j5-1,loop-1) + shockslope(j5-1,loop-1) *
        ( tausmallrares(loop,1) - tausmallrares(loop-1,1));
250
251 % format figure to Ralph-level of perfection and readability
252 h = gca;
253 set(h,'FontSize',[18]);
254 h=xlabel('Position', '\xi');
255 h=ylabel('Time', '\tau');
256 set(h,'interpreter','tex');
257 title({' ',' ','Characteristic Plane with'; 'Wave-front Tracking
        Solution'})
258

```

```

259 %%%%%%%%%%%%%%%%%%%%%%%%%%%%%%%%%%%%%%%%%%%%%%%%%%%%%%%%%%%%%%%%%%%%%%%%%%
260 %%%%%%%%%% Visualize plume migration in xi-eta plane %%%%%%%%%%
261 %%%%%%%%%%%%%%%%%%%%%%%%%%%%%%%%%%%%%%%%%%%%%%%%%%%%%%%%%%%%%%%%%%%%%%%%%%
262
263 % initiate figure 3 – solution in xi-eta plane!
264 figure('units','normalized','position',[.4 0 .4 1])
265 hold on
266 % determine the finite number of interaction times
267 vidsimpending = numel(tausmallrares) ;
268
269 % to visualize the elimination of all initial constant states, we
    produce a snapshot of the solution at every interaction time
270 realplot = 1;
271 for realplot = 1:vidsimpending
272     j6 = 1;
273     set(gca,'FontSize',[18]);
274     set(gca,'YDir','Reverse')
275     set(gca,'XAxisLocation','top')
276     subplot(vidsimpending,1,realplot)
277     axis([-3 ceil(finalxi) 0 1 ])
278     set(gca,'ytick',[0 0.5 1]);
279     hold on
280     % plot solution (piecewise constant plume shape at
        calculated location in aquifer) at each interaction time
281     for j6 = 1:(vidsimpending-realplot)
282         h = area([xxsmallrares(j6,realplot);xxsmallrares(j6+1,
            realplot)],[etasmallrares(j6+1,realplot);
            etasmallrares(j6+1,realplot)]);
283         plot([xxsmallrares(j6,realplot);xxsmallrares(j6+1,
            realplot)],[etasmallrares(j6+1,realplot);
            etasmallrares(j6+1,realplot)],'color',[0 0.8 1])
284         j6 = j6 + 1 ;
285     end
286     % label each solution with the corresponding interaction time
287     str = ['\tau = ' num2str(sprintf('%2f',tausmallrares(realplot
        ,1)))] ;
288     text((floor(finalxi)-2),0.5,str,'FontSize',[18]) ;

```

```

289 %%BOO%BOO%////////////////////////////////////BOO%BOO%
290 %% Visualize residual surface as ghost images of previous %
291 %%% locations of plume now filled with bubbles of CO2 %%%
292 %%BOO%BOO%////////////////////////////////////BOO%BOO%
293
294 % since we have determined the plume location at each
    interaction time, at this step, we include the ghost plume
    solution (residual surface) in graphs at every subsequent
    interaction time
295 j8 = realplot;
296 for j8 = realplot:(vidsimpending-1)
297     xxcol = size(xxsmallreres, 2);
298     if (realplot+1)<=xxcol
299         secondxx = xxsmallreres(intloc(realplot,1),(realplot+1));
300     else secondxx = finalxi ;
301     end
302     set(gca,'FontSize',[18]);
303     set(gca,'YDir','Reverse')
304     set(gca,'XAxisLocation','top')
305     axis([-3 ceil(finalxi) 0 1 ])
306     set(gca,'ytick',[0 0.5 1]);
307     subplot(vidsimpending,1,(j8+1))
308     hold on
309     % ghosts/bubbles are light blue in plots of solution plane
310     plot([xxsmallreres(intloc(realplot,1),realplot);secondxx],[
        etasmallreres((intloc(realplot,1)+1),realplot);
        etasmallreres((intloc(realplot,1)+1),realplot)], 'color',
        [0.8 0.9 1])
311     h = area([xxsmallreres(intloc(realplot,1),realplot);secondxx
        ],[etasmallreres((intloc(realplot,1)+1),realplot);
        etasmallreres((intloc(realplot,1)+1),realplot)]);
312     j8=j8+1;
313 end
314 % subsequent solutions do not capture the plume height before
    the state is eliminated, so that ghost/residual surface
    location is determined here
315 j7 = realplot + 1;

```



```

316     for j7 = (realplot+1):vidsimpending
317         set(gca,'FontSize',[18]);
318         set(gca,'YDir','Reverse')
319         set(gca,'XAxisLocation','top')
320         axis([-3 ceil(finalxi) 0 1 ])
321         set(gca,'ytick',[0 0.5 1]);
322         subplot(vidsimpending,1,j7)
323         hold on
324         for j6 = 1:(vidsimpending-realplot)
325             h = area([xxsmallreres(j6,realplot);xxsmallreres(j6+1,
326                 realplot)],[etasmallreres(j6+1,realplot);
327                 etasmallreres(j6+1,realplot)]);
328             h.FaceColor = [0.8 0.9 1];
329             h.EdgeColor = [0.8 0.9 1];
330             plot([xxsmallreres(j6,realplot);xxsmallreres(j6+1,
331                 realplot)],[etasmallreres(j6+1,realplot);
332                 etasmallreres(j6+1,realplot)], 'color',[0.8 0.9 1])
333             j6 = j6 + 1 ;
334         end
335         j7 = j7+1;
336     end
337     % label only the first subplot axes in figure 3
338     xlabel(subplot(vidsimpending,1,1),'Position, \xi');
339     ylabel(subplot(vidsimpending,1,1),'Plume Height, \eta');
340     j9 = 2 ;
341     for j9 = 2:vidsimpending
342         set(subplot(vidsimpending,1,j9),'XTickLabel','');
343         j9 = j9 + 1 ;
344     end
345     % now crush it all again to create the next solution plot!
346     realplot = realplot + 1 ;
347 end

```